Quantum light-matter interaction of two-dimensional optical transitions coupled to dielectric microresonators

David Rosser

A dissertation

submitted in partial fulfillment of the

requirements for the degree of

Doctor of Philosophy

University of Washington

2021

Reading Committee:

Arka Majumdar, Chair

Silas Beane

Xiaodong Xu

David Masiello

Matthew Yankowitz

Program Authorized to Offer Degree:

Department of Physics

University of Washington

Abstract

Quantum light-matter interaction of two-dimensional optical transitions coupled to dielectric microresonators

David Rosser

Chair of the Supervisory Committee:
Associate Professor Arka Majumdar
Department of Physics

Photonic integrated circuits have the potential to be a disruptive technology comparable to the success of electronic integrated circuits. The absence of a compact, low-power all-optical nonlinearity limits the capability for information processing and communication applications. Dielectric microresonators and the heterogeneous integration of optical transitions such as color centers, quantum dots, and quantum wells have distinct advantages for integrated nonlinear optics. This thesis explores the light-matter interaction of two-dimensional materials supporting an excitonic optical transition coupled to dielectric microresonators. A compact expression for calculating the light-matter interaction is presented. The theoretical estimate of the light-matter interaction and input-output characteristics of the exciton-resonator system agrees with experimental observations. Exciton-phonon interactions are incorporated into the Hamiltonian model to describe the asymmetric cavity-coupled photoluminescence observed in experiments.

TABLE OF CONTENTS

PUBLICATION LIST

- A. Ryou, D. Rosser, A. Saxena, T. Fryett, and A. Majumdar, "Strong photon anti-bunching in weakly nonlinear two-dimensional exciton-polaritons", Physical Review B **97**, 235307(2018).

- D. Rosser, T. Fryett, A. Saxena, A. Ryou, A. Majumdar, and A. Majumdar, "High-precision local transfer of van der Waals materials on nanophotonic structures", Optical Materials Express **10**, 645–652 (2020).

- D. Rosser, T. Fryett, A. Ryou, A. Saxena, and A. Majumdar, "Exciton–phonon interactions in nanocavity-integrated monolayer transition metal dichalcogenides", npj 2D Materials and Applications **4**, 1–6 (2020).

- D. Rosser, D. Gerace, Y. Chen, Y. Liu, J. Whitehead, A. Ryou, L. C. Andreani, and A. Majumdar, "Dispersive coupling between MoSe2 and a zero-dimensional integrated-nanocavity", arXiv:2010.05458 (2020). Submitted to Optical Materials Express.

- D. Rosser, D. Gerace, L. C. Andreani, and A. Majumdar, "Optimal condition to probe strongcoupling of two-dimensional excitons and zero-dimensional cavity modes", arXiv:2107.00078 (2021). Submitted to Physical Review B.

LIST OF FIGURES

ACKNOWLEDGMENTS

DEDICATION

to Tanya

Chapter 1

INTRODUCTION

Atomically thin van der Waals (vdW) materials have generated strong interest in recent years for their possible electronic and optoelectronic applications [1–3]. The appeal of vdW materials for use as an active or passive material in photonic integrated circuits (PICs) hinges on their layered nature, which allows them to be integrated without concern for lattice-matching to the underlying substrate material [4]. The integration of vdW materials can thus be made independent of the PIC fabrication. The devices can be manufactured separately using existing high-throughput nanofabrication, including CMOS processes, and then the vdW material can be transferred on this pre-fabricated photonic platform to add new functionalities. The variety of vdW materials available with different optoelectronic properties provides for broad opportunities in the fabrication of light sources [5, 6], modulators [7], detectors [8], and nonlinear optical devices [4].

1.1 *Integrated nonlinear optics*

At the ultimate extreme, realizing single-photon nonlinear optics in a scalable platform could revolutionize both classical and quantum information science and engineering [9–12]. However, there exist fundamental reasons why low-power nonlinear optics in a small form factor is difficult to achieve. Consider the Mach-Zehnder interferometer (MZI, Fig. 1.1a) which consists of two input ($\hat{a}_i$) and output ($\hat{b}_i$) modes, two $50:50$ beamsplitters BS_1 and BS_2, and a phase shift $\phi_i = \beta_i L_i$ in each arm where L_i is the physical length of the optical path and $\beta_i = \frac{2\pi n_i}{\lambda}$ is the propagation constant with index of refraction n_i at the input wavelength λ [13, 14]. The mode transformations are

$$\begin{bmatrix} \hat{b}_1 \\ \hat{b}_2 \end{bmatrix} = \frac{1}{2} \underbrace{\begin{bmatrix} 1 & 1 \\ -1 & 1 \end{bmatrix}}_{BS_2} \underbrace{\begin{bmatrix} e^{i\phi_1} & 0 \\ 0 & e^{i\phi_2} \end{bmatrix}}_{\phi_L} \underbrace{\begin{bmatrix} 1 & -1 \\ 1 & 1 \end{bmatrix}}_{BS_1} \begin{bmatrix} \hat{a}_1 \\ \hat{a}_2 \end{bmatrix} \tag{1.1}$$

$$= \frac{e^{i(\phi_L+\phi_2)/2}}{2} \begin{bmatrix} \cos\phi_L/2 & i\sin\phi_L/2 \\ i\sin\phi_L/2 & \cos\phi_L/2 \end{bmatrix} \begin{bmatrix} \hat{a}_1 \\ \hat{a}_2 \end{bmatrix} \tag{1.2}$$

The relative phase shift for the linear MZI is $\phi = \phi_L$ with $\phi_L = \phi_1 - \phi_2 = \beta_1 L_1 - \beta_2 L_2$.

The optical intensity is proportional to the number operators of the modes (i.e., $I_{in} \propto \hat{a}_1^\dagger \hat{a}_1$, $I_{out} \propto \hat{b}_1^\dagger \hat{b}_1$). In the absence of input into mode $\hat{a}_2$, the output intensity of mode $\hat{b}_1$ is then

$$I_{out} = \frac{I_{in}}{2} \left(1 + \cos\phi\right) \tag{1.3}$$

By imparting a relative phase shift of $\phi = \pi$ the Mach-Zehnder interferometer output can be swept from $I_{out} = I_{in}$ to $I_{out} = 0$. In other words, the MZI acts as an optical switch. This is the premise behind optical modulators that take advantage of the electro-optic, thermo-optic, or plasma dispersion effects to manipulate the index of refraction n_i of the interferometer arms.

Now consider the nonlinear MZI with cross-phase modulation (XPM, Fig. 1.1b) due to an intensity-dependent refractive index $n = n_0 + \bar{n}_2 I$ [15, 16]. n_0 is the normal, weak-field refractive index and $\bar{n}_2$ is the second-order refractive index (optical Kerr effect). The output intensity of Eq. (1.3) now includes a nonlinear relative phase shift $\phi = \phi_L + \phi_{NL}$ with

$$\phi_{NL} = \frac{\gamma I_{in}}{2} \left(L_1 - L_2\right). \tag{1.4}$$

The nonlinear parameter is $\gamma = \frac{2\pi\bar{n}_2}{\lambda A_{eff}}$. Although the effective mode area (A_{eff}) of integrated waveguides is small, $L_1 - L_2$ must also be small for a compact footprint, and waveguiding materials are typically chosen for their foundry compatibility and low absorptive loss; not their optical nonlinearity ($\bar{n}_2$). This leads to the high power requirements needed to observe integrated nonlinear optical phenomena.
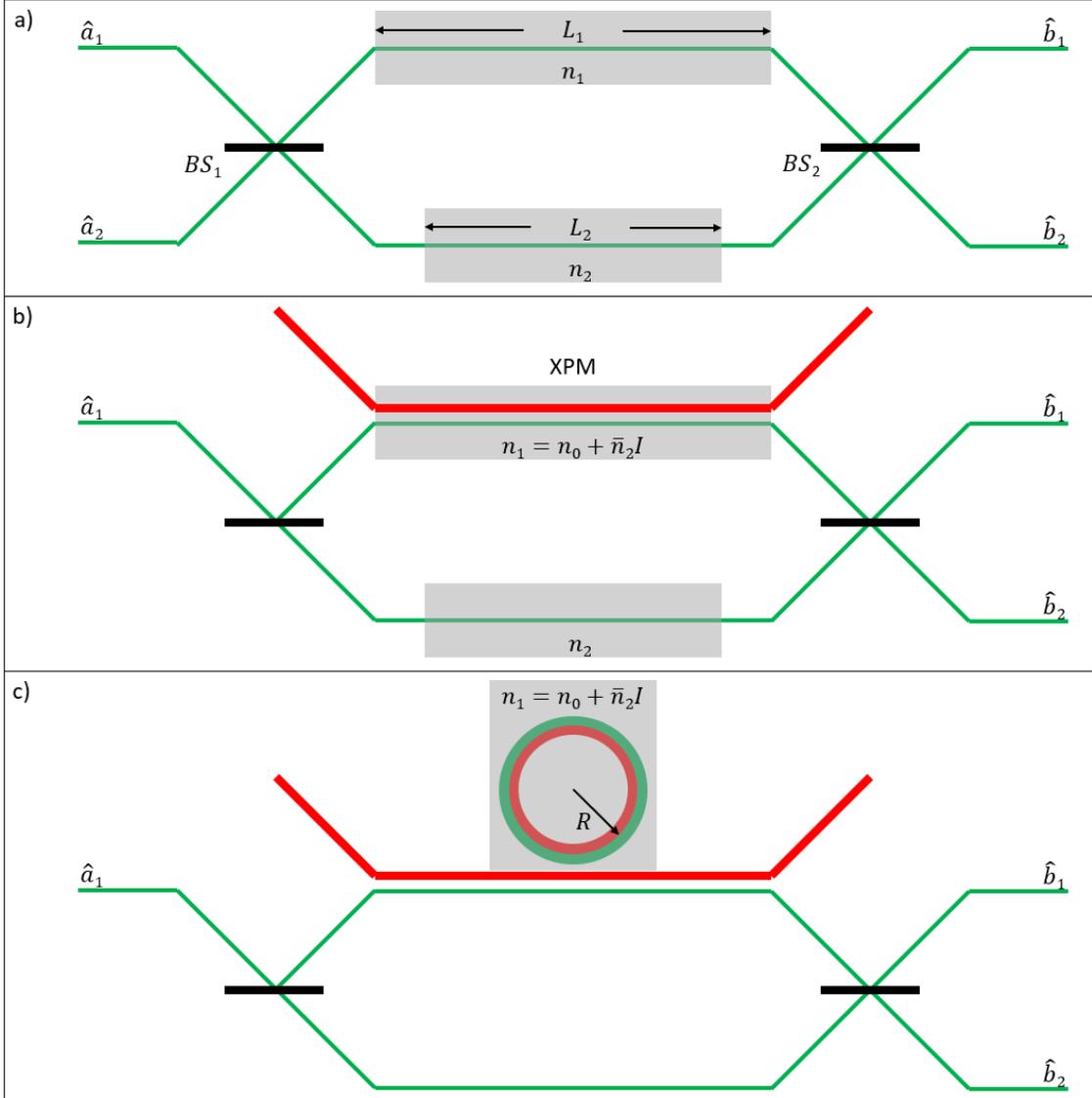
Figure 1.1: **Mach-Zehnder interferometer.** a) Mach-Zehnder interferometer (MZI) with two input and output modes, two $50:50$ beamsplitters BS_1 and BS_2, and a phase shift $\phi_i = \beta_i L_i$ in each arm. b) Nonlinear MZI with cross-phase modulation (XPM) due to an intensity-dependent refractive index $n = n_0 + \bar{n}_2 I$. c) Resonator-enhanced MZI with a nonlinear ring resonator inserted into one of the arms of a MZI enhances the nonlinear phase shift near the optical resonance.

Introduction of a nonlinear ring resonator into one of the arms of a nonlinear MZI (Fig. 1.1c) can enhance the nonlinear phase shift near the optical resonance. The effective interaction length (L_{eff}) of the interferometer arm increases due to re-circulation of the input light. And the resonator electric field intensity (I_C) increases due to accumulated temporal confinement of the input light. This results in an effective nonlinear phase shift

$$\phi_{NL} = \frac{2\overline{n}_2 I_{in}}{\pi^3 n_0^2} \underbrace{(\lambda Q)}_{L_{eff}} \underbrace{\left(\frac{Q}{V_m}\right)}_{I_C}. \qquad (1.5)$$

The quality factor $Q = \frac{\omega_0}{\Gamma}$ is a fundamental figure of merit for all resonators that quantifies the energy stored in the resonator (ω_0) relative to the power dissipated per cycle (Γ). The mode volume ($V_m = A_{eff} R$) quantifies the spatial confinement of the light in the resonator. The point of this digression was to provide a short, practical motivation for microresonators with a large Q/V_m in integrated nonlinear optics.

1.2 Microresonator QED

This thesis explores the light-matter interaction of monolayer, semiconducting transition metal dichalcogenides (TMDs) that support an excitonic optical transition evanescently coupled to a dielectric microresonator [2, 4]. The intent is to repeat the successes of cavity quantum electrodynamics (cQED) with atomic beams [17] implemented instead with microresonators and semiconductor optical transitions that can ostensibly be scaled using fabrication technologies developed for the microelectronics industry.

The first experimental step for such a system is to demonstrate a coherent interaction between a resonant optical mode and the two-dimensional (2D) excitonic transition. When the coherent interaction strength is greater than the photonic and excitonic losses, the system is said to be in the strong coupling regime manifesting as hybridized exciton-polariton modes. These polariton modes are generally observed via an anti-crossing in the spectrum of the resonator frequency and the excitonic transition, when one of the resonances is tuned across the other. For integrated nonlinear optics, the polariton then inherits the quantum features

of the excitonic transition which includes exciton-exciton interactions, lending to a Kerr-type optical nonlinearity from the polariton-polariton interaction. From this optical nonlinearity there exist theoretical proposals utilizing the TMD excitonic transition for quantum optical applications in single-photon nonlinear optics [18–20].

Several research groups have already observed exciton-polaritons using 2D TMD excitons with 2D planar resonators, including distributed Bragg reflector (DBR) cavities [21–24] and nonlocal metasurfaces [25]. 1D guided resonances in planar waveguides have also been used to study exciton-polaritons [26, 27]. An advantage of these types of resonators is the strong dispersion thanks in part to the lack of 3D confinement of the electromagnetic field. This dispersion allows the investigation of strong coupling via energy-momentum spectroscopy. In other words, by collecting light at different angles of emission or reflection from the resonator we can probe different resonance frequencies without the requirement of physically tuning the resonator. However, the lack of 3D confinement also implies a large mode volume. Hence, it would be difficult to realize a strong polariton-polariton interaction that is inversely proportional to the confinement area [18].

Zero-dimensional (0D) resonators can confine the electromagnetic field in all three spatial dimensions to a sub-wavelength mode volume. As a result of such strong resonant mode localization, the resonance is dispersionless and the exciton-resonator detuning must be modified by some other physical means. To date, curved fiber-DBR cavities are the only 0D platform that have demonstrated exciton-polaritons with 2D excitons [28, 29]. Here, a fixed DBR mirror and a mechanically movable fiber creates the cavity mode. The cavity length, and hence the cavity resonance frequency, is controlled by the spatial separation of the fiber and bottom DBR. The tuning of the cavity allows for direct observation of the avoided crossing associated with the formation of exciton-polariton modes. Recently, signatures of single-photon nonlinearity have been reported in a III-V quantum well system coupled to an optically confined mode of a fiber-DBR cavity [30, 31]. While these works provide remarkable proof of concept demonstrations with promising perspectives [32], the in-situ tuning advantage of a fiber-DBR cavity comes at the expense of a larger mode volume

as compared to a photonic crystal defect resonator [33, 34].

On-chip integrated 0D resonators, such as a photonic crystal defect resonator (PCDR), provide a means to confine light in a wavelength-scale mode volume while allowing many such resonators to couple to each other via evanescent fields [35]. In fact, TMDs coupled to PCDRs have already been used to demonstrate optically pumped lasing [5, 36], cavity enhanced electroluminescence [37], and second harmonic generation [38, 39]. TMD hetero-structures have also been integrated with PCDRs to demonstrate emission enhancement [40] and lasing [41].

However, no conclusive signature of a coherent interaction between TMD excitons and a small mode volume on-chip microresonator had been reported and the value of a coherent light-matter interaction strength g had not been estimated for any 2D excitonic transition, including III-V quantum wells coupled to an on-chip PCDR. The difficulties lie in the degradation of the quantum well excitonic transition due to etching, lack of in-situ tuning of on-chip resonators, and measuring the 0D resonator in a transmission configuration.

Strong coupling and subsequent single-photon nonlinear optics have been demonstrated in self-assembled quantum dots coupled to zero-dimensional (0D) cavity systems [42–45]. In a quantum dot, the exciton is confined in all three dimensions, which is defined as a 0D exciton. Similarly, in a PCDR [46] or a fiber-DBR cavity [47], light is confined at wavelength scale in all three dimensions, making these systems 0D cavities. While such 0D polaritons can provide the strongest nonlinearity, arising from the quantum anharmonicity induced by the 0D exciton [45, 48], practical limitations, such as limited range of cavity tuning and the stochastic nature of the position and wavelength of quantum dots, prevent the scalability of such a platform.

The importance of the strong coupling between the 2D excitonic transition and the microresonator stems from the enhancement of the exciton-exciton interaction due to the same increased electric field intensity mentioned in the previous section [18, 49]. The field enhancement is necessary to overcome the reduced Hamiltonian anharmonicity compared to the 0D excitonic transition. While many quantum optical effects have been predicted in

the 2D exciton-polariton systems [50, 51], the lack of excitonic wave function confinement in all three dimensions precluded a clear observation of single-photon nonlinearity (e.g., reaching the regime of polariton blockade under resonant excitation [18]). We emphasize that, assuming strong coupling is achieved, a small cavity mode volume is the primary figure of merit for maximizing the optical nonlinearity [52]. As such, on-chip 0D microresonators with a sub-wavelength mode volume coupled to a 2D excitonic transition can simultaneously provide a large light-matter interaction and a clear path to a scalable architecture for integrated nonlinear optics.

Chapter 2

TECHNOLOGY DEVELOPMENT

Dielectric microresonators and semiconducting transition metal dichalcogenides (TMDs) support optical resonances which are solutions of the wave equation and Schrödinger equation, respectively, subject to suitable boundary conditions. In this chapter I provide theoretical background for the physical manifestations of these solutions, known as quasinormal modes for dielectric microresonators and Wannier excitons for TMDs.

A modified polycarbonate-polydimethylsiloxane (PC-PDMS) transfer technique is then presented, which allows precise pickup and placement of vdW materials onto photonic integrated circuits (PICs). As mentioned in Kim et al [53], the contact area (i.e. the region of the PC film which is in contact with the substrate) of the standard dome stamp transfer method is limited to an approximately 50 µm x 50 µm area. The selectivity of the standard transfer method leaves detritus on the photonic integrated circuits that can destroy their optical properties. The contact area of the modified process can be two orders of magnitude smaller than the dome method. The efficacy of the new transfer process is demonstrated by placing WSe_2 onto a large-area silicon nitride spiral [54] and two different semiconductor monolayers (WSe_2, $MoSe_2$) onto neighboring silicon nitride ring resonators [55].

2.1 Dielectric microresonators

Photonic intergrated circuits (PICs) use wavelength-scale patterning of dielectric materials to confine and guide light via a refractive index contrast similar to the mechanism for total internal reflection. Dielectric microresonators, a component used in PICs, use constructive and destructive interference of the wave solutions of Maxwell's equations to enable confinement of the electromagnetic field in time.

2.1.1 Quasinormal modes

These quasinormal modes (QNMs), or resonant modes, of dissipative (non-Hermitian) electromagnetic resonators are time-harmonic solutions of the source-free, Maxwell's equations [56, 57]

$$[\mu_0 \mu_R(\mathbf{r}, \tilde{\omega}_\mu)]^{-1} \nabla \times \tilde{\mathbf{E}}_\mu(\mathbf{r}) = i\tilde{\omega}_\mu \tilde{\mathbf{H}}_\mu(\mathbf{r}) \tag{2.1}$$

$$[\epsilon_0 \epsilon_R(\mathbf{r}, \tilde{\omega}_\mu)]^{-1} \nabla \times \tilde{\mathbf{H}}_\mu(\mathbf{r}) = -i\tilde{\omega}_\mu \tilde{\mathbf{E}}_\mu(\mathbf{r}) \tag{2.2}$$

satisfying the Silver-Müller radiation condition

$$\hat{\mathbf{r}} \times \tilde{\mathbf{E}}(\mathbf{r}, \omega) \rightarrow \sqrt{\frac{\mu_0}{\epsilon_0 \epsilon_B}} \tilde{\mathbf{H}}(\mathbf{r}, \omega), \quad r \rightarrow \infty \tag{2.3}$$

$$\hat{\mathbf{r}} \times \tilde{\mathbf{H}}(\mathbf{r}, \omega) \rightarrow -\sqrt{\frac{\epsilon_0 \epsilon_B}{\mu_0}} \tilde{\mathbf{E}}(\mathbf{r}, \omega), \quad r \rightarrow \infty. \tag{2.4}$$

The radiation condition ensures the solution contains only outgoing waves [57–59]. $\tilde{\mathbf{E}}_\mu$ ($\tilde{\mathbf{H}}_\mu$) is the electric (magnetic) field, ϵ_0 (μ_0) is the permittivity (permeability) of free space, and ϵ_R (μ_R) is the relativity permittivity (permeability). At sufficiently large distances the relative permittivity and permeability are assumed to have constant background values, $\epsilon_R = \epsilon_B = n_B^2$ and $\mu_R = 1$. A finite-difference time-domain (FDTD) electromagnetic solver, such as Lumerical-Ansys, with perfectly matched layers can be used to calculate the QNMs by initially exciting the the resonant field with a short input pulse and simulating the resonator ring-down [60, 61].

The difficulty associated with the QNMs of dissipative electromagnetic resonators is their complex resonant frequency, $\tilde{\omega}_\mu = \omega_\mu - i\gamma_\mu$, used to define the resonator quality factor $Q_\mu = \omega_\mu/2\gamma_\mu$. Assuming a spherical outgoing wave where $\mathbf{E}(\mathbf{r}, t) \propto \exp[-i\tilde{\omega}_\mu(t - n_B|\mathbf{r}|/c)]/|\mathbf{r}|$, substitution of the complex resonant frequency leads to a spatially divergent far-field behavior, $\mathbf{E} \propto \exp[\gamma_\mu n_B|\mathbf{r}|/c]/|\mathbf{r}|$ [56, 62]. This field divergence necessarily leads to a difficulty making quantitative predictions from simulated mode field profiles. Specifically, for dissipative

resonators the volume integral used to define the normalization of the electromagnetic field is exponentially diverging. Compare this to the classical results of Hermitian resonators where the integration volume is defined by energy considerations, usually located at the physical boundaries of the resonator [63].

Methods have been established to regularize QNMs using FDTD electromagnetic solvers [62]. However, note that the divergent behavior of the QNM becomes significant at a distance r_{QNM} such that $(\gamma_\mu n_B/c)r_{QNM} \approx 1$. For a dielectric microresonator with a moderate quality factor, for example $Q = 10^4$, the field decay rate at visible frequencies of light ($\omega \approx 400$ THz) is approximately 10 GHz. With a background relative permittivity equal to that of free space ($\epsilon_B = n_B^2 = 1$) the divergent behavior of the QNM is important at distances beyond $r_{QNM} \approx 1 \times 10^4$ µm. From this we can infer the QNM for dielectric microresonators can be regularized by introducing a spatial cut-off of the integration volume [58, 61].

The zero-dimensional photonic crystal defect resonator (PCDR) in-line with an optical waveguide is an example of a dielectric microresonator that supports QNMs. The simplest one-dimensional photonic crystal is the infinite Bragg grating, with the center wavelength of the stop-band at $\lambda_B = 2\Lambda n_{eff}$, known as the Bragg wavelength [14, 63, 64]. $\Lambda = L_1 + L_2$ is the grating period and $n_{eff} = (n_1 L_1 + n_2 L_2)/(L_1 + L_2)$ is the average effective index (Fig. 2.1). The PCDR is, in essence, a Fabry-Perot optical cavity formed by distributed Bragg reflectors (DBRs). A $\pi/2$ phase shift defect with an optical length $\Lambda/2$ is inserted in the center of a finite Bragg grating to introduce resonant tunneling at the Bragg wavelength [14] (Fig. 2.2).

For monolithic fabrication of an in-plane PCDR on a dielectric substrate the mirror strength of the grating (a measure of the grating's reflectivity) is linearly apodized to reduce the out-of-plane scattering from coupling to radiation modes. We use the deterministic design outlined in Quan et al. [66, 67] for its high quality factor and strong coupling to the feeding waveguide. The former is essential for the strong coupling regime of the light-matter interaction and the latter for observation of polaritons in a transmission configuration.
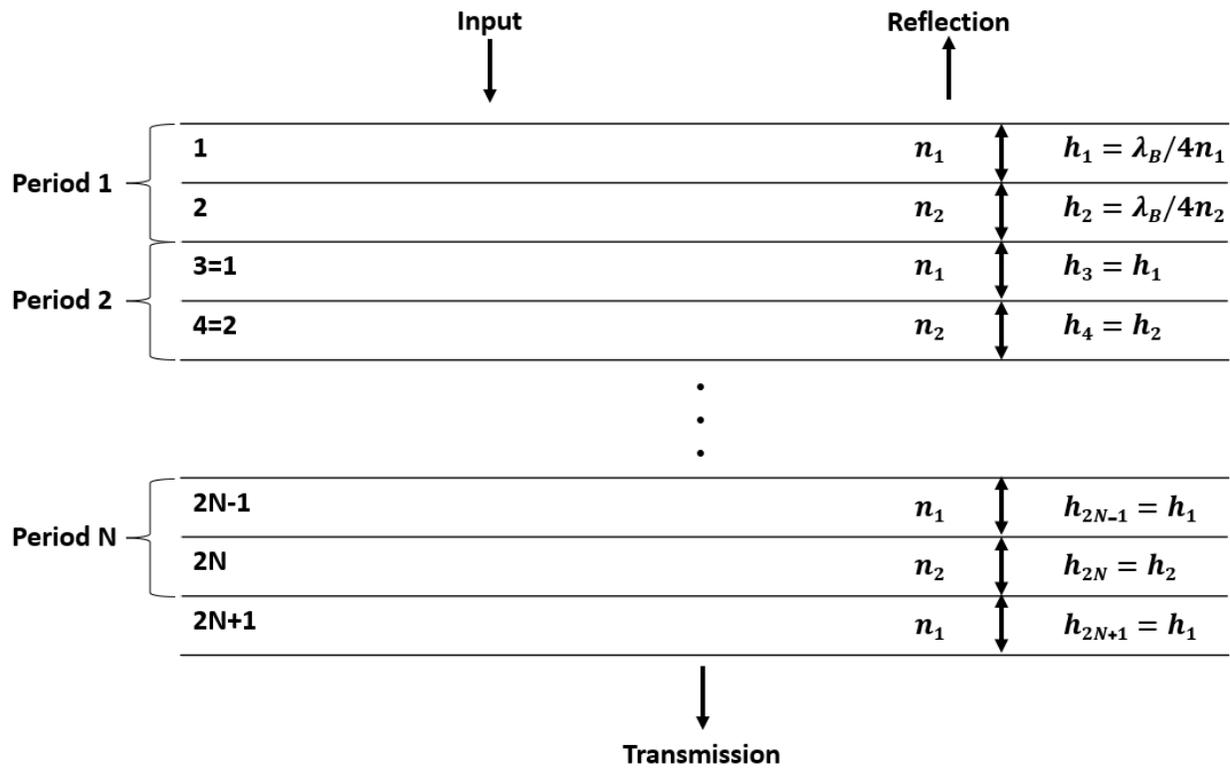
Figure 2.1: **Distributed Bragg reflector.** A distributed Bragg reflector (DBR) consisting of $2N + 1$ layers of alternating quarter-wavelength high and low index materials [65].
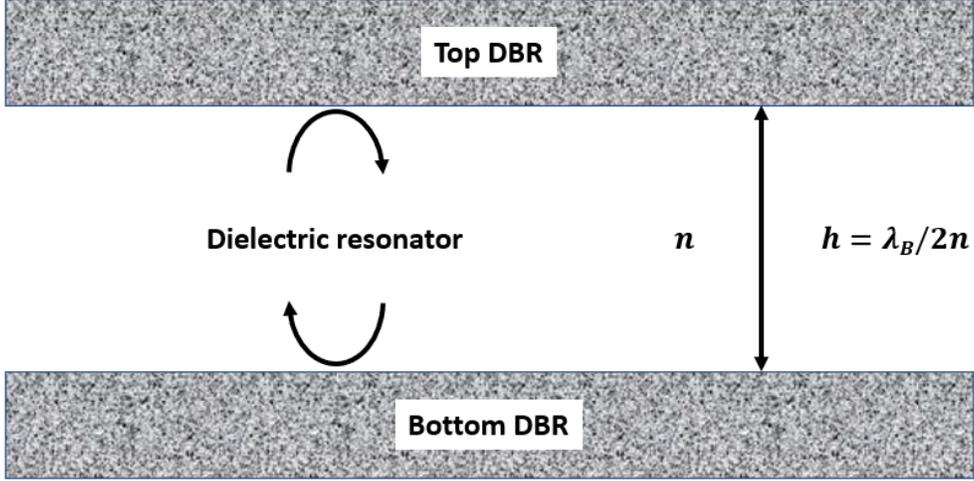
Figure 2.2: **Distributed Bragg reflector resonator.** A dielectric resonator formed by the inclusion of a $\pi/2$ phase shift defect within a distributed Bragg reflector (DBR). Alternatively, this can be understood in terms of a resonance formed between two DBRs.

2.1.2 Input-output relations

In-line resonator

To understand the transmission properties of the in-line resonator, such as the PCDR, consider that the Hamiltonian of a single-mode electromagnetic resonator is commonly described by that of a free harmonic oscillator of the form

$$\hat{H}_C = \hbar \sum_{\mathbf{k}} \omega_{\mathbf{k}} \hat{a}_{\mathbf{k}}^\dagger \hat{a}_{\mathbf{k}}, \tag{2.5}$$

$\hat{a}_{\mathbf{k}}^\dagger$ is the bosonic creation operator of photon with momentum $\mathbf{k}$. For a dispersionless resonator with no in-plane (perpendicular to the propagation direction of the waveguide) photon momentum this reduces to

$$\hat{H}_C = \hbar \tilde{\omega}_C \hat{a}^\dagger \hat{a}, \tag{2.6}$$

where $\tilde{\omega}_C = \omega_C - i\kappa$ is the complex resonant frequency of the resonant mode which includes the intrinsic radiative loss κ. Following the input-output theory of Collett and Gardiner [68, 69], the quantum Langevin equation describing the internal mode for a two-sided, single-mode resonator with a single external driving field is

$$\frac{d\hat{a}}{dt} = -\frac{i}{\hbar}[\hat{a}, \hat{H}_C] - \frac{\gamma_1}{2}\hat{a} - \frac{\gamma_2}{2}\hat{a} + \sqrt{\gamma_1}\hat{a}_{in}. \tag{2.7}$$

$\gamma_{1,2}$ are the resonator damping constants for the two sides of the resonator. $\hat{a}_{in}$ is the external driving field coupled to the resonator through γ_1. The transmitted field $\hat{a}_{out}$ is coupled to the resonator via γ_2, as described by the equation

$$\hat{a}_{out} = \sqrt{\gamma_2}\hat{a}. \tag{2.8}$$

Inserting Eq. (2.6) into Eq. (2.7) and computing the commutator gives

$$\frac{d\hat{a}}{dt} = -i\tilde{\omega}_C\hat{a} - \frac{\gamma_1}{2}\hat{a} - \frac{\gamma_2}{2}\hat{a} + \sqrt{\gamma_1}\hat{a}_{in}. \tag{2.9}$$

In the frequency domain the internal mode operator is taken to be

$$\tilde{a}(\omega) = \frac{1}{\sqrt{2\pi}} \int_{-\infty}^{\infty} e^{i\omega t}\hat{a}(t)dt. \tag{2.10}$$

Eq. (2.9) in the frequency domain is then

$$-i\omega\tilde{a} = -i\tilde{\omega}_C\tilde{a} - \frac{\gamma_1}{2}\tilde{a} - \frac{\gamma_2}{2}\tilde{a} + \sqrt{\gamma_1}\tilde{a}_{in}. \tag{2.11}$$

The operator $\tilde{a}$ can be solved in terms of the operator $\tilde{a}_{in}$

$$\tilde{a} = \frac{\sqrt{\gamma_1}}{-i(\omega - \tilde{\omega}_C) + \frac{1}{2}(\gamma_1 + \gamma_2)}\tilde{a}_{in} \tag{2.12}$$

This can be substituted into Eq. (2.8) to find

$$\left|\frac{\tilde{a}_{out}}{\tilde{a}_{in}}\right|^2 = \left|\frac{\sqrt{\gamma_1\gamma_2}}{-i(\omega - \tilde{\omega}_C) + \frac{1}{2}(\gamma_1 + \gamma_2)}\right|^2 \tag{2.13}$$

Substituting $\tilde{\omega}_C = \omega_C - i\kappa$ we get

$$\left|\frac{\widetilde{a}_{out}}{\widetilde{a}_{in}}\right|^2 = \left|\frac{\sqrt{\gamma_1 \gamma_2}}{-i(\omega - \omega_C) + \kappa + \frac{1}{2}(\gamma_1 + \gamma_2)}\right|^2 \tag{2.14}$$

Simplification of this result leads to the standard transmitted spectrum of an in-line resonator

$$T(\omega) = \left|\frac{\widetilde{a}_{out}}{\widetilde{a}_{in}}\right|^2 = \frac{\gamma_1 \gamma_2}{(\Delta\omega)^2 + (\kappa + \frac{1}{2}(\gamma_1 + \gamma_2))^2} \tag{2.15}$$

with $\Delta\omega = \omega - \omega_C$ the detuning of the driving external field frequency ω, such as a laser, from the resonator frequency ω_C. For a symmetric resonator with $\gamma = \gamma_1 = \gamma_2$ this reduces to

$$T(\omega) = \left|\frac{\widetilde{a}_{out}}{\widetilde{a}_{in}}\right|^2 = \frac{\gamma^2}{(\Delta\omega)^2 + (\kappa + \gamma)^2} \tag{2.16}$$

This result is in accord with analysis based on scattering theory [70]. $T_{max} = \left(\frac{\gamma}{\kappa+\gamma}\right)^2$ is the maximum transmission efficiency of the in-line resonator at zero detuning ($\Delta\omega = 0$) for a given instrinsic radiative loss (κ) and waveguide-coupled resonator damping (γ).

Side-coupled resonator

Single-mode: Alternatively, the side-coupled resonator geometry has the advantage it partially decouples the intrinsic cavity quality factor and field profile from the transmission properties of the resonator. The quantum Langevin equation describing the internal mode for a side-coupled, single-mode resonator with a single external driving field is [71, 72]

$$\frac{d\hat{a}}{dt} = -\frac{i}{\hbar}[\hat{a}, \hat{H}_C] - i\sqrt{\gamma_{SC}}\hat{a}_{in}. \tag{2.17}$$

The resonator loss γ_{SC} associated with the presence of the side-coupled waveguide leads to a modified complex frequency of the resonant mode $\tilde{\omega}_C = \omega_C - i(\kappa + \gamma_{SC})$. The transmitted field $\hat{a}_{out}$ is coupled to the resonator via γ_{SC}, as described by the equation

$$\hat{a}_{out} = \hat{a}_{in} - i\sqrt{\gamma_{SC}}\hat{a}. \tag{2.18}$$

Following identical steps which concluded with Eq. (2.15), the transmitted spectrum of a side-coupled resonator is

$$T(\omega) = \frac{(\Delta\omega)^2 + \kappa^2}{(\Delta\omega)^2 + (\kappa + \gamma_{SC})^2}. \tag{2.19}$$

Again, this result is in accord with analysis based on scattering theory [70].

Two degenerate modes: The quantum Langevin equations describing the two degenerate internal modes for a side-coupled resonator with a single external driving field are

$$\frac{d\hat{a}_1}{dt} = -\frac{i}{\hbar}[\hat{a}_1, \hat{H}_C] - i\sqrt{\gamma_1}\hat{a}_{in} \tag{2.20}$$

$$\frac{d\hat{a}_2}{dt} = -\frac{i}{\hbar}[\hat{a}_2, \hat{H}_C] - i\sqrt{\gamma_2}\hat{a}_{in}. \tag{2.21}$$

The Hamiltonian describing the two modes is now

$$\hat{H}_C = \hbar\tilde{\omega}_C\hat{a}_1^\dagger\hat{a}_1 + \hbar\tilde{\omega}_C\hat{a}_2^\dagger\hat{a}_2 + \hbar\beta^*\hat{a}_1\hat{a}_2^\dagger + \hbar\beta\hat{a}_1^\dagger\hat{a}_2, \tag{2.22}$$

$\hat{a}_{1,2}$ are the bosonic annihilation operators for the resonator modes. β is a mode coupling between the two resonator modes [73]. The resonator loss associated with the presence of the side-coupled waveguide for the two modes leads to a modified complex frequency of the resonant mode $\tilde{\omega}_C = \omega_C - i(\kappa + \frac{1}{2}(\gamma_1 + \gamma_2))$. The transmitted field $\hat{a}_{out}$ is coupled to the resonator via γ_{SC}, as described by the equation

$$\hat{a}_{out} = \hat{a}_{in} - i\sqrt{\gamma_1}\hat{a}_1 - i\sqrt{\gamma_2}\hat{a}_2. \tag{2.23}$$

Following identical steps which concluded with Eq. (2.15) and Eq. (2.19), the complex transmittance of the two degenerate modes is found to be

$$t(\omega) = \frac{\tilde{a}_{out}}{\tilde{a}_{in}} = \frac{(\omega - \tilde{\omega}_C)((\omega - \tilde{\omega}_C) - i(\gamma_1 + \gamma_2)) - i\sqrt{\gamma_1\gamma_2}(\beta + \beta^*) - |\beta|^2}{(\omega - \tilde{\omega}_C)^2 - |\beta|^2} \tag{2.24}$$

In the absence of coupling between the degenerate modes ($\beta = 0$), and the couplings between each resonator mode and the waveguide are equally strong ($\gamma = \gamma_1 = \gamma_2$), the transmission spectrum reduces to

$$T(\omega) = \left| \frac{\widetilde{a}_{out}}{\widetilde{a}_{in}} \right|^2 = \frac{(\Delta\omega)^2 + (\kappa - \gamma)^2}{(\Delta\omega)^2 + (\kappa + \gamma)^2} \tag{2.25}$$

This result is in accord with analysis based on scattering theory [70] and applies to both standing wave resonators (e.g., a photonic crystal defect resonator) and traveling wave resonators (e.g., a whispering gallery mode resonator). There exists a critical coupling where the intrinsic radiative loss is equal to the resonator-waveguide coupling ($\kappa = \gamma$) such that transmission is zero at the resonant frequency of the degenerate resonator modes.

2.2 Two-dimensional excitonic transition

An exciton is a quasiparticle excitation consisting of an electron and hole bound by the Coulomb force. The phenomenological approach to treating the Wannier exciton in TMDs is the effective mass Hamiltonian which is identical to that of the hydrogen atom with the reduced mass defined from the effective mass of the electron and hole. In this section I sketch the second quantized derivation of the Wannier exciton for motivating the excitonic operator used in later chapters.

The one-pair subspace of the electron-hole Hamiltonian $H_{eh} = H_e + H_h + V_{eh}$ describing semiconductors is [74]

$$H_e = \sum_{\mathbf{k}} \varepsilon_{\mathbf{k}}^{(e)} a_{\mathbf{k}}^\dagger a_{\mathbf{k}} \tag{2.26}$$

$$H_h = \sum_{\mathbf{k}} \varepsilon_{\mathbf{k}}^{(h)} b_{\mathbf{k}}^\dagger b_{\mathbf{k}} \tag{2.27}$$

$$V_{eh} = -\sum_{\mathbf{q} \neq 0} V_{\mathbf{q}} \sum_{\mathbf{k}_1 \mathbf{k}_2} a_{\mathbf{k}_1 + \mathbf{q}}^\dagger b_{\mathbf{k}_2 - \mathbf{q}}^\dagger b_{\mathbf{k}_2} a_{\mathbf{k}_1} \tag{2.28}$$

$a_{\mathbf{k}}^\dagger$ and $\varepsilon_{\mathbf{k}}^{(e)}$ are the electron creation operator and electron kinetic energy, respectively. $b_{\mathbf{k}}^\dagger$

and $\varepsilon_{\mathbf{k}}^{(h)}$ are the hole creation operator and hole kinetic energy, respectively. And V_{eh} is the Coulomb interaction between the electron and hole with $V_{\mathbf{q}} = e^2/\epsilon_0 \epsilon_{sc} L^3 q^2$ for two- and three-dimensional systems. ϵ_{sc} is the dielectric constant of the semiconductor, L is a quantization volume, and q is the transferred momenta between the electron and hole states.

The correlated state $|i\rangle$ of an electron-hole pair is an eigenstate of the Schrödinger equation in the presence of the Coulomb interaction

$$(H_e + H_h + V_{eh} - E_i)\,|i\rangle = 0. \tag{2.29}$$

The correlated pair state

$$|i\rangle = B_i^\dagger |v\rangle \tag{2.30}$$

defines the exciton creation operator $B_i^\dagger$. The exciton creation operator can be written in terms of the electron and hole creation operators

$$B_{\mathbf{Q}_i v_i}^\dagger = \sum_{\mathbf{p}} f_{\mathbf{p}}^{(\nu_i)} a_{\mathbf{p}+\gamma_e \mathbf{Q}_i}^\dagger b_{-\mathbf{p}+\gamma_h \mathbf{Q}_i}^\dagger \tag{2.31}$$

$f_{\mathbf{p}}^{(\nu_i)}$ is the relative motion wave function of the exciton satisfying the hydrogen-like Schrödinger equation, also known as the Wannier equation,

$$\frac{\mathbf{p}^2}{2\mu_X} f_{\mathbf{p}}^{(\nu_i)} - \sum_{\mathbf{q}\neq 0} V_{\mathbf{q}} f_{\mathbf{p}-\mathbf{q}}^{(\nu_i)} = \varepsilon_{v_i} f_{\mathbf{p}}^{(\nu_i)}. \tag{2.32}$$

The free electron ($\mathbf{k}_e = \mathbf{p} + \gamma_e \mathbf{Q}_i$) and free hole ($\mathbf{k}_h = -\mathbf{p} + \gamma_h \mathbf{Q}_i$) momenta define the center-of-mass momentum ($\mathbf{Q}_i$) and relative momentum ($\mathbf{p}$) with $\gamma_e = 1 - \gamma_h = m_e/(m_e + m_h)$. The reduced mass is $\mu_X^{-1} = m_e^{-1} + m_h^{-1}$.

The two-dimensional exciton bound-state energies from the solution of Eq. (2.32) are [75]

$$E_n = -E_0 \frac{1}{(n+1/2)^2} \tag{2.33}$$

with $n = 0, 1, ...$ where $E_0 = \frac{e^2}{8\pi\epsilon_0 a_B}$ is the exciton Rydberg energy and $a_B = \frac{4\pi\hbar^2\epsilon_0}{e^2\mu_X}$ is the exciton Bohr radius. Note, the binding energy of the exciton ground state in three dimensions is E_0 and $4E_0$ in two dimensions due to out-of-plane quantum confinement of the Bohr radius.

Transition metal dichalcogenides [76] are van der Waals (vdW) materials similar to graphene that can be mechanically exfoliated from bulk crystals or chemical grown. When thinned to a single monolayer the MX_2 TMDs with $M = Mo, W$ and $X = S, Se$ become direct bandgap semiconductors which support excitonic transitions. Due to the large out-of-plane confinement the typical exciton binding energies are on the order of 0.5 meV. The exciton binding energies are larger than the thermal energy $k_BT \approx 25$ meV at room temperature allowing for observation of excitonic photoluminescence even at elevated temperatures. Although the excitonic transition in monolayer TMDs conforms well to the effective mass Hamiltonian described in Eq. (2.32) the Coulomb interaction must be replaced by a electron-hole interaction that accounts for nonlocal charge screening [77–79]. In the 2D TMD material family, monolayer $MoSe_2$ is particularly interesting as the only one with the the neutral exciton as the ground state optical transition [80].

2.3 Material integration

Having motivated the design of dielectric microresonators and the existence of an excitonic optical transition in TMDs it is important to first establish a deterministic transfer method for marrying the two material platforms into a single device. Mechanically exfoliated and small-area chemical vapor deposition (CVD) grown vdW materials are pervasive in laboratory experiments due to their high quality and ease of device integration [81, 82]. Various transfer techniques have been devised to facilitate rapid prototyping of vdW material heterostructures assembled from randomly located, micron-sized flakes that are often surrounded by unwanted bulk material [53, 83, 84]. For pure material studies the surrounding bulk materials do not pose a serious problem because there are no extended structures to avoid in the transfer process. In the realm of nanophotonics, however, stray bulk material can modify the optical properties of the structure under study. Moreover, many of these contaminants cannot be

removed easily via etching or cleaning in solvents, often leading to ruined devices. Hence, a local transfer technique with improved monolayer discrimination is desired for high-yield vdW material integrated nanophotonic structures.

2.3.1 Experimental procedure

Figure 2.3(a) and figure 2.3(b) is an example of the standard dome transfer method with a zoomed-in nanobeam cavity to illustrate the scale of a photonic device [34]. The monolayer was successfully transferred onto the nanobeam cavity. Note the monolayer is invisible under an optical microscope due to the poor optical contrast on the silicon nitride substrate. The dome stamp contaminated the waveguide with bulk material and tape residue which can significantly alter the transmission properties of the devices, sometimes to an extent where no transmission through the waveguide can be measured. The local transfer method described below allows for the precise pickup and placement of vdW material flake without the usual accompanying bulk material pieces.

The hemispherical dome stamp fabrication begins by preparing a 2-3 mm layer of cured PDMS (SYLGARD™184 Silicone Elastomer) cut into 6 mm diameter rounds. A second batch of PDMS is mixed from the silicone elastomer base with the curing agent, and placed in vacuum for 20 minutes for degassing. The liquid PDMS is then pipetted onto the round layer to form a hemisphere under the surface tension of the liquid. The domes are cured by leaving them in vacuum for 24 hours (Fig. 2.3(c)).

The PC film (Sigma Aldrich® Poly(Bisphenol A carbonate), 7% solution in chloroform) is secured to the hemispherical PDMS stamp using Scotch® tape with a hole punched into it as a window (Fig. 2.3(d)). The sample stage is first set to 125 °C (Fig. 2.3(f)-1) and always under vacuum to avoid picking up the chip. Under an optical microscope, the dome stamp is lowered into minimal contact with the sample stage (Fig 2.3(f)-2). An SU-8 chip is used with pillars of varying diameters for the sample stage as a visual reference in the point formation. The dome is offset from the pillar, so it does not interfere with the melting PC. The SU-8 chip is not essential for the PC point formation. It is solely a pragmatic solution to making

20
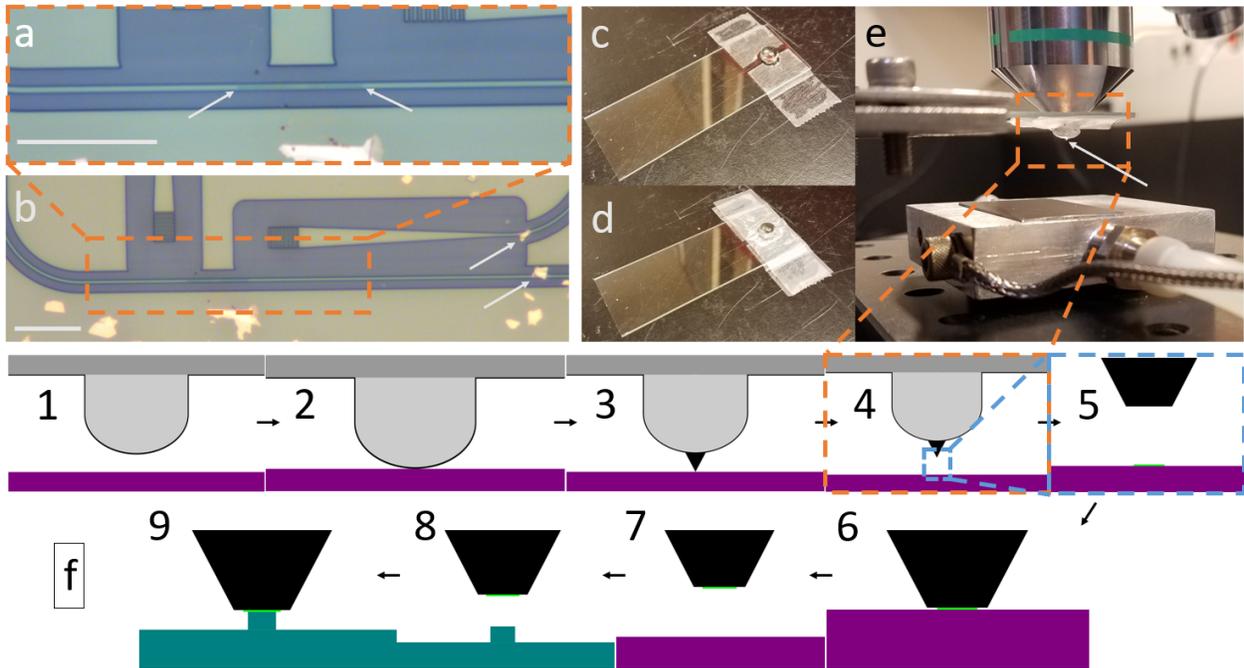
Figure 2.3: **Material transfer schematic.** a) 2D material transferred onto a nanobeam cavity indicated by the arrows. The monolayer material is not visible on the SiN subtrate. b) Bulk material on waveguides indicated by the arrows. Scale bars are 10 µm. c) Dome stamp on a glass slide. d) PC film secured to the dome stamp with Scotch® tape. e) ≈ 1 mm drawn PC point indicated by the arrow. f) Visual schematic of the procedure described in the text. Steps numbered 1-9. Purple is the stage substrate (e.g. SU-8 or SiO$_2$) and teal is the SiN waveguide. Dark gray is the glass slide, light gray is the PDMS dome, and black is the PC film. Green is the vdW material.
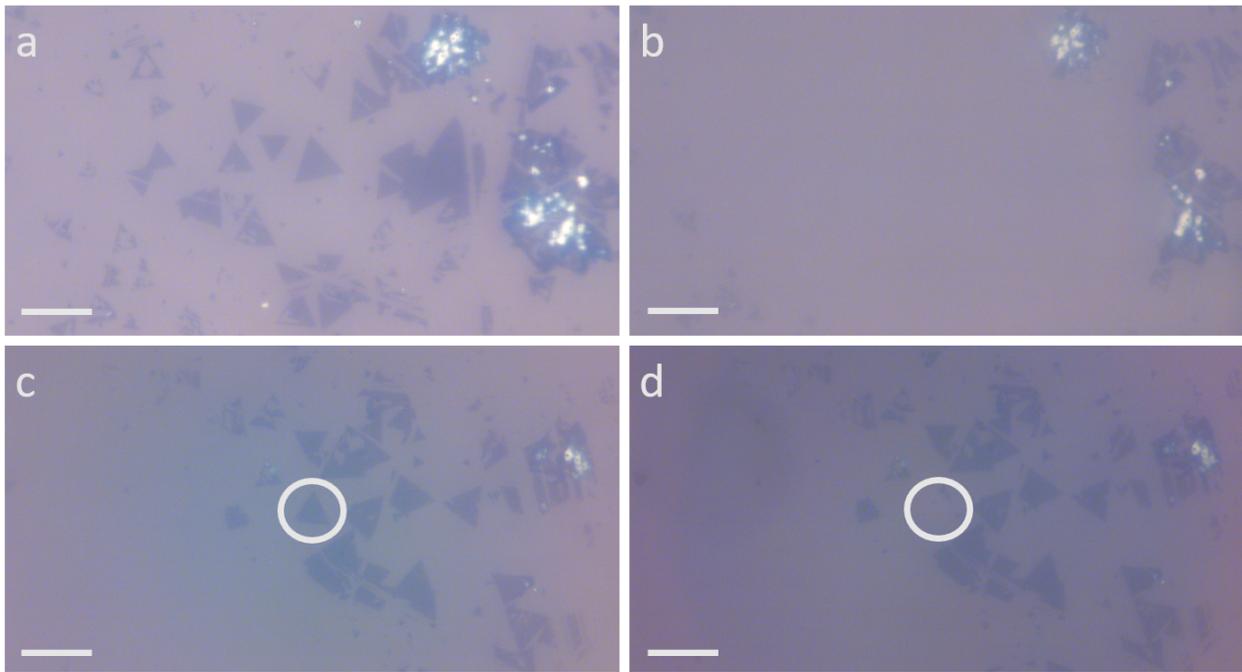
Figure 2.4: **Material transfer example.** a) Before pickup - CVD grown 2D material on SiO$_2$. b) After pickup with PC dome - CVD grown 2D material on SiO$_2$. Any materials picked up will be deposited onto the nanophotonic device. c) Before pickup – CVD-grown 2D material on SiO$_2$. d) After pickup with PC point – CVD-grown 2D material on SiO$_2$ without the removed monolayer WSe$_2$ triangle. A small sliver of the monolayer's edge is left behind. Scale bars are 10 µm.

a point with the same diameter as the monolayer sample to prevent picking up additional material. The sample stage is then heated to 160 ℃. After the stage equilibrates to the new temperature, the sample stage temperature is again set to 125 ℃. As the sample stage decreases towards the lower temperature, the dome stamp is drawn away from the sample stage to separate the PDMS stamp from the PC film, which will still be adhered to the sample stage. The dome stamp is continuously pulled away from the substrate as a point is drawn in the PC film commensurate with the monolayer sample (Fig. 2.3(f)-3). The point should be formed before the sample stage reaches the polycarbonate glass transition temperature (147 ℃). It is imperative to intentionally pull the newly formed point away from the stage after the sample stage crosses the glass transition temperature (Fig. 2.3(e) and Fig. 2.3(f)-4).

During pickup of the monolayer it is important to ensure that the monolayer sample is centered on the microscope objective along with the newly formed point (Fig. 2.3(f)-5). As the hemispherical PDMS dome itself acts as a lens, the heated stage position has to be adjusted to maintain the monolayer sample in the focal plane of the objective. The point will manifest as a white disk. Pickup is performed by contacting the point to the monolayer (Fig. 2.3(f)-6 and Fig. 2.3(f)-7).

Finally, to transfer the monolayer onto a photonic device the point is again brought close to the surface (Fig. 2.3(f)-8). Due to the suspended nature of the PC point, melting can cause the point to droop unpredictably. For precise placement of the monolayer it is easiest to rapidly lower the PDMS dome stamp into contact with the monolayer to anchor it to the sample substrate (Fig. 2.3(f)-9). The temperature of the sample stage is then raised to 180 ℃ to detach the PC as a sacrificial layer from the PDMS stamp. The PC film is dissolved in chloroform for 12 hours followed by a 30 minute isopropanol bath.

The main limitation of the dome stamp is that as the PC dome is lowered to a close enough distance that the Newton's rings can be seen, the dome will suddenly contact the substrate with the previously mentioned 50 µm x µm area contact area (Fig. 2.4(a) and Fig. 2.4(b)). Anything in contact with the PC film will likely be picked up and transferred onto the photonic device. By using the described local transfer method, it is possible pick up,

for example, a single 10 µm^2 triangle of CVD-grown monolayer WSe$_2$ heavily surrounded by unwanted material (Fig. 2.4(c) and Fig. 2.4(d)).

2.3.2 Experimental results and discussion

I first demonstrated the modified transfer method with the integration of WSe$_2$ onto a non-resonant nanophotonic device - a large-area silicon nitride (SiN) spiral (Fig. 2.5(a)). Due to its large area, the transmission spectrum is known to be sensitive to contaminants [85]. Then, resonant photonic devices were demonstrated by the dual integration of two different semiconductor monolayers (WSe$_2$, MoSe$_2$) onto neighboring SiN ring resonators. As the two monolayers are integrated in separate transfer steps the samples can be integrated as a heterostructure or onto separate devices depending on the desired experiment.

The underlying nanophotonic devices were fabricated using a 220 nm thick SiN membrane grown via LPCVD on 4 µm of thermal oxide on silicon. The samples were obtained from commercial vendor Rogue Valley Microelectronics. Roughly 400 nm of Zeon ZEP520A was spin-coated onto the silicon nitride chip which was coated with a thin layer of Pt/Au that served as a charging layer. The resist was then patterned using a JEOL JBX6300FX electron-beam lithography system with an accelerating voltage of 100 kV. The pattern was transferred to the SiN using a reactive ion etch (RIE) in CHF$_3$/O$_2$ chemistry.

Photoluminescence (PL) measurements [86] were conducted by exciting the monolayers with a 632 nm HeNe laser. The resulting emission was collected with a free-space confocal microscopy setup and measured in a spectrometer. The spectrometer was a Princeton Instruments IsoPlane SCT-320 Imaging Spectrograph. The transmission spectrum was measured by exciting a grating coupler with a supercontinuum laser (Fianium WhiteLase Micro) and collecting from the other grating coupler (Fig. 2.5(a), top right inset). For cavity-coupled PL [6] the sample was directly excited with the HeNe laser and the resulting emission was collected from a grating coupler using a pinhole in the image plane of the confocal microscope. To obtain high signal-to-noise ratio PL the sample was cooled down to 80K using liquid nitrogen in a continuous flow cryostat (Janis ST-500).
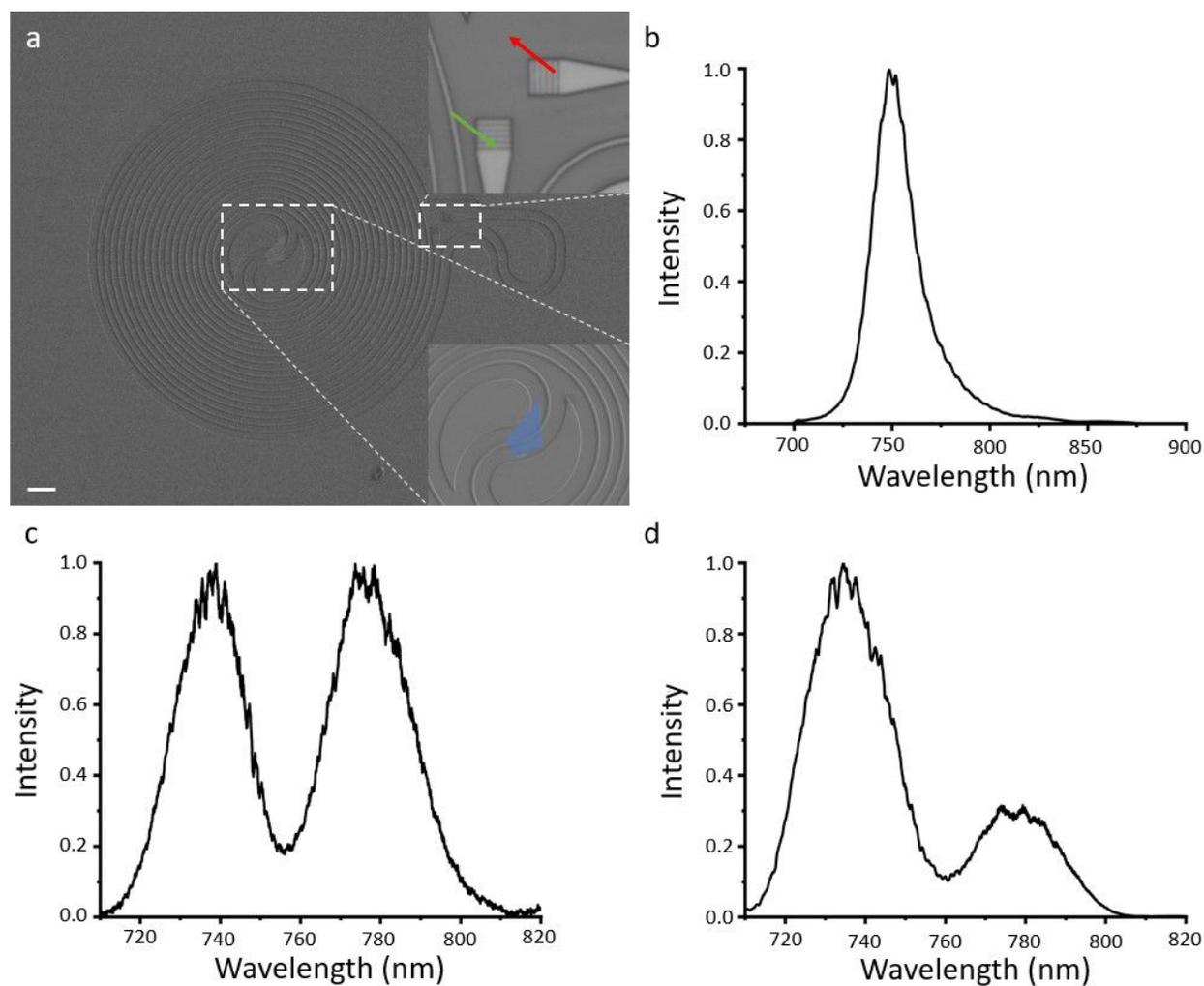
Figure 2.5: **Silicon nitride spiral transfer.** a) SEM image of a silicon nitride spiral. The bottom right inset is a false-color SEM of the integrated monolayer WSe$_2$. The top right inset is the grating couplers (green - excitation, red - collection). Scale bar is 10 µm. b) Room-temperature PL of the monolayer WSe$_2$ integrated onto the silicon nitride spiral. c) Transmission spectrum for the silicon nitride spiral. d) Transmission spectrum for the silicon nitride spiral with the integrated monolayer WSe$_2$.
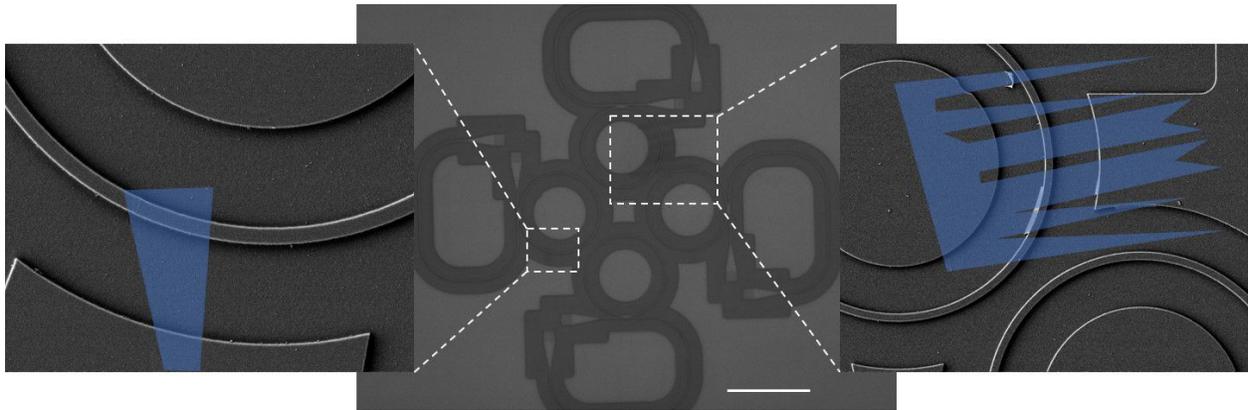
Figure 2.6: **Silicon nitride ring resonator transfer.** Optical image of exfoliated WSe$_2$ and MoSe$_2$ monolayers integrated onto the left and top ring resonators, respectively, with false-color SEM images of the integrated monolayers. Scale bar is 10 µm.

The room-temperature PL with a strong excitonic peak of the WSe$_2$ monolayer integrated onto the SiN spiral (Fig. 2.5(b)) establishes the presence of the vdW material on the waveguide [77]. The primary peak is attributed to neutral exciton emission, which is indicative of a direct bandgap, semiconducting material when the TMD vdW materials are exfoliated as monolayers. The secondary sidebands are likely due to defects or trions [28, 87]. The before and after transmission spectrum (Fig. 2.5(c) and Fig. 2.5(d), respectively) for the SiN spiral waveguide integrated with the monolayer WSe$_2$ illustrates the contamination-free nature of the transfer process. Significant contamination would prevent any transmission spectrum from being measured. The envelope modulation of the spectrum is due to the frequency-dependent coupling efficiency of the grating couplers. The relative amplitude change between the two features in the spectrum is likely due to the angular dependence of the grating couplers. As the measurement is done before and after the transfer - which requires removing the sample from the optical setup - the angular alignment of the confocal microscope objective to the grating coupler will be slightly different [14].

The method can be extended to integrate vdW materials to disjoint but proximate vdW

material photonic devices (Fig. 2.6). The four SiN ring resonators were each separated by 1 µm to ensure no coupling between cavities. Each cavity can be independently addressed by input and output grating couplers. Again, the PL of the WSe_2 and $MoSe_2$ (Fig. 2.7(a) and Fig. 2.7(d), respectively) establishes the presence of the monolayers. The low-temperature transmission spectrum for the ring resonators (Fig. 2.7(b) and Fig. 2.7(e)) with the integrated monolayers illustrates a contamination-free transfer. The dips in transmission correspond to the resonance in the ring resonators. The separation between the modes corresponds to the free spectral range of the ring resonator. The PL of the WSe_2 and $MoSe_2$ coupled to the evanescent field of the ring resonators collected from the grating coupler (Fig. 2.7(c) and Fig. 2.7(f), respectively) was amplified at the cavity resonances.

2.3.3   Conclusion

A method was presented to facilitate the integration of vdW materials onto photonic devices that require minimal contamination from bulk material. A PL measurement was used to identify the presence of vdW materials on the photonic devices. The transmission spectrum of the SiN spiral integrated with a monolayer material demonstrates the contamination-free nature of the described transfer method. The integration of two different transition metal dichalcogenide monolayers onto neighboring SiN ring resonators demonstrates the capability to manually scale the fabrication of devices for rapid prototyping. This local transfer technique can potentially enable a lithographically defined quantum emitter [88, 89] deterministically integrated onto a nanocavity, which can reach the few-photon nonlinear optical regime [20, 30, 31] for applications in neuromorphic photonics [90, 91] and quantum many-body simulation [92, 93].
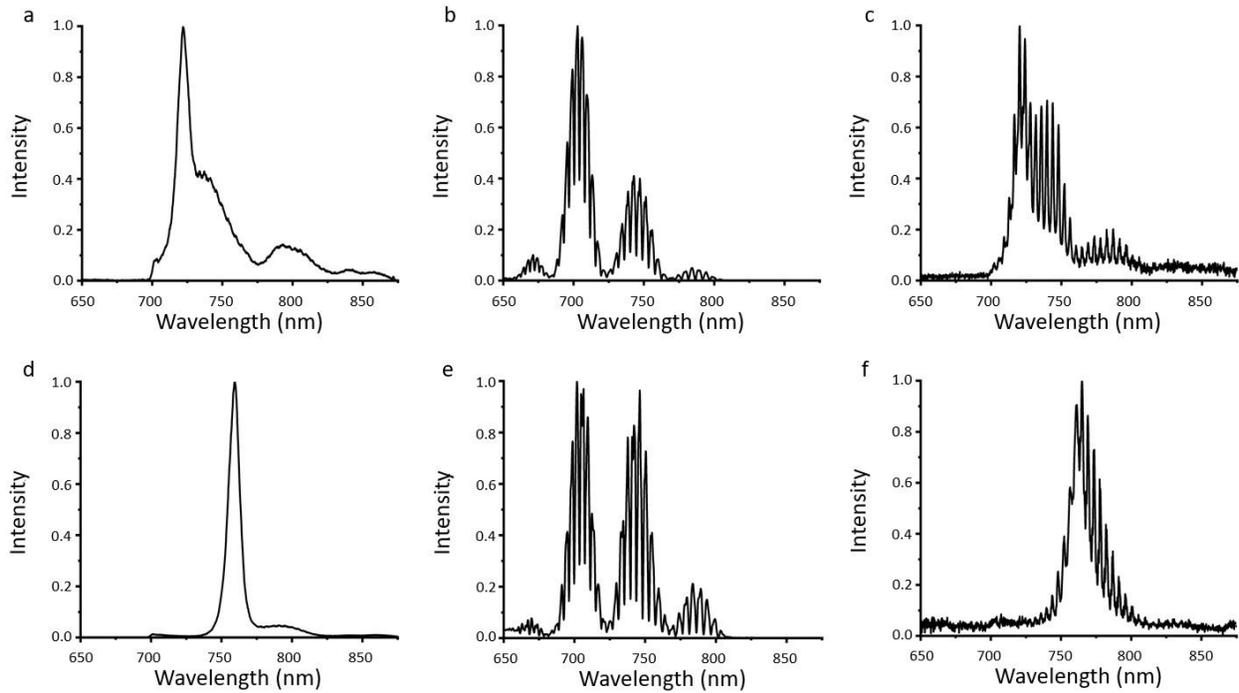
Figure 2.7: **Ring resonator spectra with integrated monolayer WSe$_2$ and MoSe$_2$.** a) PL of the integrated WSe$_2$ monolayer at 80 K. b) Transmission spectrum for the ring resonator with the integrated monolayer WSe$_2$. c) Cavity-coupled PL of the integrated monolayer WSe$_2$ on the ring resonator. d) PL of the integrated MoSe$_2$ monolayer at 80 K. e) Transmission spectrum for the ring resonator with the integrated monolayer MoSe$_2$. f) Cavity-coupled PL of the integrated monolayer MoSe$_2$ on the ring resonator. The baseline below the cavity resonance peaks in c and f is due to background PL.

Chapter 3

LIGHT-MATTER INTERACTION

I derive a compact expression for the light-matter interaction strength between a single quasinormal mode (QNM) of a dielectric microresonator and the two-dimensional excitonic transition. The theoretical result of the light-matter interaction strength is applied to the neutral exciton in a monolayer transition metal dichalcogenide (TMD) (MoSe$_2$) evanescently coupled to a silicon nitride, in-line photonic crystal defect resonator (PCDR). An optimal spatial extent of the monolayer TMD that maximizes the light-matter interaction strength was found due to the competition between minimizing the excitonic envelope function area and maximizing the total integrated field. The theoretical estimate was then experimentally corroborated by demonstration of a dispersive shift in the cavity transmission spectrum observed as the exciton is temperature-tuned near the QNM.

An on-substrate PCDR was utilized to ensure mechanical stability needed for the two-dimensional (2D) material transfer process. The microresonator was fabricated in silicon nitride (SiN) used for its large optical bandgap (necessary for the frequencies of the excitonic transition in TMDs) and a small thermo-optic coefficient. The latter is essential for the temperature tuning utilized in the demonstration of a coherent interaction. Otherwise the temperature dependence of the dispersive shift must be deconvolved from the temperature shift of the QNM. In comparison, an encapsulating polymer on the microresonator can have a significant effect on the resonant frequency [94].

The system was probed in transmission with the QNM red-detuned with respect to the excitonic transition because as the cavity-coupled photoluminescence is known to be affected by exciton-phonon interactions [95], discussed in chapter 4. The QNM was measured at large exciton-cavity detunings due to a significant increase in insertion loss of the QNM in

transmission at small detunings [96]. The extracted light-matter interaction strength from the dispersive shift was $\hbar g \approx 6.5$ meV for an estimated cooperativity $C = 4g^2/(\kappa_0 \gamma_0') \sim 4.0$, in which $\hbar \gamma_0' = 11.11$ meV is the measured broadening of the TMD exciton at 80 K, and $\hbar \kappa_0 = 3.8$ meV is the bare photonic mode linewidth measured without the TMD material. The cooperativity is a measure of the polariton mode splitting visibility, where at $C > 1$ the splitting is greater than the respective linewidths of the upper and lower polariton modes. This experimental result compares favorably to the theoretical estimate of $\hbar g \approx 4.2$ meV. The cooperativity can be further enhanced to $C \sim 380$ at 4 K due to reduction of the exciton decay rate and by increasing the QNM quality factor to 10^4, which is well within the reach of current fabrication technology.

By applying an input-output theory approach to calculate the cavity transmission it is shown that the transmission efficiency drops significantly for a resonant exciton-cavity system. The predicted transmission suppression agrees with experimental observations [97]. Alternatively, it is shown that strong coupling can be probed in a transmission configuration by exploiting a side-coupled cavity.

3.1 Exciton-photon coupling

3.1.1 Second quantized Hamiltonian

The electric-field operator can be expanded near the electromagnetic resonator as [98, 99]

$$\hat{\mathbf{E}}(\mathbf{r}, \omega) = i\sqrt{\frac{\hbar}{2\epsilon_0}} \sum_{\mu} \sqrt{\omega_\mu} \tilde{\mathbf{f}}_\mu(\mathbf{r}) \tilde{\alpha}_\mu + \text{H.a.}. \tag{3.1}$$

$\tilde{\mathbf{f}}_\mu$ is the QNM solution to the Helmholtz equation

$$\nabla \times \nabla \times \tilde{\mathbf{f}}_\mu(\mathbf{r}) - \frac{\tilde{\omega}_\mu^2}{c^2} \epsilon_0 \epsilon_R(\mathbf{r}, \omega_\mu) \tilde{\mathbf{f}}_\mu(\mathbf{r}) = 0 \tag{3.2}$$

derived from the substitution of Eq. (2.1) into Eq. (2.2). $c = 1/\sqrt{\epsilon_0 \mu_0}$ is the speed of light in vacuum. For a single QNM Eq. (3.1) reduces to

$$\hat{\mathbf{E}}(\mathbf{r}) = i\sqrt{\frac{\hbar\omega_C}{2\epsilon_0}}\sqrt{S}\tilde{\mathbf{f}}_C(\mathbf{r})a + \text{H.a.} \tag{3.3}$$

in a symmetrized basis to ensure the bosonic annihilation operator a satisfies canonical commutation relations [98, 99].The S factor is a unitless quantity approximately equal to one for a single QNM ($S \approx 1$) [100, 101]. The subscript C on ω_C and $\tilde{\mathbf{f}}_C$ represents cavity.

The linear exciton-photon interaction associated with transitions between conduction and valence bands for a single QNM is [49, 74]

$$W_1 = \hbar \sum_{\mathbf{k}\alpha} \hat{a}\left(g_{\mathbf{k}\alpha}b_{\mathbf{k}\alpha}^\dagger + g_{\mathbf{k}\alpha}^* b_{-\mathbf{k}\alpha}\right) + \text{H.a.} \tag{3.4}$$

summed over the in-plane wavevector $\mathbf{k}$ and the degenerate high-symmetry points $\alpha \in K, K'$ of the electronic band structure [76]. $\hat{a}$ ($b_{\mathbf{k}\alpha}$) is the bosonic annihilation operator for the QNM (exciton). The exciton-photon interaction strength is given by

$$\hbar g_{\mathbf{k}\alpha} = \frac{|e|\mathbf{P}_{\mathbf{k}\alpha}}{m_0}\sqrt{\frac{\hbar}{\epsilon_0\omega_\mathbf{k}}}\langle v \mid \mathbf{r} = \mathbf{0}\rangle. \tag{3.5}$$

e is the elementary charge and m_0 is the electron mass. The factor

$$\mathbf{P}_{\mathbf{k}\alpha} = \int d^3\mathbf{r}\, e^{i\mathbf{k}\cdot\mathbf{r}} u_{c,\alpha}^*(\mathbf{r})\tilde{\mathbf{f}}_C \cdot \hat{\mathbf{p}} u_{v,\alpha}(\mathbf{r}) \tag{3.6}$$

can be simplified by assuming QNM field profile is constant over the unit cell and the wavevector $\mathbf{k}$ is small compared to the reciprocal lattice vector. Then the integral can be written as the integral over a unit cell and a summation over all unit cells.

$$\mathbf{P}_{\mathbf{k}\alpha} = \sum_j e^{i\mathbf{k}\cdot\mathbf{r}_j}\tilde{\mathbf{f}}_c(\mathbf{r}_j, z_0) \cdot \mathbf{p}_{cv}^\alpha \tag{3.7}$$

where $\mathbf{p}_{cv}^\alpha = \int_{V_{UC}} d^3\mathbf{r}\, u_{c,\alpha}^*(\mathbf{r})\hat{\mathbf{p}} u_{v,\alpha}(\mathbf{r})$ is the interband momentum matrix element. The summation over j can then be rewritten as an integral:

$$\mathbf{P}_{\mathbf{k}\alpha} = \frac{1}{S}\int d^3\mathbf{r}\, e^{i\mathbf{k}\cdot\mathbf{r}_j}\tilde{\mathbf{f}}_c(\mathbf{r}_j, z_0) \cdot \mathbf{p}_{cv}^\alpha. \tag{3.8}$$

Then the position space wavefunction of a 2D exciton $\langle \mathbf{r} \mid v \rangle = \sqrt{\frac{2}{\pi} \frac{2}{a_0}} e^{-2|\mathbf{r}|/a_0}$ [75] contributes a factor of

$$\langle v \mid \mathbf{r} = \mathbf{0} \rangle = \sqrt{\frac{2}{\pi a_B^2}} \tag{3.9}$$

with an effective Bohr radius $a_B = a_0/2$, assuming equal electron and hole effective masses [102]. Substitution of Eq. (3.8) and (3.9) into Eq. (3.5) becomes

$$\hbar g_{\mathbf{k}\alpha} = \frac{|e|}{m_0} \sqrt{\frac{\hbar}{\pi \epsilon_0 \omega a_B^2 S}} \int \mathrm{d}^2 \mathbf{r} e^{i\mathbf{k} \cdot \mathbf{r}} \tilde{\mathbf{f}}_C\left(\mathbf{r}, z_0\right) \cdot \mathbf{p}_{\mathrm{cv}}^\alpha. \tag{3.10}$$

In a frame rotating at the frequency of an external pump laser, utilizing the rotating wave approximation, the linear exciton-photon interaction reduces to

$$\hat{H}_{\mathrm{I}} = \sum_{\alpha \mathbf{k}} \left(\hbar g_{\alpha \mathbf{k}} \hat{a}_{\mathrm{c}} \hat{b}_{\alpha \mathbf{k}}^\dagger + \hbar g_{\alpha \mathbf{k}}^* \hat{a}_{\mathrm{c}}^\dagger \hat{b}_{\alpha \mathbf{k}} \right) \tag{3.11}$$

A reaction coordinate (RC) mapping [103–105] can then be chosen in which the QNM coupled to the bosonic environment of excitons in Eq. (3.11) is mapped to a collective excitonic mode, called the exciton reaction coordinate, with the simplified light-matter interaction Hamiltonian

$$\hat{H}_{\mathrm{I}} = \hbar G_0 \left(\hat{B}_0 \hat{a}^\dagger + \hat{B}_0^\dagger \hat{a} \right). \tag{3.12}$$

The light-matter interaction strength is then

$$G_0 = \sqrt{\sum_{\alpha \mathbf{k}} |g_{\alpha \mathbf{k}}|^2} = \sqrt{\int \mathrm{d}\omega J_{RC}(\omega)} \tag{3.13}$$

characterized by an effective spectral density $J(\omega) = \sum_{\alpha \mathbf{k}} |g_{\alpha \mathbf{k}}|^2 \delta\left(\omega - \omega_{\mathbf{k}}\right)$. By inspection the excitonic mode annihilation operator is

$$\hat{B}_0 = \left[\sum_{\alpha \mathbf{k}} |g_{\alpha \mathbf{k}}|^2 \right]^{-1/2} \sum_{\alpha \mathbf{k}} g_{\alpha \mathbf{k}}^* \hat{b}_{\alpha \mathbf{k}}. \tag{3.14}$$

This can be extended to higher-order exciton modes

$$\hat{B}_i = \sum_{\alpha\mathbf{k}} U_{i\alpha\mathbf{k}}\hat{b}_{\alpha\mathbf{k}} \tag{3.15}$$

where the first row of the transformation matrix U is $U_{0\alpha\mathbf{k}} = g^*_{\alpha\mathbf{k}} \left(\sum_{\alpha\mathbf{k}} |g_{\alpha\mathbf{k}}|^2\right)^{-1/2}$.

Substitution of Eq. (3.10) into Eq. (3.13) results in

$$\hbar G_0 = \sqrt{\frac{\hbar e^2}{\pi\epsilon_0 m_0^2 \omega a_{\mathrm{B}}^2} \frac{1}{S} \left| \sum_\alpha \int \mathrm{d}^2\mathbf{r}\, \tilde{\mathbf{f}}_C\left(\mathbf{r}, z_0\right) \cdot \mathbf{p}_{\mathrm{cv}}^\alpha \right|^2} \tag{3.16}$$

$$\leq \sqrt{\frac{\hbar e^2}{\pi\epsilon_0 m_0^2 \omega a_{\mathrm{B}}^2} \frac{1}{S} \sum_\alpha |\hat{\epsilon} \cdot \mathbf{p}_{\mathrm{cv}}^\alpha|^2 \int \mathrm{d}^2\mathbf{r}\, \left|\tilde{\mathbf{f}}_C\left(\mathbf{r}, z_0\right)\right|} \tag{3.17}$$

To relate the free parameters of Eq. (3.16) to quantities that can be experimentally determined, consider within the semi-classical Lorentz oscillator model the electric susceptibility can be written as [75, 106]

$$\chi(\omega) = \frac{e^2}{\epsilon_0 m_0 V} \sum_j \frac{f_j}{\omega_j^2 - \omega^2 - i\gamma_{j\omega}} \tag{3.18}$$

with an oscillator strength f_j at frequency ω_j with a damping γ_j. The exciton oscillator strength is evaluated in the effective mass approximation as

$$f_{\hat{\epsilon}} = \sum_\alpha \frac{2 |\hat{\epsilon} \cdot \mathbf{p}_{\mathrm{cv}}^\alpha|^2}{m_0 \hbar \omega} \left| \int F(\mathbf{r} = 0, \mathbf{R}) d\mathbf{R} \right|^2 \tag{3.19}$$

For free excitons in two dimensions, the exciton envelope function is $\langle \mathbf{r}, \mathbf{R} \mid v \rangle = S^{-1/2} e^{i\mathbf{k}\cdot\mathbf{R}} \langle \mathbf{r} \mid v \rangle$ where $\langle \mathbf{r} \mid v \rangle$ is as described before Eq. (3.9). For a single excitonic transition the dielectric function of a monolayer TMD , such as $MoSe_2$, can be modeled as a Lorentzian oscillator [107]

$$\epsilon(\omega) = \epsilon_b + \frac{A}{\omega_X^2 - \omega^2 - i\gamma_X\omega}. \tag{3.20}$$

ϵ_b is the background dielectric constant, where $\epsilon_b = 26$ for MoSe$_2$ [108], which results in a perturbative shift of the cavity resonance. And

$$A = \frac{e^2}{\epsilon_0 m_0 V} f_j \tag{3.21}$$

$$= \frac{e^2}{\epsilon_0 m_0 V} \sum_\alpha \frac{2 \left| \hat{\epsilon} \cdot \mathbf{p}_{cv}^\alpha \right|^2}{m_0 \hbar \omega} \left| \int F(\mathbf{r} = 0, \mathbf{R}) d\mathbf{R} \right|^2 \tag{3.22}$$

$$= \frac{e^2}{\epsilon_0 m_0 V} \frac{2 p_{cv}^2}{m_0 \hbar \omega} \frac{2S}{\pi a_B^2} \tag{3.23}$$

$$= \frac{4 e^2 p_{cv}^2}{\pi m_0^2 \epsilon_0 \hbar \omega a_B^2 L_z} \tag{3.24}$$

is an effective oscillator strength having dimensions of a squared frequency, ω_X is the frequency of the excitonic transition, and γ_X is the total exciton loss rate (including both radiative and non-radiative contributions). The assumption going from Eq. (3.22) to Eq. (3.23) is the field is polarized in-plane. The effective oscillator strength can be measured by fitting a transfer matrix model to the differential reflectance, or reflection contrast, of the monolayer TMD illuminated by a broad spectrum light source [107].

With $p_{cv}^2 = \sum_\alpha \left| \hat{\epsilon} \cdot \mathbf{p}_{cv}^\alpha \right|^2$ substitution of Eq. (3.24) into Eq. (3.16) results in a compact expression for the light-matter interaction strength

$$G_0 = \frac{\sqrt{A}}{2} \sqrt{\frac{L_z}{L_{\text{eff}}}}. \tag{3.25}$$

L_z is the effective thickness of the monolayer TMD and L_{eff} is a length scale defined by the competition between minimizing the excitonic envelope function area S and maximizing the total integrated field.

$$\frac{1}{L_{\text{eff}}} = \frac{1}{S} \left(\int d^2\mathbf{r} \left| \tilde{\mathbf{f}}_C (\mathbf{r}, z_0) \right| \right)^2. \tag{3.26}$$

3.1.2   Optimal material coverage

While this formalism can be applied to any extended 2D coherent media in confined cavity geometries, this result is illustrated assuming parameters appropriate for a MoSe$_2$ monolayer deposited on a silicon nitride in-line nanobeam cavity, because such a system can be readily fabricated in practice [97]. In the following, $\hbar^2 A = 0.4$ eV^2 is fixed as a representative value from experimental reflectivity measurements [107] for monolayer MoSe$_2$. Using a finite difference time domain (FDTD) electromagnetic solver (from Lumerical-Ansys), the cavity field profile is calculated (Fig. 3.6b) to be used into Eq. (3.26) with a resonance at $\omega_C/2\pi = 395.777$ THz (wavelength of 757 nm). Taking the effective thickness of the monolayer material to be equal to the measured one, $L_Z \equiv 0.7$ nm, a maximal value for the light-matter interaction is found for a monolayer length of 4.31 µm (Fig. 3.7). This result runs counter to the result associated with the Dicke model, in which a giant oscillator is expected to grow monotonically with the number of oscillators ($g \propto \sqrt{N} g_0$) [109], which in this case correlates to the area of monolayer MoSe$_2$ assuming the excitonic wavefunction is delocalized over the entire field integration region. For a confined field in the cavity we would then expect the light-matter interaction strength g to saturate with the length of the monolayer material and not have a non-monotonic behavior as shown in Fig. 3.7.

Heuristically, this optimal condition between the 2D exciton envelope function and the cavity field profile can be understood in terms of the light-matter interaction by recognizing that the steady state electric field of the nanobeam cavity has an approximately Gaussian envelope along the cavity axis, with a width σ (units of length) modulated by a sinusoidal signal of the photonic lattice periodicity [67] (see, e.g., Fig. 3.6a). Assuming the length of the coherent polarization due to the delocalized excitonic wavefunction is the same as the length of the cavity integration, L_x, substitution of a Gaussian cavity field profile into Eq. 3.26 gives a light-matter interaction strength of the form $g \propto \sqrt{\frac{1}{L_x} \int_{-L_x/2}^{L_x/2} e^{-\frac{1}{2}\left(\frac{x}{\sigma}\right)^2} dx} \propto \sqrt{\frac{\sigma}{L_x} \mathrm{erf}\left(\frac{L_x}{2\sqrt{2}\sigma}\right)}$. The latter function gives a peak in the light-matter interaction around 2.80σ, which roughly corresponds with the 2.44σ that is numerically calculated for the designed in-line nanobeam

cavity. In Fig. 3.7 this heuristic estimate is overlayed on top of the numerical simulation.

3.2   Light-matter interaction strength

A zero-dimensional (0D) PCDR integrated into a waveguide, also known as a nanobeam cavity, was designed (Fig. 3.1a) and fabricated (Fig. 3.1b) in a SiN thin-film on a silicon dioxide substrate with an estimated cavity mode volume $V \sim 2(\lambda/n)^3$, according to the standard cavity QED definition [110]. Finite difference time domain simulations were used to optimize the cavity design [34, 66, 111] with additional Bragg mirrors included to further improve the cavity quality factor. Note that unlike most SiN photonic crystal cavities, this design is an on-substrate cavity that is not suspended. The substrate underneath makes the cavity quality factor lower than what can be achieved in a suspended cavity, but provides the mechanical stability for easy transfer of 2D materials and cleaning of the chip. The bare cavity transmission is interrogated via a confocal microscope using input and output grating couplers with a ≈ 5 µm $\times$ 5 µm collection area and a 5-10% collection efficiency at the cavity resonance frequency. A monolayer MoSe$_2$ flake was then transferred onto the nanobeam via the method described in chapter 2 to eliminate any bulk materials or tape residues on the grating or the waveguide [112] (Figs. 3.1c, d). This coupled MoSe$_2$-nanobeam device was placed in a cryostat where the temperature was swept between 80 K and 200 K.

3.2.1   Device characterization

Monolayer MoSe$_2$ exhibits poor optical contrast on the SiN substrate (Fig. 3.1b). Hence, the presence of the monolayer on the nanocavity is confirmed by measuring the photoluminescence (PL). A strong excitonic peak was observed in the PL spectrum (at 80K), as shown in Fig. 3.2a. When the PL is collected from a grating coupler (versus from the full field of view of the confocal microscope), a cavity peak is clearly evidenced in the spectrum (Fig. 3.2b). The background PL is also observed simultaneously due to imperfect spatial filtering in the confocal microscope. Due to a limited field of view in the microscopy setup (≈ 50 µm $\times$ 50 µm), the cavity with transferred monolayer must be in close proximity to the output grating,
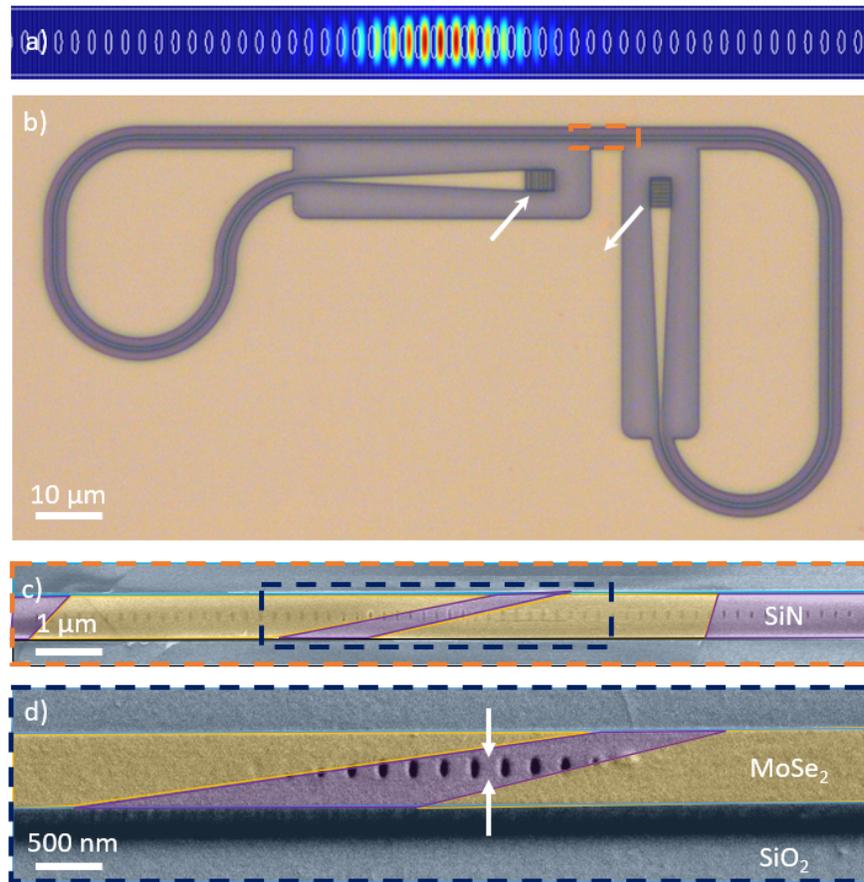
Figure 3.1: **Monolayer MoSe$_2$ integrated onto a photonic crystal defect resonator.**
a) Electric field intensity simulated at the center of the SiN nanobeam cavity by 3D-FDTD
at the cavity mode resonance frequency, showing wavelength scale field confinement. The
maximum field intensity is seen in the center of the nanobeam. b) Optical image of the
monolayer MoSe$_2$ (not visible) integrated onto the nanobeam (orange box) with the grating
couplers for transmission measurements (green - excitation, red - collection). Scale bar is
10 µm. c) False color SEM image of the monolayer MoSe$_2$ integrated onto the nanobeam.
(MoSe$_2$ - gold, SiN - purple, SiO$_2$ - teal). Scale bar is 1 µm. d) False color SEM image of
the monolayer MoSe$_2$ integrated onto the nanobeam with deposited gold to prevent charging.
The obstruction of the nanobeam holes is made explicit. Red arrows indicate the cavity
center. Scale bar is 500 nm.

making it difficult to spatially filter radiation scattered from the sample.

The nanobeam cavity was characterized via resonant transmission. A broadband super-continuum laser was directed into one of the gratings and the transmitted radiation is collected from the other grating. Prior to monolayer material integration, the cavity resonance was measured at 300 K to be $\hbar\omega_C = 1595$ meV with a linewidth $\hbar\kappa_0 = 3.8$ meV, corresponding to a bare quality factor $Q_0 = 420$ (Fig. 3.2c). After transfer of the monolayer $MoSe_2$ the bare cavity resonance was measured at 80 K to be $\hbar\omega_C = 1590$ meV with a broadened linewidth $\hbar\kappa = 10.7$ meV, corresponding to a loaded quality factor $Q = 149$ (Fig. 3.2d). The reduction in quality factor is attributed to the optical absorption of the monolayer $MoSe_2$. The shift in the resonance energy comes from the perturbation of the cavity due to the background dielectric constant of the monolayer material and a dispersive shift of the cavity. The dispersive shift is investigated via temperature tuning of the excitonic transition. It is emphasized that as the linewidth of the monolayer $MoSe_2$ is the dominant source of decay in the coupled system, the observed quality factor of the cavity, albeit low, is sufficient to probe the physical effect of coherent coupling.

3.2.2   Temperature dependence

The neutral exciton PL and cavity transmission were then concurrently measured as the temperature was swept from 80K to 200K. At low temperature, the cavity mode is detuned on the blue side of the excitonic resonance. As the temperature is increased the exciton resonance redshifts, so the detuning between the exciton and cavity resonances decrease. The excitonic PL spectra at different temperatures are fit with a Voigt function [113] to extract the peak energy (ω_X) and linewidth (γ) where the source of inhomogeneous broadening ($\Delta = 4.42 \pm 2.27$ meV) is assumed to be independent of temperature [114].

The temperature dependence of the neutral exciton peak energy is fit to the standard
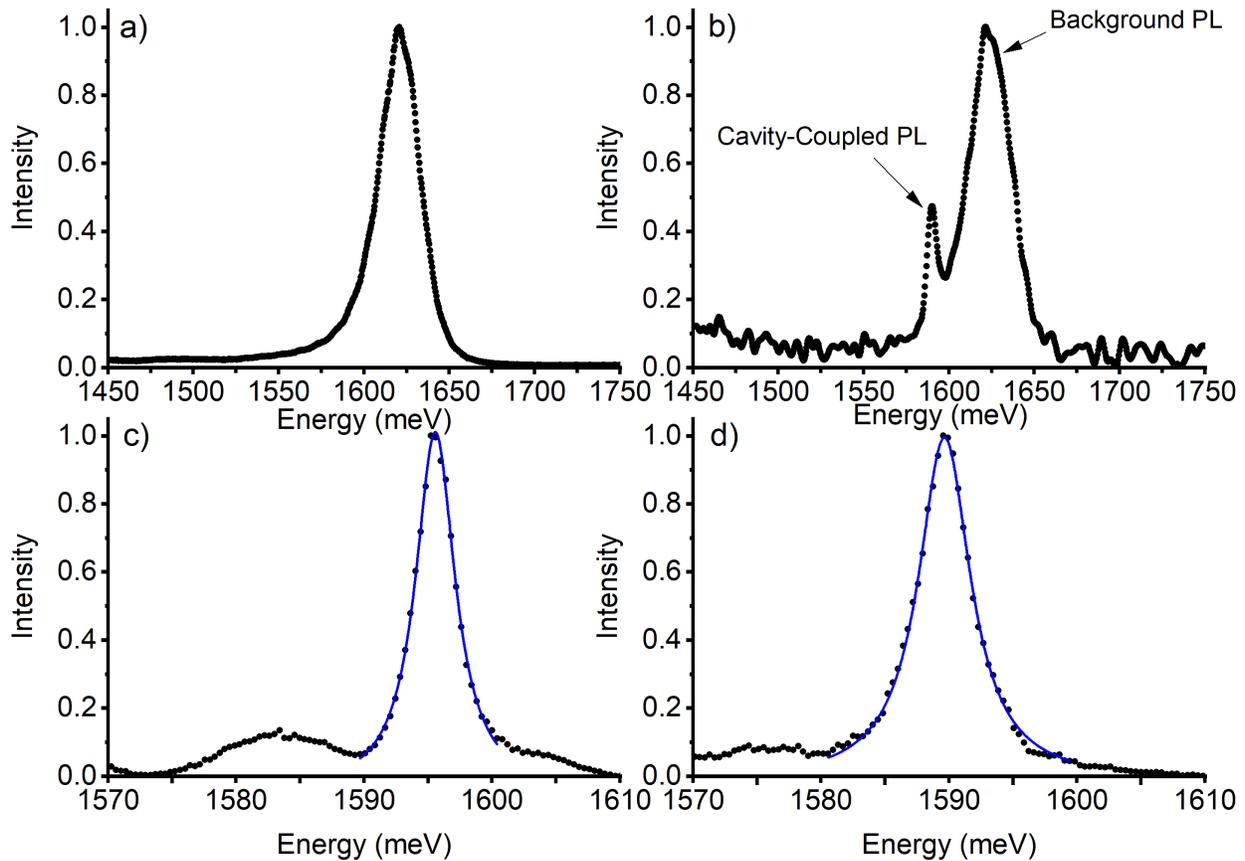
Figure 3.2: **Spectra for the monolayer MoSe$_2$ integrated onto a photonic crystal defect resonator.** a) Photoluminescence of monolayer MoSe$_2$ at 80 K. b) Cavity-coupled photoluminescence of monolayer MoSe$_2$ at 80 K. Primary peak is background photoluminescence. Secondary peak is collected from the grating coupler confirming cavity coupling. c) Bare transmission spectrum of the nanobeam cavity at 300 K. The blue curve is a Lorentzian fit to the cavity resonance. d) Transmission spectrum of the nanobeam cavity with an integrated flake of monolayer MoSe$_2$ at 80 K. The blue curve is a Lorentzian fit to the cavity resonance.

equation for the semiconductor bandgap [115] (Fig. 3.3a):

$$E_X(T) = E_X(0) - S\langle \hbar\omega \rangle [\coth{[\langle \hbar\omega \rangle/(2k_BT)]} - 1]$$
$$\approx E_X'(0) - 2Sk_BT \tag{3.27}$$

where $E_X(0)$ is the zero Kelvin neutral exciton energy, S is a dimensionless coupling constant, and $\langle \hbar\omega \rangle$ is the average phonon energy. This relation corresponds to the neutral exciton energy assuming the exciton binding energy is not strongly temperature dependent. In this experiment, the temperature range explored remains in the linear regime at high temperatures. A fit to the extracted energy of the neutral exciton provides a linearized zero Kelvin neutral exciton energy of $E_X'(0) \equiv E_X(0) + S\langle \hbar\omega \rangle = 1637$ meV and a dimensionless coupling constant $S = 1.21$. These values are comparable to previous reports in the literature [116].

Similarly, the temperature dependence of the neutral exciton linewidth is fit to the Rudin equation [117] (Fig. 3.3b):

$$\gamma_X(T) = \gamma_0 + c_1 T + \frac{c_2}{e^{\Omega/k_BT} - 1}$$
$$\approx \gamma_0' + Rk_BT \tag{3.28}$$

where γ_0 is the intrinsic homogeneous linewidth, c_1 includes exciton interactions with acoustic phonons, c_2 includes exciton interactions with longitudinal-optical phonons, and Ω is the average phonon energy. In the linearized equation $\gamma_0' = \gamma_0 - \frac{c_2}{2}$ and $R = \frac{c_2}{\Omega}$ where it is assumed $c_1 << c_2$. A fit to the extracted neutral exciton linewidth provides for an intrinsic linewidth of $\hbar\gamma_0' = 5.77$ meV and a dimensionless coupling constant $R = 0.69$. These values are also comparable to previous reports in the literature [114].

It is worth noting the bare nanobeam cavity resonance wavelength does not significantly shift with temperature, which is primarily due to the low thermo-optic coefficient of SiN (Fig. 3.4a). The temperature-independent cavity resonance shift of ~ 5 meV (comparing Fig. 3.2a and Fig. 3.2b) is consistent with the cavity perturbation theory [118, 119], where the monolayer material is modelled as a $d = 0.7$ nm thick homogeneous dielectric with an $n_B = \sqrt{\epsilon_B}$ index of refraction where $\epsilon_B = 26$ is the background dielectric constant for

40
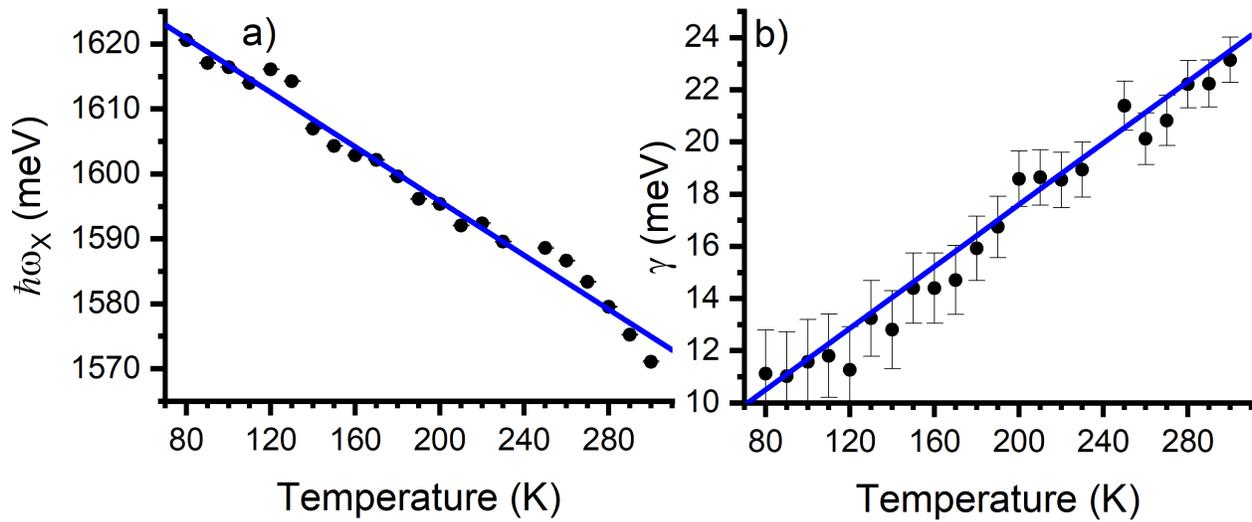
Figure 3.3: **Temperature dependence of the neutral exciton resonance in** MoSe$_2$. a) Temperature dependence of the neutral exciton resonance. The black dots are the neutral exciton energy observed in the photoluminescence spectrum fit to a Voigt function. The blue line is a fit to Eq. 3.27. b) Temperature dependence of the neutral exciton linewidth. The black dots are the neutral exciton linewidth observed in the photoluminescence spectrum fit to a Voigt function. The blue line is a fit to Eq. 3.28.

monolayer MoSe$_2$ [107]. In the TMD-coupled nanobeam resonator a shift in the cavity resonance is clearly observed as the exciton-cavity detuning decreases (Fig. 3.4b). We attribute this shift to the dispersive coupling of the 2D excitons in the monolayer MoSe$_2$ to the 0D nanobeam cavity mode, which is hereby established via a simple coupled oscillator model. We note that the cavity transmission is significantly suppressed as the exciton is brought into resonance with the cavity (Fig. 3.9a). Additionally, the exciton linewidth increases at higher temperatures precluding the observation of avoided crossing, a hallmark of strong coupling, in the reported system. This is a critical limitation of the temperature tuning. Other tuning mechanisms, such as gas tuning [120], have been considered but the effect of deposited xenon and nitrogen gas on 2D materials leads to inconclusive results.

It is worth noting the bare nanobeam cavity resonance wavelength does not significantly shift with temperature, which is primarily due to the low thermo-optic coefficient of SiN (Fig. 3.4a). However, in the TMD-coupled nanobeam resonator a shift in the cavity resonance was clearly observed as the exciton-cavity detuning decreases (Fig. 3.4b). We attribute this shift to the dispersive coupling of the 2D excitons in the monolayer MoSe$_2$ to the zero-dimensional (0D) nanobeam cavity mode, which is hereby established via a simple coupled oscillator model.

3.2.3 Coupled oscillator model

A homogeneous distribution of TMD excitons and a single 0D cavity mode can be phenomenologically modeled with a Hamiltonian describing two coupled oscillators, wherein the exciton and cavity degrees of freedom coherently interact via an exciton-cavity coupling rate, g. The bare oscillator resonance frequencies are measured with respect to a rotating frame at the resonant driving frequency, ω_L. The Hamiltonian is

$$H_{XC} = \hbar\Delta_{CL}\hat{a}^\dagger\hat{a} + \hbar\Delta_{XL}\hat{b}^\dagger\hat{b} + \hbar g(\hat{b}^\dagger\hat{a} + \hat{b}\hat{a}^\dagger)\,, \tag{3.29}$$

where $\Delta_{XL} = \omega_X - \omega_L$ and $\Delta_{CL} = \omega_C - \omega_L$ are the detunings of the exciton and cavity modes from the laser frequency, respectively; $\hat{b}$ ($\hat{a}$) is the annihilation operator for the exciton
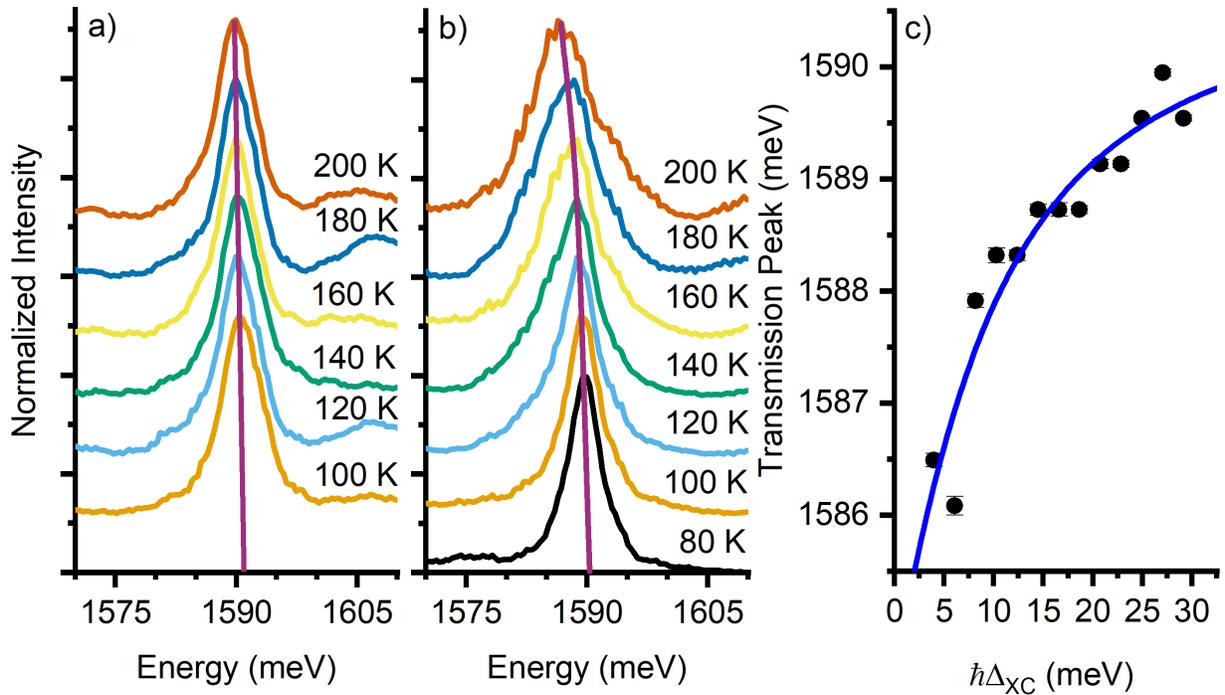
Figure 3.4: **Temperature dependence of the monolayer MoSe$_2$ integrated onto a photonic crystal defect resonator.** a) Representative transmission spectra of the nanobeam cavity without an integrated flake of monolayer MoSe$_2$ at 100 K to 200 K in 20 K increments. b) Representative transmission spectra of the nanobeam cavity with an integrated flake of monolayer MoSe$_2$ at 80 K to 200 K in 20 K increments. b) Dispersive shift of the cavity resonance in transmission.

43

(cavity) mode. In the weak excitation regime, exciton saturation and any exciton-exciton interaction can be neglected. Hence, both exciton and cavity operators can be treated as bosonic modes. Including losses, the model can be completed by defining the Liouvillian operator for the density matrix, $\mathcal{L}(\rho) = \frac{1}{i\hbar}[H, \rho] + \hbar\kappa\mathcal{L}_{\hat{a}}(\rho) + \hbar\gamma\mathcal{L}_{\hat{b}}(\rho)$, which accounts for the finite cavity and exciton linewidths. The Lindblad operators are $\mathcal{L}_{\xi}(\rho) = \xi\rho\xi^{\dagger} - \frac{1}{2}\xi^{\dagger}\xi\rho - \frac{1}{2}\rho\xi^{\dagger}\xi$, in which $\xi = \hat{b}, \hat{a}$.

By diagonalizing the Liouvillian within the single excitation subspace, the following eigenenergies can be obtained [48, 110, 121, 122]

$$\omega_{\pm} = \omega_C + \frac{\Delta_{XC}}{2} - i\frac{\kappa + \gamma}{2} \pm \sqrt{g^2 + \frac{1}{4}\left[\Delta_{XC} + i(\kappa - \gamma)\right]^2}, \tag{3.30}$$

in which $\Delta_{XC} = \omega_X - \omega_C$ is the exciton-cavity detuning. The experimental data is fit with Eq. 3.30 for an exciton-cavity coupling energy $\hbar g = 6.47 \pm 0.39$ meV (Fig. 3.4b). Near zero exciton-cavity detuning transmission spectra were not included due to the reduced transmission efficiency inherent to the in-line cavity design [96]. It should be noted the exciton PL peak energy is used as a proxy for the absorption resonance, since MoSe$_2$ is known to have a small Stokes shift [29] which in this case is approximately 1 meV. The extracted light-matter interaction is similar to related nanophotonic structures, although it is expected to be larger with an optimal coverage of the cavity mode [95, 97].

Figure 3.5 is an alternative plot demonstrating the subtle dispersive shift of the cavity as the exciton-cavity detuning is decreased. The blue diagonal line tracks the peak of the neutral exciton photoluminescence in monolayer MoSe$_2$. The orange vertical line tracks what would be the temperature-independent cavity resonant frequency due to the low thermo-optic coefficient of silicon nitride. The curved purple line tracks the peak of the cavity transmission spectrum showing the avoided crossing of the cavity resonant frequency and the excitonic transition. The photoluminescence is the total emission of the monolayer flake. Should it be possible to observe the photoluminescent emission solely at the center of the cavity mode we would expect to see level repulsion of the exciton resonant frequency as well.

The light-matter coupling energy was theoretically estimated to be $\hbar g = 4.2$ meV from Eq
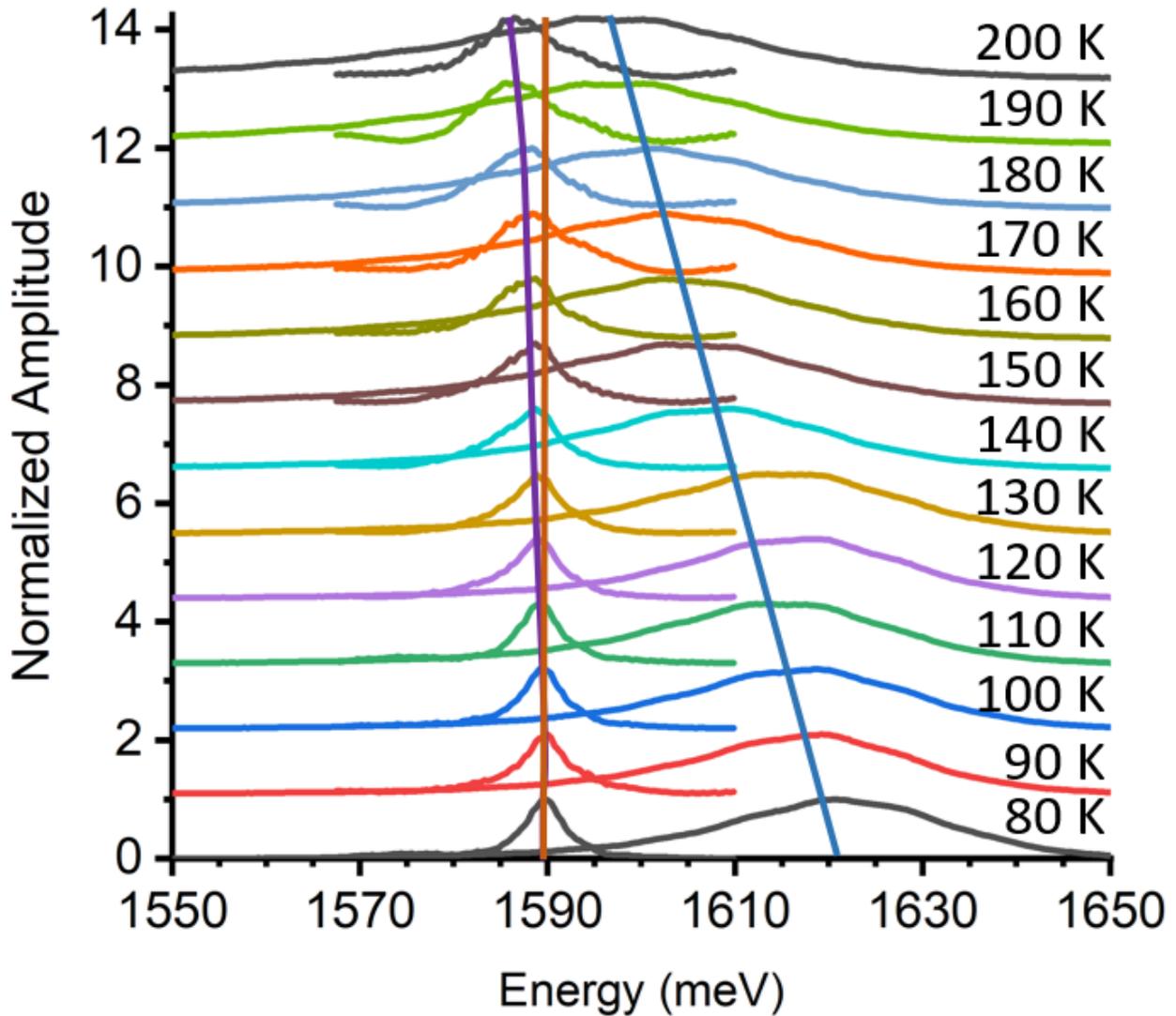
Figure 3.5: Overlayed plots of the cavity transmission (left peak) and $MoSe_2$ photoluminescence (right peak). The center frequency of the neutral exciton exhibited in the photoluminescence is plotted in Fig. 3.3a. The center frequency of the cavity resonance is plotted in Fig. 3.4c with respect to the exciton detuning from the bare cavity resonant frequency.

(3.25). Qualitative agreement with the value extracted from the dispersive shift is attained when assuming a 2D flake coverage of the nanocavity compatible with the one inferred from the sample SEM (Fig. 3.1d). A maximal simulated exciton-cavity coupling energy $\hbar g = 5.1$ meV is obtained for this cavity design when the 2D flake extension matches the spatial envelope of the cavity mode electric field. Note that the experimentally measured value of $\hbar g$ is slightly larger than the theoretical prediction. This is attributed to reduced confinement of the electromagnetic field in the cavity due to fabrication imperfections (such as sidewall roughness), and thus a stronger field on the cavity surface than the theoretical design.

3.3 Input-output relations

Now explicitly consider the experimental scheme allowing to probe the polariton excitations in the material system. Often, such light-matter coupled systems are measured via incoherent photoluminescence; however, coherent driving in a transmission configuration is necessary in view of practical development of quantum technology applications [123]. For the on-chip microresonator, the exciton-polariton modes can generally be probed using a two-sided cavity [68] (Fig. 3.6a). An input grating is used to send light to the coupled system and the transmitted light is collected via an output grating.

The input-output relation for the exciton-resonator system in the linear regime is similar to that found for the side-coupled resonator with two degenerate modes owing to the bosonic nature of the excitonic transition. The Hamiltonian (compare to Eq. (3.29)) describing the in-line, single-mode electromagnetic resonator and the localized excitonic mode as two coupled oscillators is

$$\hat{H}_{XC} = \hbar \tilde{\Delta}_{CL} \hat{a}^\dagger \hat{a} + \hbar \tilde{\Delta}_{XL} \hat{b}^\dagger \hat{b} + \hbar g (\hat{b}^\dagger \hat{a} + \hat{b} \hat{a}^\dagger) \tag{3.31}$$

with a light-matter interaction strength g. $\tilde{\Delta}_{CL} = (\omega_C - \omega_L) - i\kappa$ and $\tilde{\Delta}_{XL} = (\omega_X - \omega_L) - i\gamma_X$ are the detunings and intrinsic radiative loss of the resonator mode (ω_C, κ) and excitonic transition (ω_X, γ_X) from the laser frequency (ω_L), respectively. $\hat{a}$ $(\hat{b})$ is the bosonic annihilation operator for the resonator (excitonic) mode.

3.3.1   In-line resonator

For an in-line resonator, the quantum Langevin equations describing the internal resonator and excitonic modes with a single external driving field are

$$\frac{d\hat{a}}{dt} = -\frac{i}{\hbar}[\hat{a}, \hat{H}_{XC}] - \frac{\gamma_1}{2}\hat{a} - \frac{\gamma_2}{2}\hat{a} + \sqrt{\gamma_1}\hat{a}_{in} \tag{3.32}$$

$$\frac{d\hat{b}}{dt} = -\frac{i}{\hbar}[\hat{b}, \hat{H}_{XC}]. \tag{3.33}$$

Eq. (3.32) is idential to that of Eq. (2.7) except the modified Hamiltonian. The transmitted field $\hat{a}_{out}$ is coupled to the resonator via γ_2, as described by the equation

$$\hat{a}_{out} = \sqrt{\gamma_2}\hat{a}. \tag{3.34}$$

Inserting Eq. (3.31) into Eqs. (3.32) and (3.33), and then computing the commutator gives

$$\frac{d\hat{a}}{dt} = -i\tilde{\omega}_C\hat{a} - ig\hat{b} - \frac{\gamma_1}{2}\hat{a} - \frac{\gamma_2}{2}\hat{a} + \sqrt{\gamma_1}\hat{a}_{in} \tag{3.35}$$

$$\frac{d\hat{b}}{dt} = -i\tilde{\omega}_X\hat{b} - ig\hat{a}. \tag{3.36}$$

Following identical steps which concluded with Eq. (2.15), the transmission efficiency is

$$T(\omega) = \left|\frac{\tilde{a}_{out}}{\tilde{a}_{in}}\right|^2 = \left|\frac{\sqrt{\gamma_1\gamma_2}}{-i(\omega - \tilde{\omega}_C) + \frac{1}{2}(\gamma_1 + \gamma_2) + \frac{g^2}{-i(\omega - \tilde{\omega}_X)}}\right|^2. \tag{3.37}$$

Collecting real and imaginary components of the expression, this can be rewritten as

$$T(\omega) = \left|\frac{\sqrt{\gamma_1\gamma_2}}{-i\left[(\omega - \omega_C) - \frac{(\omega - \omega_X)g^2}{(\omega - \omega_X)^2 + \gamma_X^2}\right] + \left[\frac{1}{2}(\gamma_1 + \gamma_1) + \kappa + \frac{\gamma_X g^2}{(\omega - \omega_X)^2 + \gamma_X^2}\right]}\right|^2 \tag{3.38}$$

The transmitted spectrum is then

$$T(\omega) = \frac{\gamma_1 \gamma_2}{\left[\omega - \omega_C - \frac{(\omega - \omega_X)g^2}{(\omega - \omega_X)^2 + \gamma_X^2}\right]^2 + \left[\kappa + \frac{1}{2}(\gamma_1 + \gamma_2) + \frac{\gamma_X g^2}{(\omega - \omega_X)^2 + \gamma_X^2}\right]^2}. \tag{3.39}$$

For an in-line resonator symmetrically coupled to the waveguide ($\gamma = \gamma_1 = \gamma_2$), the transmitted spectrum of the exciton-resonator system is

$$T(\omega) = \frac{\gamma^2}{\left[\omega - \omega_C - \frac{(\omega - \omega_X)g^2}{(\omega - \omega_X)^2 + \gamma_X^2}\right]^2 + \left[\kappa + \gamma + \frac{\gamma_X g^2}{(\omega - \omega_X)^2 + \gamma_X^2}\right]^2}. \tag{3.40}$$

The minima for Eq. (3.40) in the strong coupling regime at zero exciton-cavity detuning (setting $\omega = \omega_C = \omega_X$) gives a transmission of

$$T = \left(\frac{\gamma}{\kappa + \gamma}\right)^2 \frac{1}{(1 + C)^2} \tag{3.41}$$

where the cooperativity is defined as $C \equiv \frac{g^2}{\gamma_X(\kappa + \gamma)}$, which effectively quantifies the visibility of the polariton modes. In the absence of an optical transition this reduces to the T_{max} discussed in section 2.1.2.

At zero exciton-cavity detuning ($\omega_C = \omega_X$) by setting the derivative of Eq. (3.40) equal to zero ($\frac{dT}{d\omega} = 0$) there exists a maxima at $\omega_\pm = \omega_C \pm \sqrt{C'g^2 - \gamma_X^2}$ associated with normal mode splitting in the strong coupling regime. Substituting $\omega_\pm$ into Eq. (3.40), the peaks have a transmission efficiency of

$$T(\omega_\pm) = \frac{\gamma^2 C'}{g^2 (C' - 1)^2 + [(\kappa + \gamma)^2 - \gamma_X^2] C' + 2\gamma_X [(\kappa + \gamma) + \gamma_X]}. \tag{3.42}$$

where a new constant is defined $C' = \sqrt{1 + \frac{2}{C}[1 + \gamma_X/(\kappa + \gamma)]}$.

The intrinsic cavity loss and cavity-waveguide coupling can be inferred from the FDTD simulations. The designed in-line nanobeam cavity has a loaded quality factor of $Q_{loaded} = 11924$ and an intrinsic quality factor of $Q_{intrinsic} = 25480$. The intrinsic quality factor of the cavity is found by increasing the number of Bragg mirror holes until the waveguide is no longer coupled to the cavity and the simulated quality factor approaches an asymptotic
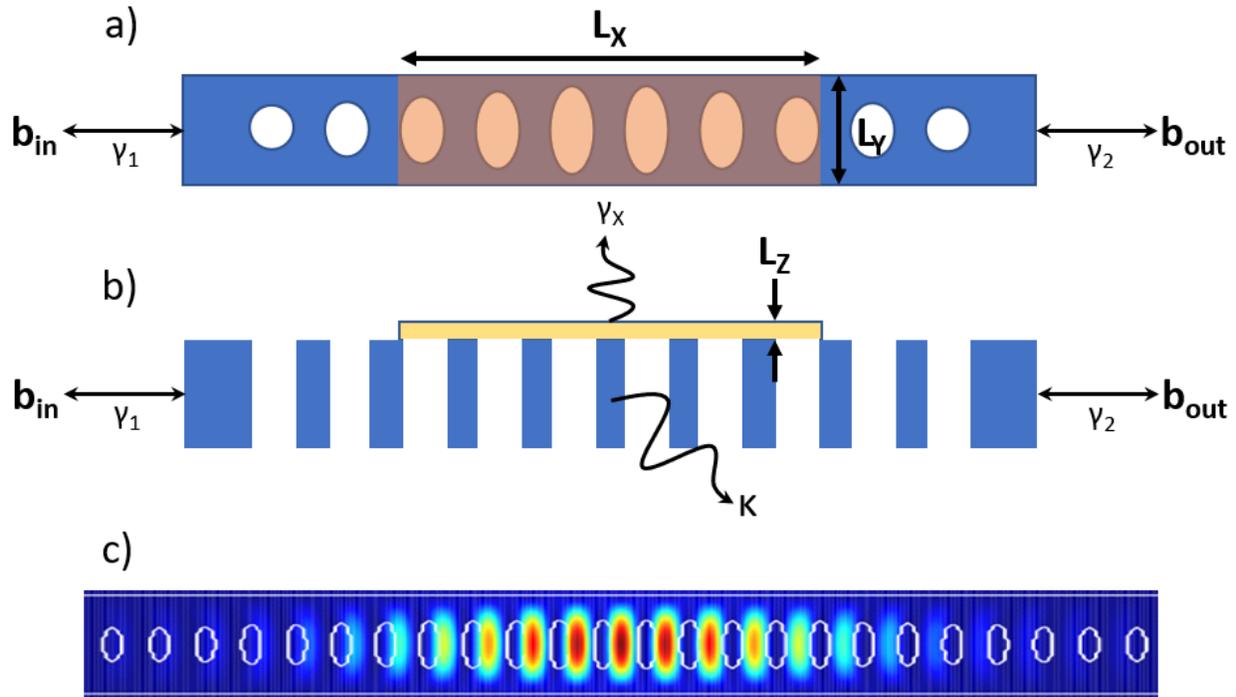
Figure 3.6: **Schematic of the input-output characteristics of a two-sided cavity.** a) Top-view pictorial representation of a photonic crystal defect cavity embedded in-line to a waveguide, coupled to a quantum well supporting a two-dimensional excitonic transition. Blue is the confining dielectric and orange is the quantum well. $\gamma_{1,2}$ are the waveguide-coupled losses. L_X is the length of the integrated quantum well. L_Y is the width of the integrated quantum well. b) Side-view of the waveguide. κ and γ_X are the intrinsic losses of the cavity and exciton, respectively. L_Z is the effective height of the integrated quantum well. b) Electric field intensity simulated at the center of a silicon nitride nanobeam cavity by a finite-difference time-domain electromagnetic solver at the cavity mode resonant frequency, showing wavelength scale field confinement. The maximum field intensity is seen in the center of the nanobeam.
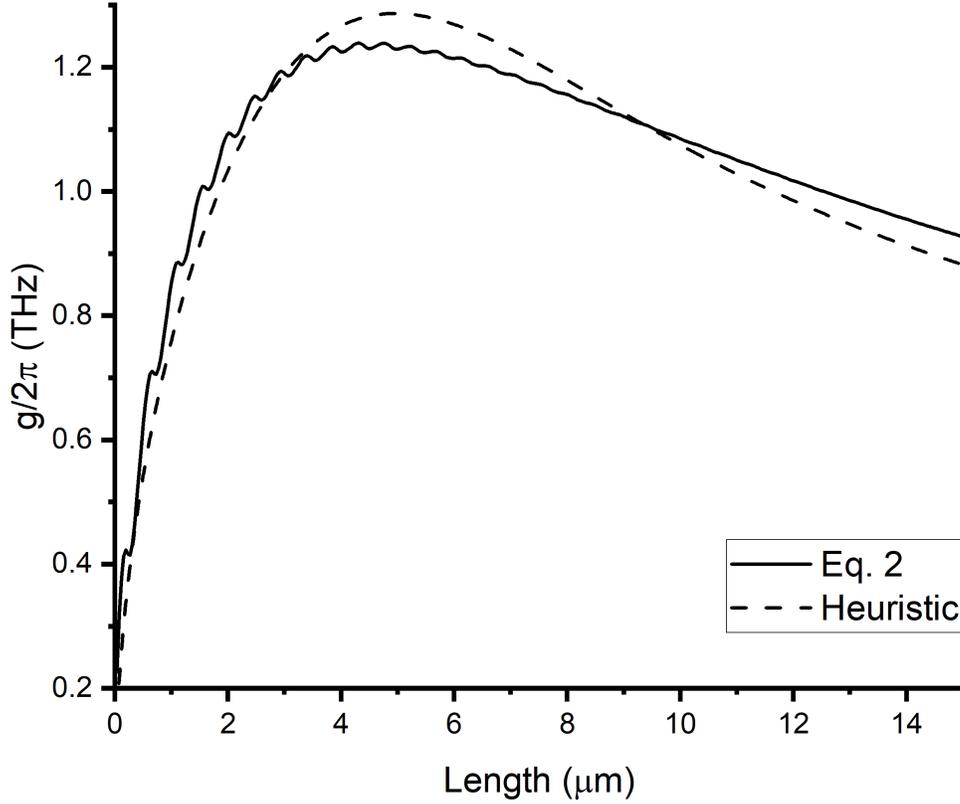
Figure 3.7: **Optimal condition for the light-matter interaction strength.** Light-matter interaction strength for different lengths L_X of the integrated quantum well with L_Y fixed to the width of the waveguide. The oscillations seen in the light-matter interaction originate from the periodic variation of the electric field commensurate with the lattice spacing of the nanobeam air holes. $g/2\pi = 1.2389$ THz is the maximum value for this cavity design and oscillator strength. The dotted line is a fit to the heuristic equation in the text elucidating the peak in the light-matter interaction for a cavity confinement length of $\sigma = 1.77$ µm.

value. Note that for this particular cavity, the design is chosen for an on-substrate, silicon nitride, in-line, nanobeam cavity due to its mechanical stability [34], hence the reduced quality factor compared to a suspended nanobeam cavity. The decay rate of the cavity field is $\kappa = \frac{1}{2}\frac{\omega_C}{Q_{intrinsic}} = 2\pi \times 7.77$ GHz. Similarly, the decay rate of the loaded cavity field is $\kappa + \gamma = \frac{1}{2}\frac{\omega_C}{Q_{loaded}} = 2\pi \times 16.6$ GHz, which gives a waveguide-coupled field decay rate $\gamma = 2\pi \times 8.83$ GHz. This results in an estimated maximum transmission efficiency of $T_{max} = \left(\frac{\gamma}{\kappa+\gamma}\right)^2 = 0.28$ [70]. From the measured temperature dependence of the excitonic transition $\gamma_X(4.2\text{K}) = 2\pi \times 566$ GHz is used as a representative value for the excitonic linewidth in the strong coupling regime.

The transmission spectrum of the coupled exciton-cavity system is calculated using these estimated values of the system parameters (Fig. 3.8a). At large exciton-cavity detuning the transmission efficiency approaches the bare cavity value T_{max}. At smaller detunings, the dispersive cavity shift is noticeable with broadening of the transmission peak. Near zero detuning, however, the intensity of the transmission peak in the strong coupling regime is several orders of magnitude smaller than the bare cavity transmission (Fig. 3.8b). Substituting the parameters, for example, from Fig. 3.8 into Eq. 3.42 the maximum transmission efficiency with the integrated 2D exciton relative to the bare cavity transmission maximum is only 0.098%. Thus a major drawback of an in-line symmetric two-sided cavity is the drastic suppression of transmission near zero exciton-cavity detuning. Note that, suppression of the cavity transmission was observed in experiment as the exciton is brought into resonance with the cavity (Fig. 3.9).

3.3.2   Side-coupled resonator

The drastic reduction in the transmission efficiency of an in-line cavity primarily comes from the large excitonic loss rate γ_X. To ensure an appreciable transmission efficiency, the waveguide-cavity coupling rate (γ) can be increased. But this will reduce the quality factor of the cavity and reaching the strong coupling regime may not be possible. The difficulty of demonstrating high transmission efficiency of the cavity mode near zero exciton-cavity
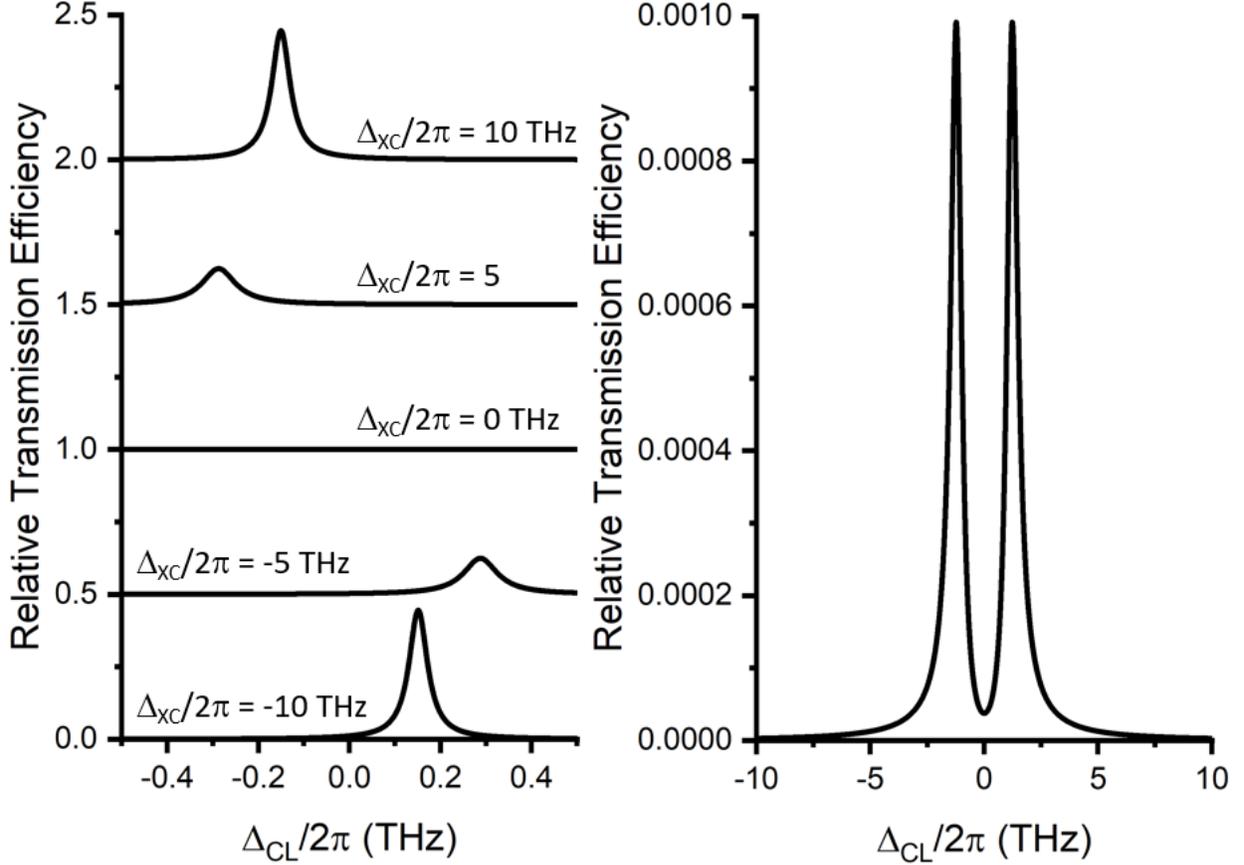
Figure 3.8: **Transmission efficiency of a two-sided cavity with an integrated excitonic transition.** a) Transmission spectrum relative to T_{max} ($T_{relative} = T(\omega)/T_{max}$) at different exciton-cavity detunings Δ_{XC}. $\Delta_{CL} = \omega_C - \omega_L$ is the laser detuning from the bare cavity resonance. For clarity, the transmission spectrum are offset by 0.5 from the lower to upper plots. b) Transmission spectrum relative to T_{max} at zero exciton-cavity detuning. The solid line in part (b) is the magnified solid line of part (a). Note the different x-axis range. Parameters: $\kappa/2\pi = 7.77$ GHz, $\gamma/2\pi = 8.83$ GHz, $\gamma_X/2\pi = 566$ GHz, $g/2\pi = 1.2389$ THz.
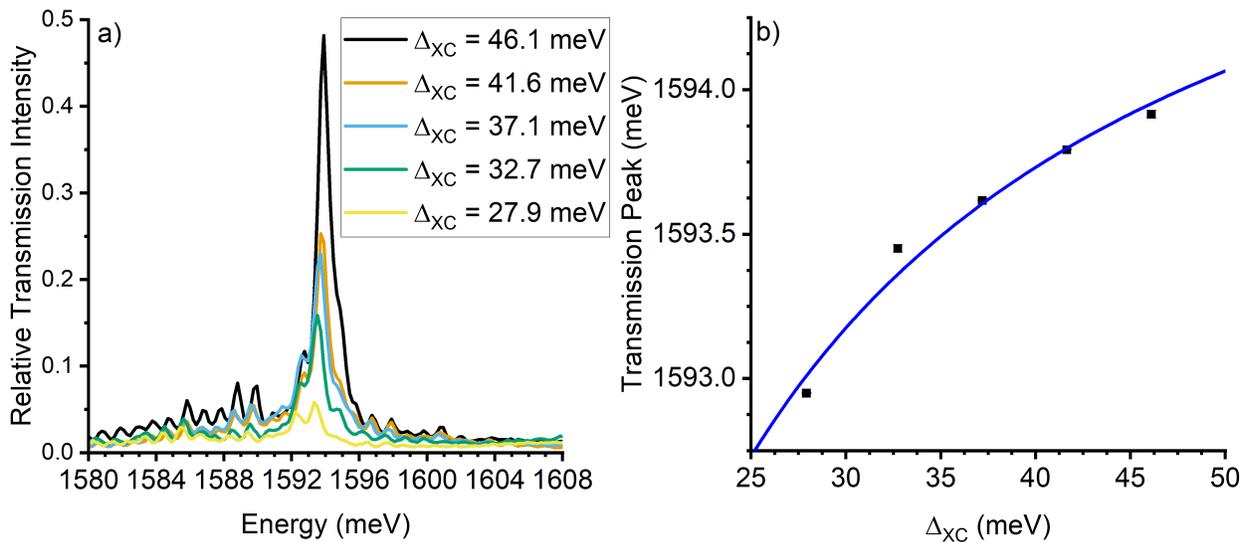
Figure 3.9: **Cavity transmission suppression at small exciton-cavity detunings.** On a second device: a) Transmission spectra at different exciton-cavity detunings. Note a factor of five reduction in transmission intensity even at large detunings which precludes on-resonance transmission measurements, hence the dispersive regime. b) Dispersive shift of the cavity resonance in transmission for a radiation-matter coupling of $\hbar g = 8.17 \pm 0.36$ meV commensurate with that found in the main device with a different areal coverage.

detuning stems from the mismatch between the loss of the hybridized polariton mode and waveguide-coupled loss [124, 125]. This effect is similar to the condition of reaching critical coupling in a waveguide-coupled microring resonator [65]. One way to circumvent this loss in transmission will be to employ a side-coupled waveguide-cavity system [126]. By engineering the side-coupled, waveguide-cavity coupling rate (γ_{SC}) the radiative loss of the polariton can be kept relatively low while still maintaining sufficient waveguide-coupling to observe polariton modes in transmission.

In a side-coupled nanobeam cavity, by modifying the width and the gap of the coupled waveguide to the nanobeam cavity the waveguide-coupled loss can be engineered. Such side-coupled geometry partially decouples the intrinsic cavity quality factor and field profile from the transmission properties of the cavity. We analyze the performance of such a side-coupled cavity and found that significant transmission contrast can be achieved in the strong coupling regime (Fig. 3.10a). Reaching critical coupling in the side-coupled cavity design requires the waveguide-cavity coupling rate to be the same as the polariton loss, which is necessarily no longer in the strong coupling regime. However, in the under-coupled regime, by carefully choosing the waveguide-cavity coupling rate we can achieve a measurable transmission contrast, as we verified numerically (Fig. 3.4b). The side-coupled, waveguide-cavity coupling rate (γ_{SC}) essentially provides an additional degree of freedom for cavity design that is absent in in-line cavities.

For a single-mode, side-coupled resonator the quantum Langevin equations describing the internal resonator and excitonic modes with a single external driving field are

$$\frac{d\hat{a}}{dt} = -\frac{i}{\hbar}[\hat{a}, \hat{H}_{XC}] - i\sqrt{\gamma_{SC}}\hat{a}_{in} \tag{3.43}$$

$$\frac{d\hat{b}}{dt} = -\frac{i}{\hbar}[\hat{b}, \hat{H}_{XC}]. \tag{3.44}$$

The transmitted field $\hat{a}_{out}$ is coupled to the resonator via γ_{SC}, as described by the equation

$$\hat{a}_{out} = \hat{a}_{in} - i\sqrt{\gamma_{SC}}a \tag{3.45}$$
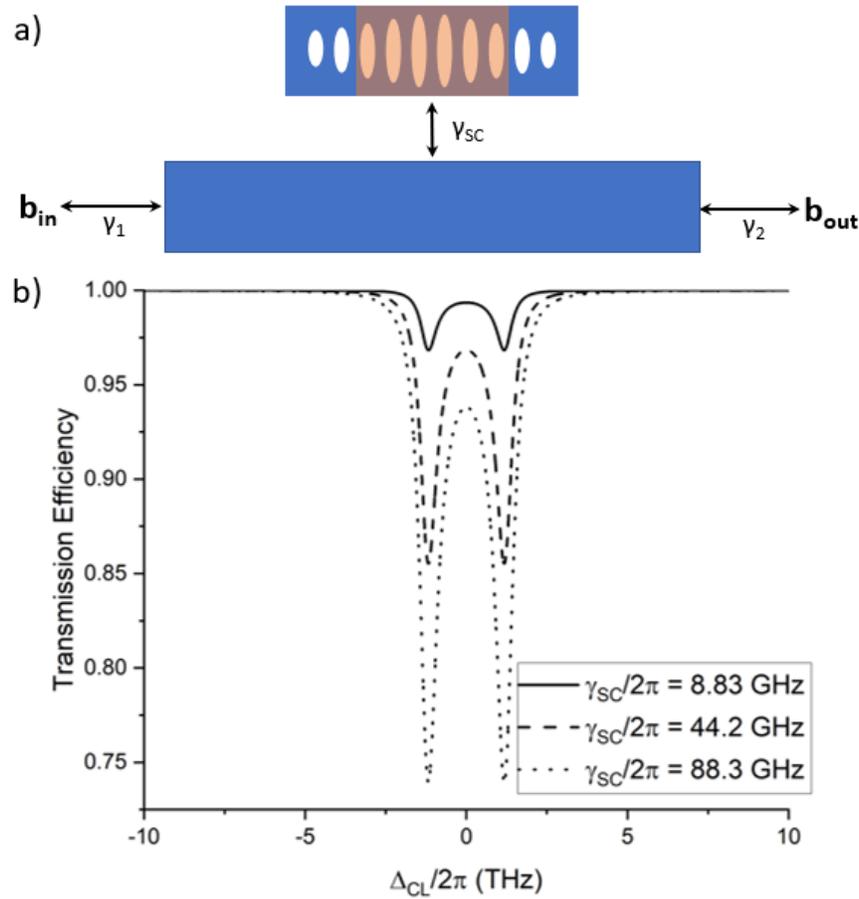
Figure 3.10: **Schematic of the input-output characteristics and transmission effi-ciency of a side-coupled cavity with an integrated excitonic transition.** a) Top-view pictorial representation of a photonic crystal defect cavity side-coupled to a waveguide, coupled to a quantum well supporting a two-dimensional excitonic transition. Blue is the confining di-electric and orange is the quantum well. γ_{SC} is the waveguide-coupled loss for the side-coupled cavity. b) Side-coupled transmission spectrum for increasing values of the waveguide-coupled loss. Parameters: $\kappa/2\pi = 7.77$ GHz, $\gamma_X/2\pi = 566$ GHz, $g/2\pi = 1.2389$ THz.

Following identical steps which concluded with Eq. (3.40), the transmission efficiency is

$$T(\omega) = \left|\frac{\tilde{a}_{out}}{\tilde{a}_{in}}\right|^2 = \left|1 - \frac{i\gamma_{SC}(\omega - \tilde{\omega}_X)}{(\omega - \tilde{\omega}_C)(\omega - \tilde{\omega}_X) - g^2}\right|^2. \tag{3.46}$$

Collecting real and imaginary components of the expression, this can be rewritten as

$$T(\omega) = \left|\frac{[g^2 + \gamma_X(\kappa - \gamma_{SC}) - (\omega - \omega_C)(\omega - \omega_X)] - i\left[\gamma_X(\omega - \omega_C) + (\kappa - \gamma_{SC})(\omega - \omega_X)\right]}{[g^2 + \gamma_X\kappa - (\omega - \omega_C)(\omega - \omega_X)] - i\left[\gamma_X(\omega - \omega_C) + \kappa(\omega - \omega_X)\right]}\right|^2. \tag{3.47}$$

For a single-mode, side-coupled resonator the transmitted spectrum of the exciton-resonator system is then

$$T(\omega) = \frac{[g^2 + \gamma_X(\kappa - \gamma_{SC}) - (\omega - \omega_C)(\omega - \omega_X)]^2 + [\gamma_X(\omega - \omega_C) + (\kappa - \gamma_{SC})(\omega - \omega_X)]^2}{[g^2 + \gamma_X\kappa - (\omega - \omega_C)(\omega - \omega_X)]^2 + [\gamma_X(\omega - \omega_C) + \kappa(\omega - \omega_X)]^2}. \tag{3.48}$$

Significant transmission contrast can still be achieved in the side-coupling geometry while remaining in the strong coupling regime (Fig. 3.10b). Reaching critical coupling in the side-coupled cavity design requires the waveguide-cavity coupling rate to be the same as the polariton loss, which is necessarily no longer in the strong coupling regime. However, in the under-coupled regime, by carefully choosing the waveguide-cavity coupling rate a measurable transmission contrast can be achieved, as verified numerically. The side-coupled, waveguide-cavity coupling rate (γ_{SC}) essentially provides an additional degree of freedom for cavity design that is absent in in-line cavities.

3.4 Discussion

A theoretical and experimental estimate of the light-matter interaction strength was determined for a monolayer TMD excitonic transition integrated onto a PCDR ($\hbar g = 6.5$ meV). An optimal condition for the of monolayer length was found for observation of avoided crossing in this material system. Despite the improved cooperativity ($C = \frac{g^2}{\gamma_X(\kappa+\gamma)}$) found by maximizing the light-matter interaction, the small transmission efficiency remains a challenge

to experimentally probe the strong coupling regime [97]. This low transmission efficiency may be avoided by decoupling the waveguide-coupled loss from the intrinsic cavity loss, using a side-coupled nanobeam or ring resonator [70, 126]. This allows for an extra degree of freedom to increase the waveguide-coupled loss at a similar rate to that of the cavity broadening from the perturbing monolayer $MoSe_2$. The limiting factor in this material system is the linewidth of the neutral exciton in monolayer $MoSe_2$. hBN encapsulation is a means to narrow the linewidth by modifying the dielectric environment and reducing sample inhomogeneity [127]. However, experiment may be better served by pursuing two-dimensional excitonic transitions with intrinsically narrow linewidths [128].

Additionally, the difficulty remains in the necessary tuning range of the microresonator and/or exciton resonance to best observe an avoided crossing due to the large linewidth of the excitonic transition. Temperature tuning was used as it is the only mechanism to provide sufficient range of the exciton-cavity detuning to make observation of a coherent interaction in a dispersionless cavity. The disadvantage to temperature tuning is the increased linewidth of the exciton transition at elevated temperatures preventing the observation of strong coupling. As such, a tunable nanocavity at low temperature is necessary to observe strong coupling with a broad optical transition. The quantum confined Stark effect is a possible in situ mechanism for tuning of the excitonic transition, however the in-plane nature of the intralayer exciton dipole moment with an out-of-plane electric field does not have sufficient tuning range to be practically useful [129]. A hetero-bilayer structure supporting interlayer excitons has a distinct advantage as the excitations then support a dipole moment aligned to an out-of-plane electric field [130]. An alternative form of digital tuning would be to transfer a large-area of monolayer TMDs grown via chemical vapor deposition [131, 132] onto an array of nanobeam cavities with different resonant wavelengths. This would allow for the simultaneous observation of multiple exciton-cavity detunings on many devices.

Chapter 4

EXCITON-PHONON INTERACTION

A necessary step for elucidating the potential applications of microresonator quantum electrodynamics (cQED) is an understanding of the relevant underlying physics of the light-matter interaction. The prevailing description of the interaction between quasinormal modes of dielectric microresonators and the excitonic transition in transition metal dichalcogenides (TMDs) largely neglects the role of the solid-state environment. However, exciton-phonon interactions are known to have a significant effect on the neutral exciton photoluminescence (PL) [102, 133–138]. In other solid-state cQED systems, such as self-assembled quantum dots coupled to nanocavities, the exciton-phonon interaction is known to cause an asymmetric photoluminescent lineshape in the form of phonon sidebands as well as modify the cavity-coupled photoluminescence [123, 139, 140]. For TMDs coupled to whispering gallery mode resonators the excitonic photoluminescent emission into the cavity modes appear preferentially coupled to the red-detuned side of the excitonic resonant frequency [6, 112, 141, 142]. This asymmetric coupling, which is not predicted by the simple coupled oscillator model for the light-matter interaction, points to important missing elements in the model.

Interactions of acoustic phonons with the excitonic transition is shown to play a role in the cavity-coupled photoluminescence of monolayer TMDs and dielectric microresonators. The coupled oscillator model for the coupling of the TMD neutral excitonic transition to a quasinormal mode (QNM) [20, 143, 144] is modified to include a deformation potential interaction used to model the exciton-phonon interaction [145, 146], similar to the studies in self-assembled quantum dots coupled to photonic crystal defect resonators (PCDRs). An effective master equation is employed to describe phonon-mediated decay processes and incoherent exciton-cavity coupling [147]. Experimentally, monolayer WSe_2 is transferred onto

a silicon nitride ring resonator which allows for the simultaneous measurement of multiple QNMs at different exciton-cavity detunings. The model exhibits preferential coupling of the exciton emission to red-detuned cavity modes, faithfully reproducing the experimental data. The theoretical model is further validated with a prediction and experimental confirmation that the asymmetry decreases with increasing temperature.

The Hamiltonian description of our system begins with the coupled oscillator model H_{XC} (Eq. (3.29)) wherein the exciton $\Delta_{XL} = \omega_X - \omega_L$ and cavity $\Delta_{CL} = \omega_C - \omega_L$ resonances, measured with respect to a rotating frame at the resonant drive frequency ω_L, interact via an exciton-cavity coupling g [20, 143]. The deformation potential exciton-phonon Hamiltonian ($H_{XP} = H_P + W_{XP}$) [145, 146] is a simplified model to account for effects of the solid state environment similar to that seen in the spin-boson model [148, 149] or for optomechanical systems [150]. In the deformation potential exciton-phonon interaction

$$W_{XP} = \hbar \sum_{q,k,k'} \lambda_q^{k,k'} \hat{b}_{k'}^\dagger \hat{b}_k (\hat{c}_{q,k'-k} + \hat{c}_{q,k-k'}^\dagger) \tag{4.1}$$

the exciton number operator is coupled to a bath of harmonic oscillators $H_P = \sum_q \hbar \omega_q \hat{c}_q^\dagger \hat{c}_q$ with frequency ω_q and coupling $\lambda_q^{k,k'}$. For small momentum transfer ($k' \approx k$) we can substitute the exciton reaction coordinate. The exciton-phonon interaction then reduces to

$$W_{XP} = \hbar \hat{b}^\dagger \hat{b} \sum_q \lambda_q (\hat{c}_q + \hat{c}_q^\dagger) \tag{4.2}$$

The total Hamiltonian is $H = H_{XC} + H_D + H_{XP}$ and

$$H_{XC} = \hbar \Delta_{CL} \hat{a}^\dagger \hat{a} + \hbar \Delta_{XL} \hat{b}^\dagger \hat{b} + \hbar g(\hat{b}^\dagger \hat{a} + \hat{b} \hat{a}^\dagger) \tag{4.3}$$

$$H_D = \hbar \eta_X (\hat{b} + \hat{b}^\dagger) \tag{4.4}$$

$$H_{XP} = \sum_q \hbar \omega_q \hat{c}_q^\dagger \hat{c}_q + \hbar \hat{b}^\dagger \hat{b} \sum_q \lambda_q (\hat{c}_q + \hat{c}_q^\dagger). \tag{4.5}$$

$\hat{a}$ ($\hat{b}$) is the annihilation operator for the cavity (excitonic) mode. In the weak excitation regime, exciton saturation and any exciton-exciton interaction is neglected. Hence, both the

exciton and cavity operators can be treated as bosonic. η_X is the amplitude of a coherent drive for the excitonic transition.

4.1   Polaron transformation

In order to distinguish the observed neutral exciton from the effects associated with phonon bath induced fluctuations, the polaron transformation $P = \hat{b}^\dagger \hat{b} \sum_q \frac{\lambda_q}{\omega_q}(\hat{c}_q^\dagger - \hat{c}_q)$ is used with $H \to e^P H e^{-P}$ [149, 151]. Using the identity $e^X Y e^{-X} = Y + [X, Y] + \frac{1}{2!}[X, [X, Y]] + \frac{1}{3!}[X, [X, [X, Y]]] + \cdots$ and that $\hat{a}$, $\hat{b}$, and $\hat{c}$ are all bosonic operators (e.g. $[\hat{a}, \hat{a}^\dagger] = 1$) leads to

$$\Delta_{XL} b^\dagger b \to \Delta_{XL} b^\dagger b$$

$$\Delta_{CL} a^\dagger a \to \Delta_{CL} a^\dagger a$$

$$b^\dagger b \sum_q \lambda_q (c_q + c_q^\dagger) \to b^\dagger b \sum_q \lambda_q (c_q + c_q^\dagger) - 2(b^\dagger b)^2 \sum_q \frac{\lambda_q^2}{\omega_q}$$

$$= b^\dagger b \sum_q \lambda_q (c_q + c_q^\dagger) - 2(b^\dagger b)^2 \Delta_P$$

$$\sum_q \omega_q c_q^\dagger c_q \to \sum_q \omega_q c_q^\dagger c_q - b^\dagger b \sum_q \lambda_q (c_q + c_q^\dagger) + (b^\dagger b)^2 \sum_q \frac{\lambda_q^2}{\omega_q}$$

$$= \sum_q \omega_q c_q^\dagger c_q - b^\dagger b \sum_q \lambda_q (c_q + c_q^\dagger) + (b^\dagger b)^2 \Delta_P$$

$$g(b^\dagger a + a^\dagger b) + \eta_X(b + b^\dagger) \to g(b^\dagger a + a^\dagger b) + \eta_X(b + b^\dagger)$$

$$+ \left[\sum_q \frac{\lambda_q}{\omega_q}(c_q^\dagger - c_q)\right][g(b^\dagger a - a^\dagger b) + \eta_X(b - b^\dagger)]$$

$$+ \left[\sum_q \frac{\lambda_q}{\omega_q}(c_q^\dagger - c_q)\right]^2[g(b^\dagger a + a^\dagger b) + \eta_X(b + b^\dagger)]$$

$$+ \left[\sum_q \frac{\lambda_q}{\omega_q}(c_q^\dagger - c_q)\right]^3[g(b^\dagger a - a^\dagger b) + \eta_X(b - b^\dagger)] + \cdots$$

$$= \exp\left[\sum_q \frac{\lambda_q}{\omega_q}(c_q^\dagger - c_q)\right](gb^\dagger a + \eta_X b) + \exp\left[-\sum_q \frac{\lambda_q}{\omega_q}(c_q^\dagger - c_q)\right](ga^\dagger b + \eta_X b^\dagger)$$

$$= g(\underbrace{C_+ b^\dagger a}_{1} + \underbrace{C_- a^\dagger b}_{2}) + \eta_X(\underbrace{C_+ b^\dagger}_{3} + \underbrace{C_- b}_{4})$$

$$= \frac{1}{2}[\underbrace{gC_+ a^\dagger b}_{I} + \underbrace{gC_+ b^\dagger a}_{1} + \underbrace{\eta_X C_+ b}_{III} + \underbrace{\eta_X C_+ b^\dagger}_{3}$$

$$+ \underbrace{gC_- a^\dagger b}_{2} + \underbrace{gC_- b^\dagger a}_{II} + \underbrace{\eta_X C_- b}_{4} + \underbrace{\eta_X C_- b^\dagger}_{IV}$$

$$+ \underbrace{gC_+ b^\dagger a}_{1} - \underbrace{gC_+ a^\dagger b}_{I} + \underbrace{\eta_X C_+ b^\dagger}_{3} - \underbrace{\eta_X C_+ b}_{III}$$

$$- \underbrace{gC_- b^\dagger a}_{II} + \underbrace{gC_- a^\dagger b}_{2} - \underbrace{\eta_X C_- b^\dagger}_{IV} + \underbrace{\eta_X C_- b}_{4}]$$

$$= \frac{1}{2}(C_+ + C_-)[g(a^\dagger b + b^\dagger a) + \eta_X(b + b^\dagger)]$$

$$+ \frac{1}{2}(C_+ - C_-)[g(b^\dagger a - a^\dagger b) + \eta_X(b^\dagger - b)]$$

$$= \frac{1}{2}(C_+ + C_-)X_g + \frac{1}{2i}(C_+ - C_-)X_u$$

$$= \frac{1}{2}(C_+ + C_- - 2\langle C\rangle)X_g + \langle C\rangle X_g + \frac{1}{2i}(C_+ - C_-)X_u$$

$$= \zeta_g X_g + \zeta_u X_u + \langle C\rangle X_g$$

The polaron shift is defined $\Delta_P = \sum_q \frac{\lambda_q^2}{\omega_q} = \int_0^\infty d\omega J(\omega)/\omega$ and the exciton-cavity coupling terms

$$X_g = \hbar g(a^\dagger b + b^\dagger a) + \hbar \eta_X (b + b^\dagger)$$

$$X_u = i\hbar g(b^\dagger a - a^\dagger b) + i\hbar \eta_X (b^\dagger - b)$$

$J(\omega)$ is the phonon spectral function. The bath displacement operators $C_\pm = \exp\left[\pm \sum_q \frac{\lambda_q}{\omega_q}(c_q - c_q^\dagger)\right]$ are included in the exciton-cavity prefactors

$$\zeta_g = \frac{1}{2}(C_+ + C_- - 2\langle C \rangle)$$

$$\zeta_u = \frac{1}{2i}(C_+ - C_-)$$

where $\langle C \rangle = \langle C_+ \rangle = \langle C_- \rangle$. The resulting system, bath, and interaction Hamiltonian give

$$H_S' = \hbar \Delta_{CL} a^\dagger a + \hbar \Delta_{XL} b^\dagger b - \hbar \Delta_P (b^\dagger b)^2 + \langle C \rangle X_g \tag{4.6}$$

$$= \hbar \Delta_{CL} a^\dagger a + \hbar (\Delta_{XL} - \Delta_P) b^\dagger b - \hbar \Delta_P b^\dagger b^\dagger bb + \langle C \rangle X_g \tag{4.7}$$

$$H_B' = \sum_q \hbar \omega_q c_q^\dagger c_q \tag{4.8}$$

$$H_I' = X_g \zeta_g + X_u \zeta_u \tag{4.9}$$

Eq. (4.7) is the effective Hamiltonian describing the transformed system [148, 150, 152, 153]. The exciton resonance $\Delta_{xL}' = \Delta_{xL} - \Delta_P$ is renormalized by a polaron shift $\Delta_P = \sum_q \frac{\lambda_q^2}{\omega_q}$, which is analogous to a Lamb shift [154]. When the harmonic oscillator bath is written in terms of the phonon displacement operator $C_\pm = \exp\left[\pm \sum_q \frac{\lambda_q}{\omega_q}(c_q - c_q^\dagger)\right]$ the exciton-cavity coupling is modified from the bare value by the average phonon displacement $\langle C \rangle$

$$\langle C \rangle = \exp\left[-\frac{1}{2}\sum_q \left(\frac{\lambda_q}{\omega_q}\right)^2 (2\bar{n}_q + 1)\right]$$

where $\bar{n}_q = [e^{\beta \hbar \omega_q} - 1]^{-1}$ is the mean phonon number with bath temperature $T = 1/k_B \beta$ [155]. As the temperature increases, the average phonon number in each mode increases, which decreases the light-matter interaction strength.

4.2 Effective master equation

The Markovian time-convolutionless (TCL) master equation can be used to approximate the temporal dynamics of the system and derive an effective master equation that models the incoherent exciton-cavity feeding [149, 153, 155–158].

$$\frac{\partial \rho(t)}{\partial t} = \frac{1}{i\hbar}[H'_S, \rho(t)] + \mathcal{L}(\rho) - \frac{1}{\hbar^2} \int_0^\infty d\tau \sum_{m=g,u} \{G_m(\tau)[\hat{X}_m, e^{-iH'_S\tau/\hbar}\hat{X}_m e^{iH'_S\tau/\hbar}\rho(t)] + H.c.\}$$

(4.10)

$G_m(t)$ are the polaron Green functions $(m = g, u)$

$$G_g(t) = \langle C \rangle^2 \cosh[\phi(t)] - 1$$

$$G_u(t) = \langle C \rangle^2 \sinh[\phi(t)]$$

and $\phi(\tau) = \int_0^\infty d\omega \frac{J(\omega)}{\omega^2} \left[\coth\left(\frac{\hbar\omega}{2k_BT}\right)\cos(\omega\tau) - i\sin(\omega\tau)\right]$ is the phonon correlation function. The average phonon displacement can be calculated as $\langle C \rangle = \exp(-\phi(0)/2)$ [158].

To approximate the integral in the master equation the cavity-exciton detuning (Δ_{CX}) is assumed to be large compared to g and weak excitation such that $\langle b^\dagger b \rangle << 1$. In the interaction picture this reduces to

$$e^{-iH'_S\tau/\hbar}\hat{X}_m e^{iH'_S\tau/\hbar} \simeq e^{-iH'_0\tau/\hbar}\hat{X}_m e^{iH'_0\tau/\hbar}$$

(4.11)

with $H'_0 = \hbar\Delta_{CL}a^\dagger a + \hbar(\Delta_{XL} - \Delta_P)b^\dagger b$ where $\Delta_{XL} - \Delta_P \to \Delta_{XL}$ is renormalized. The component transformations become

$$e^{-iH'_0\tau/\hbar}be^{iH'_0\tau/\hbar} = b^\dagger e^{-i\Delta_{XL}\tau}$$

$$e^{-iH'_0\tau/\hbar}b^\dagger e^{iH'_0\tau/\hbar} = b^\dagger e^{i\Delta_{XL}\tau}$$

$$e^{-iH'_0\tau/\hbar}a^\dagger be^{iH'_0\tau/\hbar} = a^\dagger e^{i\Delta_{CL}\tau}be^{-i\Delta_{XL}\tau}$$

$$= a^\dagger be^{-i\Delta_{CX}\tau}$$

$$e^{-iH'_0\tau/\hbar}b^\dagger ae^{iH'_0\tau/\hbar} = b^\dagger e^{i\Delta_{XL}\tau}ae^{-i\Delta_{CL}\tau}$$

$$= b^\dagger ae^{i\Delta_{CX}\tau}$$

Without the coherent driving term, substitution gives

$$G_g(\tau)[\hat{X}_g, e^{-iH'_S\tau/\hbar}\hat{X}_g e^{iH'_S\tau/\hbar}\rho(t)] + H.c.$$

$$\simeq \hbar^2 g^2 G_g(\tau)(a^\dagger b + b^\dagger a)(a^\dagger b e^{i\Delta_{CX}\tau} + b^\dagger a e^{-i\Delta_{CX}\tau})\rho(t)$$

$$- \hbar^2 g^2 G_g(\tau)(a^\dagger b e^{i\Delta_{CX}\tau} + b^\dagger a e^{-i\Delta_{CX}\tau})\rho(t)(a^\dagger b + b^\dagger a)$$

$$+ \hbar^2 g^2 G_g^*(\tau)\rho(t)(a^\dagger b e^{-i\Delta_{CX}\tau} + b^\dagger a e^{i\Delta_{CX}\tau})(a^\dagger b + b^\dagger a)$$

$$- \hbar^2 g^2 G_g^*(a^\dagger b + b^\dagger a)\rho(t)(a^\dagger b e^{-i\Delta_{CX}\tau} + b^\dagger a e^{i\Delta_{CX}\tau})$$

$$= \hbar^2 g^2 [G_g(\tau)e^{-i\Delta_{CX}\tau}\underbrace{b^\dagger a a^\dagger b\rho(t)}_{1} + G_g(\tau)e^{i\Delta_{CX}\tau}\underbrace{a^\dagger b b^\dagger a\rho(t)}_{5}]$$

$$- \hbar^2 g^2 [G_g(\tau)e^{-i\Delta_{CX}\tau}\underbrace{a^\dagger b\rho(t)b^\dagger a}_{3} + G_g(\tau)e^{i\Delta_{CX}\tau}\underbrace{b^\dagger a\rho(t)a^\dagger b}_{7}]$$

$$+ \hbar^2 g^2 [G_g^*(\tau)e^{-i\Delta_{CX}\tau}\underbrace{\rho(t)a^\dagger b b^\dagger a}_{6} + G_g^*(\tau)e^{i\Delta_{CX}\tau}\underbrace{\rho(t)b^\dagger a a^\dagger b}_{2}]$$

$$- \hbar^2 g^2 [G_g^*(\tau)e^{-i\Delta_{CX}\tau}\underbrace{b^\dagger a\rho(t)a^\dagger b}_{8} + G_g^*(\tau)e^{i\Delta_{CX}\tau}\underbrace{a^\dagger b\rho(\tau)b^\dagger a}_{4}]$$

$$= \hbar^2 g^2 \{\underbrace{\Re[G_g(t)e^{-i\Delta_{CX}\tau}]b^\dagger a a^\dagger b\rho(t) + i\Im[G_g(\tau)e^{-i\Delta_{CX}\tau}]b^\dagger a a^\dagger b\rho(t)}_{1}\}$$

$$+ \hbar^2 g^2 \{\underbrace{\Re[G_g(\tau)e^{-i\Delta_{CX}\tau}]\rho(t)b^\dagger a a^\dagger b - i\Im[G_g(\tau)e^{-i\Delta_{CX}\tau}]\rho(t)b^\dagger a a^\dagger b}_{2}\}$$

$$- \hbar^2 g^2 \{\underbrace{G_g(\tau)e^{-i\Delta_{CX}\tau}a^\dagger b\rho(t)b^\dagger a}_{3} + \underbrace{G_g^*(\tau)e^{i\Delta_{CX}\tau}a^\dagger b\rho(t)b^\dagger a}_{4}\}$$

$$+ \hbar^2 g^2 \{\underbrace{\Re[G_g(\tau)e^{i\Delta_{CX}\tau}]a^\dagger b b^\dagger a\rho(t) + i\Im[G_g(\tau)e^{i\Delta_{CX}\tau}]a^\dagger b b^\dagger a\rho(t)}_{5}\}$$

$$+ \hbar^2 g^2 \{\underbrace{\Re[G_g(\tau)e^{i\Delta_{CX}\tau}]\rho(t)a^\dagger b b^\dagger a - i\Im[G_g(\tau)e^{i\Delta_{CX}\tau}]\rho(t)a^\dagger b b^\dagger a}_{6}\}$$

$$- \hbar^2 g^2 \{\underbrace{G_g(\tau)e^{i\Delta_{CX}\tau}b^\dagger a\rho(t)a^\dagger b}_{7} + \underbrace{G_g^*(\tau)e^{-i\Delta_{CX}\tau}b^\dagger a\rho(t)a^\dagger b}_{8}\}$$

$$G_g(\tau)[\hat{X}_g, e^{-iH'_S\tau/\hbar}\hat{X}_g e^{iH'_S\tau/\hbar}\rho(t)] + H.c.$$

$$\simeq \hbar^2 g^2 \Re[G_g(\tau)e^{-i\Delta_{CX}\tau}](\underbrace{b^\dagger aa^\dagger b\rho(t)}_{\Re[1]} + \underbrace{\rho(t)b^\dagger aa^\dagger b}_{\Re[2]} - \underbrace{2a^\dagger b\rho(t)b^\dagger a}_{3+4})$$

$$+ \hbar^2 g^2 \Re[G_g(\tau)e^{i\Delta_{CX}\tau}](\underbrace{a^\dagger bb^\dagger a\rho(t)}_{\Re[5]} + \underbrace{\rho(t)a^\dagger bb^\dagger a}_{\Re[6]} - \underbrace{2b^\dagger a\rho(t)a^\dagger b}_{7+8})$$

$$+ i\hbar^2 g^2 \Im[G_g(\tau)e^{-i\Delta_{CX}\tau}](\underbrace{b^\dagger aa^\dagger b\rho(t)}_{\Im[1]} - \underbrace{\rho(t)b^\dagger aa^\dagger b}_{\Im[2]})$$

$$+ i\hbar^2 g^2 \Im[G_g(\tau)e^{i\Delta_{CX}\tau}](\underbrace{a^\dagger bb^\dagger a\rho(t)}_{\Im[5]} - \underbrace{\rho(t)a^\dagger bb^\dagger a}_{\Im[6]})$$

Eight terms are lost in the first equality by cancellation with terms from the integrand containing X_u due to the imaginary i giving an overall minus sign to the manipulations. By inspection of the last equality all $a^\dagger$ are replaced by $-a^\dagger$ for the integrand with $X_u(\tau)$ but the overall minus sign negates this. Then $m = g, u$ can be summed over.

$$g^2 \int_0^\infty d\tau \sum_{m=g,u} \{\Re[G_m(\tau)e^{-i\Delta_{CX}\tau}](b^\dagger aa^\dagger b\rho(t) + \rho(t)b^\dagger aa^\dagger b - 2a^\dagger b\rho(t)b^\dagger a)$$

$$+ \Re[G_m(\tau)e^{i\Delta_{CX}\tau}](a^\dagger bb^\dagger a\rho(t) + \rho(t)a^\dagger bb^\dagger a - 2b^\dagger a\rho(t)a^\dagger b)$$

$$+ i\Im[G_m(\tau)e^{-i\Delta_{CX}\tau}](b^\dagger aa^\dagger b\rho(t) - \rho(t)b^\dagger aa^\dagger b)$$

$$+ i\Im[G_m(\tau)e^{i\Delta_{CX}\tau}](a^\dagger bb^\dagger a\rho(t) - \rho(t)a^\dagger bb^\dagger a)\}$$

Recall $\sum_{m=g,u} G_m(\tau) = \langle C \rangle^2 (e^{\phi(\tau)} - 1)$ and the dissipator is defined $\mathcal{L}[\xi] = \xi\rho\xi^\dagger - \frac{1}{2}\xi^\dagger\xi\rho - \frac{1}{2}\rho\xi^\dagger\xi$ with Lindbladian operators ξ. The resulting term becomes

$$i[\Delta_{ph}^{b^\dagger a}b^\dagger aa^\dagger b + \Delta_{ph}^{a^\dagger b}a^\dagger bb^\dagger a, \rho(t)] + \frac{\Gamma_{ph}^{b^\dagger a}}{2}\mathcal{L}(b^\dagger a) + \frac{\Gamma_{ph}^{a^\dagger b}}{2}\mathcal{L}(a^\dagger b) \qquad (4.12)$$

The frequency shifts are given as

$$\Delta_{ph}^{b^\dagger a/a^\dagger b} = \langle C \rangle^2 g^2 \text{Im}\left[\int_0^\infty d\tau e^{\pm i\Delta_{CX}\tau}(e^{\phi(\tau)} - 1)\right] \qquad (4.13)$$

The scattering rates are given as

$$\Gamma_{ph}^{b^\dagger a/a^\dagger b} = 2\langle C \rangle^2 g^2 \text{Re}\left[\int_0^\infty d\tau e^{\pm i\Delta_{CX}\tau}(e^{\phi(\tau)} - 1)\right] \qquad (4.14)$$

Ignoring cross-terms in the integrand commutator between the coherent exciton-cavity interaction g and coherent exciton drive η_X, a rederivation can be avoided by observing all a and $a^\dagger$ can be removed, replacing $g \to \eta_X$, and replacing $\Delta_{CX} \to \Delta_{XL}$. The resulting term becomes

$$i[\Delta_{ph}^{b^\dagger} b^\dagger b + \Delta_{ph}^{b} bb^\dagger, \rho(t)] + \frac{\Gamma_{ph}^{b^\dagger}}{2}\mathcal{L}(b^\dagger) + \frac{\Gamma_{ph}^{b}}{2}\mathcal{L}(b) \tag{4.15}$$

The frequency shifts are given

$$\Delta_{ph}^{b^\dagger/b} = \langle C \rangle^2 \eta_X^2 \text{Im}\left[\int_0^\infty d\tau e^{\pm i\Delta_{XL}\tau}(e^{\phi(\tau)} - 1)\right] \tag{4.16}$$

The scattering rates are given

$$\Gamma_{ph}^{b^\dagger/b} = 2\langle C \rangle^2 \eta_X^2 \text{Re}\left[\int_0^\infty d\tau e^{\pm i\Delta_{XL}\tau}(e^{\phi(\tau)} - 1)\right] \tag{4.17}$$

For the purposes of simulation and fitting to the data the AC Stark shifts $\Delta_{ph}^{b^\dagger a/a^\dagger b}$ and $\Delta_{ph}^{b^\dagger/b}$ are ignored which do not contribute modifications to the spectrum in the linear regime.

4.3   Excitonic photoluminescence

Before considering the cavity-coupled photoluminescence, the quantum optical model is first applied to the excitonic photoluminescence without cavity integration. Photoluminescence (PL) is measured to confirm the presence of the monolayer after material transfer because 2D materials exhibit poor optical contrast on the SiN substrate (Fig. 4.1d). The strong excitonic peak of the WSe$_2$ monolayer integrated onto the SiN ring resonator establishes the presence of the vdW material on the waveguide [77]. The primary peak is attributed to neutral exciton emission. The secondary sidebands are likely due to defects or trion emission [28, 87]. PL is measured by exciting the monolayer with a HeNe laser (40 µW at 633 nm). By fitting the measured PL at 80 K, the material dependent parameters for the phonon spectral function can be calculated, independent of the cavity coupling. An exciton linewidth $\gamma = 48.4$ meV is measured with an exciton-phonon coupling $\alpha_p = 0.018$ ps^2 and cutoff frequency $\omega_b = 6.7$ meV. These extracted parameters are consistent with values estimated from bulk material measurements discussed in the following numerical details. The polaron shift of the exciton
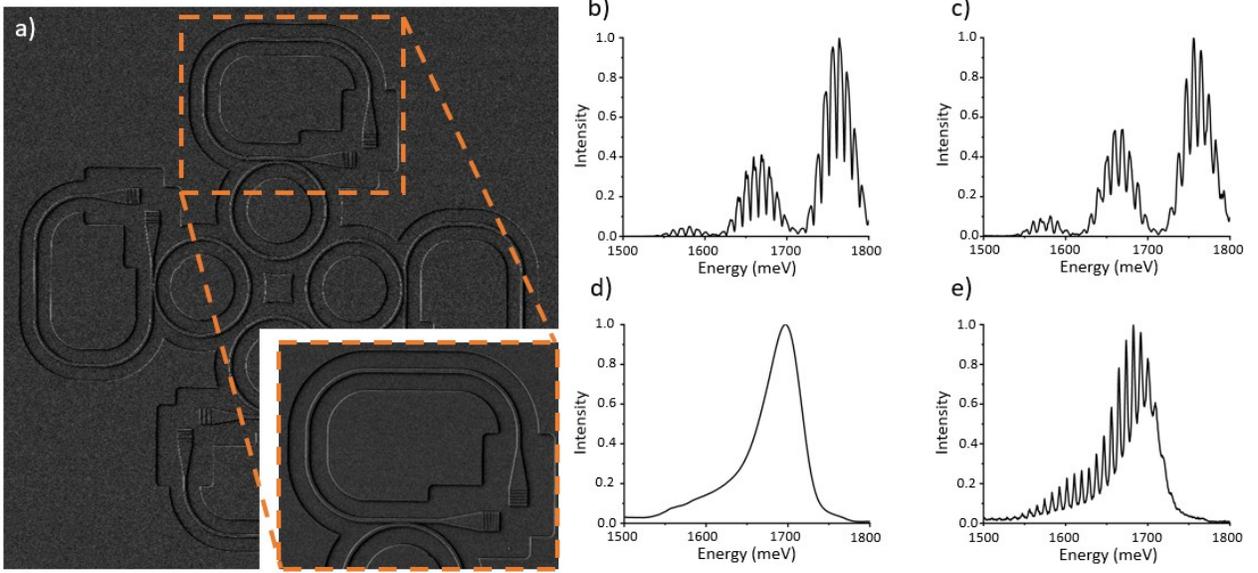
Figure 4.1: **Photoluminescence and transmission spectra.** a) SEM of four 5 µm (radius) uncoupled SiN ring resonators. Inset: SEM of the coupled ring/waveguide and grating couplers. The grating couplers are used to input light and collect transmitted light. b) Transmission spectrum of the SiN ring resonator before integration of monolayer WSe$_2$. c) Transmission spectrum of the SiN ring resonator after integration of monolayer WSe$_2$. d) PL of monolayer WSe$_2$. e) Cavity-coupled PL of monolayer WSe$_2$.

energy is then calculated to be $\hbar\Delta_P = \hbar \int_0^\infty d\omega J(\omega)/\omega = \hbar\sqrt{\frac{\pi}{2}}\alpha_p \omega_b^3 = 24$ meV, which is incorporated into the modified exciton resonance $\Delta'_{xL} = \Delta_{xL} - \Delta_P$.

4.3.1   Numerical details

It is important to note the photonic devices are fabricated on a 220 nm thick SiN membrane grown via LPCVD on 4 µm of thermal oxide on silicon. The underlying silicon is opaque to the wavelengths of the excitonic transition in monolayer transition metal dichalcogenides, hence absorption spectroscopy is not possible. Alternatively, a differential reflectance measurement may be considered. However, the structured surface of the photonic devices does not provide

a good (i.e. flat) substrate for high-quality measurements. This limits the experiment to using the photoluminescence as a proxy for the neutral exciton lineshape. Independent differential reflectivity measurements on monolayer TMDs find agreement with the photoluminescence peaks, within a classical understanding of disordered two-dimensional semiconductors [159].

The steady-state exciton population [160] without cavity-coupling can be found for comparison to PL measurements

$$\bar{N}_X = \frac{1}{2} \left[1 + \frac{\Gamma_{ph}^{\sigma^+} - \Gamma_{ph}^{\sigma^-} - \gamma}{\Gamma_{ph}^{\sigma^+} + \Gamma_{ph}^{\sigma^-} + \gamma + \frac{4\eta_x^2 \langle B \rangle^2 \Gamma_{pol}}{\Gamma_{pol}^2 + \Delta_{XL}^2}} \right] \tag{4.18}$$

with $\Gamma_{pol} = \frac{1}{2}(\Gamma_{ph}^{\sigma^+} + \Gamma_{ph}^{\sigma^-} + \gamma)$. For numerical fitting of the data to this model $\eta_X \equiv 0.01\gamma$. The coefficient choice does not significantly affect the lineshape of $\bar{N}_x$. Fixed parameters in this model are temperature (T) and the exciton decay rate (γ) extracted from the linewidth of the exciton resonance. $\bar{N}_X$ reduces to a Lorentzian with full width at half maximum (FWHM) equal to γ. Free parameters of the model are the exciton-phonon coupling strength (α_p) and cutoff frequency (ω_b).

Photoluminescence involves above-band excitation which phenomenologically amounts to an incoherent drive of the neutral exciton. Our presented simplified model requires a coherent drive for phonon-mediated processes as seen by the η_X in the $\Gamma_{ph}^{a^\dagger/a}$ scattering rates. By representing the incoherent excitation as a coherent field with a random phase [161, 162] the Markovian approximation made for the TCL master equation allows for the consideration of a steady state population of neutral excitons by effectively integrating out the transient dynamics.

The secondary sidebands observed in the photoluminescence spectra are assumed to be defects or trions [28, 87] and are fit using a Gaussian and Lorentzian function, respectively. The emission is inferred to be from defects because a fraction of the red-detuned photoluminescence is quenched at elevated temperatures [163]. As single defect emission is known to have a relatively narrow linewidth the inhomogeneous broadening is assumed to dominatesin the observed linewidth of the defect emission [136, 164]. Similarly, for the trion emission a

Lorentzian lineshape is chosen as is often done in the literature [136, 165, 166]. The remaining photoluminescence is fit to the steady-state exciton population of equation 4.18 which amounts to asymmetric emission on the blue-detuned side of the neutral exciton [102, 137]. The total PL spectrum is fit using SciPy's ***curve_fit*** function for the Gaussian and Lorentzian terms, and a brute force grid search for α_p and ω_b (Fig 4.2).

$$S_{PL}(\Delta_{XL}) = y_0 + \frac{A_D e^{\frac{-4\ln 2(\Delta_{XL} - \Delta_D)^2}{\Gamma_D^2}}}{\Gamma_D \sqrt{\frac{\pi}{4\ln 2}}} + \frac{2A_T}{\pi} \frac{\Gamma_T}{4(\Delta_{XL} - \Delta_T)^2 + \Gamma_T^2} + f\bar{N}_X(\Delta_{XL}) \quad (4.19)$$

The defect ($\Delta_D = -82.31$ meV) and trion ($\Delta_T = -26.55$ meV) peak detunings with respect to the neutral exciton are consistent with previous results in the literature ($\Delta_D \approx -101$ meV, $\Delta_T \approx -28$ meV) [87, 167].

Although there are excellent papers on the subject of phonon-mediated interactions in monolayer materials [102, 133, 137, 168], there is no clear comparison for α_p and ω_b. Consider α_p for a spherically confining potential is known to be $\frac{(D_c - D_v)^2}{4\pi^2 \rho s^5}$ [169–171]. D_c (D_v) are the deformation potential constants for the conduction (valence) band, ρ is the bulk material density, and s is the sound velocity. Using the bulk material parameters for WSe$_2$ with $|D_c - D_v| = 5.4$ eV [172], $\rho = 9.32$ g cm^{-3} [173], and $s = 4000$ m s^{-1} [174], the derived value is $\alpha_p = 0.019$ meV, which is similar to the extracted result of $\alpha_p = 0.018$ meV. The phonon cutoff energy $\omega_b = \frac{s}{d} = 6.7$ meV corresponds to a $d = 3$ nm in-plane localization. This length scale is not unreasonable for an estimate of the silicon nitride surface roughness. There may also be some correlation between the localization and defect emission.

The deformational potential ansatz assumes coupling to acoustic phonons [145]. The linear dispersion for acoustic phonons leads to the super-ohmic spectral density function. The spectral density function is introduced in terms of a localizing length scale. Alternatively, it can be understood as analogous to the Debye model for the phonon contribution to the heat capacity of a solid where a low frequency power law dependence is assumed with a soft energy cutoff [148]. At lower temperatures a more quantitative representation of the phonon spectral function accounting for the thermal occupancy of specific phonon modes would then be necessary [175].
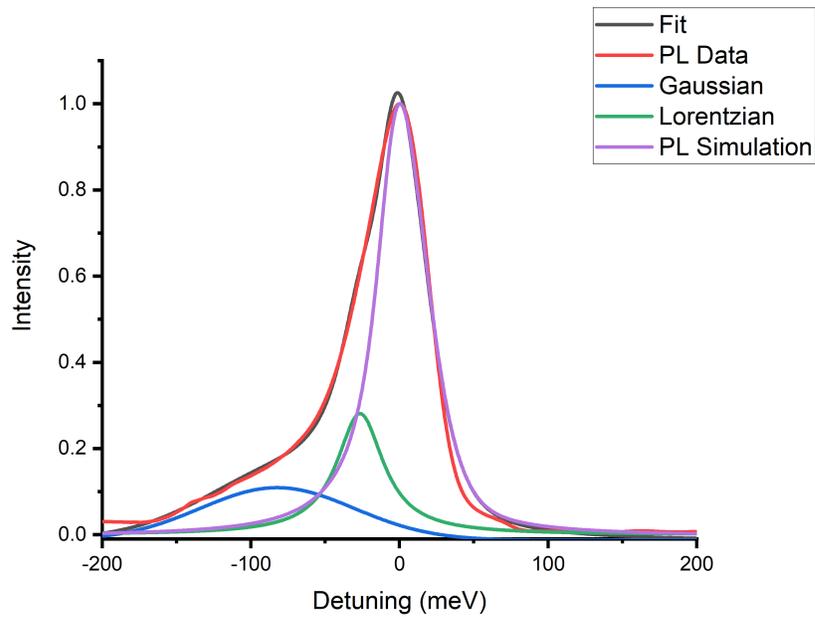
Figure 4.2: **Photoluminescence spectra and fit for an excitonic transition.** The extracted fit parameters for equation 4.19 are: $y_0 = -0.01262$, $A_D = 15.82$, $\Gamma_D = 122.0$ meV, $\Delta_D = -82.31$ meV, $A_T = 17.02$, $\Gamma_T = 38.56$ meV, $\Delta_T = -26.55$ meV, $f = 0.9038$, $\alpha_p = 0.018$ ps^2, and $\omega_b = 6.7$ meV.

4.4 Cavity-coupled photoluminescence

The resulting effective master equation derived above is $\frac{\partial \rho}{\partial t} = \frac{1}{i\hbar}[H'_S, \rho] + \frac{\kappa}{2}\mathcal{L}[a] + \frac{\gamma_X}{2}\mathcal{L}[b] + \frac{\Gamma^{b\dagger a}_{ph}}{2}\mathcal{L}[b^\dagger a] + \frac{\Gamma^{a\dagger b}_{ph}}{2}\mathcal{L}[a^\dagger b]$ [147] with the effective Hamiltonian in Eq. (4.7). Figure 4.3a illustrates the energy-level diagram of the exciton and cavity system. The dissipator $\mathcal{L}[\xi]$ with Lindblad operators ξ describes the cavity decay rate (κ), exciton decay rate (γ), and the incoherent phonon-mediated exciton-cavity scattering ($\Gamma^{b\dagger a}_{ph}$, $\Gamma^{a\dagger b}_{ph}$).

The phonon-mediated exciton-cavity scattering (Fig. 4.3b) with cavity-exciton detuning $\Delta_{CX} = \omega_C - \omega_X$ is given by

$$\Gamma^{a\dagger c/c\dagger a}_{ph} = 2\langle B\rangle^2 g^2 \text{Re}\left[\int_0^\infty d\tau e^{\pm\Delta_{CX}\tau}(e^{\phi(\tau)} - 1)\right] \qquad (4.20)$$

with the phonon correlation function $\phi(\tau) = \int_0^\infty d\omega \frac{J(\omega)}{\omega^2}\left[\coth\left(\frac{\hbar\omega}{2k_BT}\right)\cos(\omega\tau) - i\sin(\omega\tau)\right]$ [148, 156]. A Gaussian localization of the exciton is assumed, confined to the monolayer TMD due to substrate inhomogeneities coupled to acoustic phonons for a qualitative super-ohmic spectral density $J(\omega) = \alpha_p\omega^3 \exp(-\omega^2/2\omega_b^2)$ [145, 148] with α_p and ω_b serving as the exciton-phonon coupling strength and cutoff frequency, respectively. This phonon spectral function is identical to that used in quantum dot studies of phonon interactions [153, 169, 170].

Without phonon-mediated scattering the peak cavity intensity occurs at zero detuning ($\omega_C = \omega_X$) and the cavity-coupled PL is symmetric with respect to the exciton PL emission peak (Fig. 4.3c). The additional scattering from phonon processes of the exciton into the cavity mode dominates when the cavity is red-detuned with respect to the exciton (Fig. 4.3d). Physically, down-conversion of an exciton into a phonon and cavity photon is expected as an example of a Stokes process. Including phonon-mediated scattering demonstrates the peak cavity intensity is red-detuned with respect to the exciton PL emission peak. Furthermore, the model predicts that at the same detuning, the relative intensity between the red-detuned and blue-detuned cavity-coupled photoluminescence decreases for increasing temperature (Fig. 4.3d, dashed line) [147].

To validate the quantum optical model, experiments are performed with a ring resonator
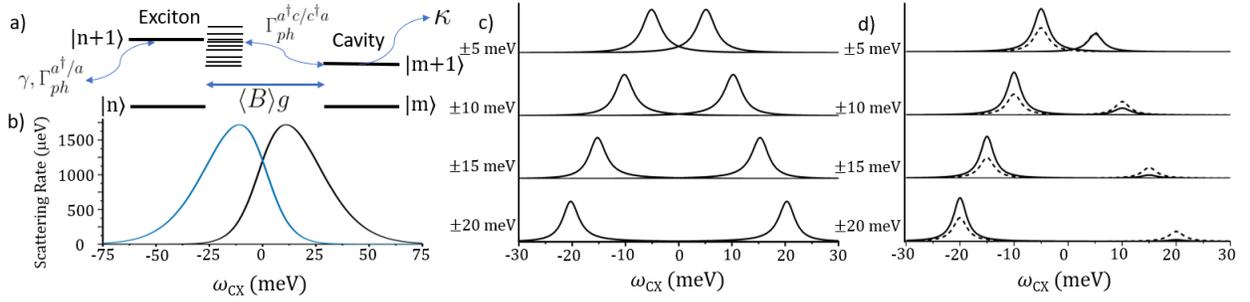
Figure 4.3: **Exciton-cavity detuning dependent phonon-mediated scattering.** Theoretical modeling with the Hamiltonian described in the text ($T = 80$ K, $\gamma = 48.4$ meV, $\alpha_p = 0.018$ ps^2, $\omega_b = 6.7$ meV, $\kappa = 2.85$ meV, $g = 4$ meV) a) Level diagram with phonon-mediated scattering. b) Asymmetric phonon-mediated exciton-cavity coupling rates. The blue line gives the phonon-mediated incoherent emission into the cavity. Note that the peak is not centered at zero detuning. c) Detuning dependent ($\Delta_{CX} = \pm 5, \pm 10, \pm 15, \pm 20$ meV) cavity emission without phonons. d) Detuning dependent cavity emission with phonons at 80 K (solid line) and 320 K (dashed line). Note that for the $\Delta_{CX} = \pm 5$ meV the dashed and solid line are on top of each other for the blue detuned case.

integrated with a monolayer of WSe$_2$. A ring resonator can support multiple cavity modes separated by the free spectral range, and thus provides an ideal platform for studying the coupling of the photoluminescence to cavity modes with different detunings from the exciton.

The transmission spectrum of the SiN ring resonator is measured by exciting a grating coupler with a supercontinuum laser (Fianium WhiteLase Micro) and collecting from the other grating coupler (Fig. 4.1a, inset). An initial transmission measurement of the ring resonator before monolayer TMD transfer yields the bare cavity linewidth of $\kappa = 2.85$ meV (Fig. 4.1b). The dips in the transmission correspond to the resonance in the ring resonators. The separation between the modes corresponds to the free spectral range (FSR $= \frac{c}{2\pi n_{eff} R} \approx 4.8$ THz) of the ring resonator, which matches the FSR expected from the ring radius ($R = 5$ µm) and effective index of refraction of the SiN waveguide ($n_{eff} \approx 2$). The envelope modulation of the spectrum is due to the frequency-dependent coupling efficiency of the grating couplers (Figs. 4.1b and 4.1c). The angular dependence of the grating coupler does not affect the cavity-coupled PL measurement due to the large numerical aperture of the objective lens. There exists a relative amplitude change between the envelope modulation function in the observed transmission spectrum due to the angular dependence of the grating couplers. As the measurement is done before and after the transfer, which requires removing the sample from the optical setup, the angular alignment of the confocal microscope objective to the grating coupler will be slightly different [14]. The transmission spectrum of the ring resonator after material transfer demonstrates the monolayer does not significantly affect the cavity modes (Fig. 4.1c). It is important to point out that with the exciton at approximately 1700 meV, the small linewidth increase seen in the transmission spectrum equally affects cavity modes both red and blue-detuned with respect to the exciton resonance.

Cavity-coupled PL is measured by directly exciting the monolayer WSe$_2$ from the top and collecting the resulting emission from a grating coupler using a pinhole in the image plane of a free-space confocal microscope. Cavity-coupled PL exhibits asymmetric emission into the cavity modes where there is greater intensity in the cavities red-detuned with respect to the exciton (Fig. 4.1e). The coherent exciton-cavity coupling $\hbar g$ can be extracted by considering

the linear superposition of all cavity resonances for the ring resonator and including a contribution from background PL that is difficult to completely remove due to the proximity of the grating coupler and laser excitation of the monolayer WSe_2. The exciton-cavity coupling accounting for the average phonon displacement is found to be $\hbar g \approx 4 - 6$ meV (Fig. 4.4) by a brute force search minimizing the least squares error between the simulated and observed data over a windowed region of the cavity-coupled PL spectrum. The far red-detuned data attributed to defect and trion emission was accounted for by a convolution of the PL and Lorentzian cavity modes.

In this experiment only $\sim 1/4$ of the SiN ring resonator was covered with monolayer WSe_2. A full coverage of monolayer WSe_2 on the SiN ring resonator gives $\hbar g \approx 8 - 12$ meV as an estimated coherent interaction of the exciton and cavity mode due to the $g \propto \sqrt{N}$ scaling of the light-matter interaction in the collective excitation basis and assuming the number of available exciton states is proportional to the area of monolayer material on the cavity. The extracted g value is consistent with the light-matter interaction $\hbar g \approx 10 - 14$ meV found in strong-coupling experiments with van der Waals materials integrated on photonic crystal cavities with comparable cavity length [22, 26, 27].

To further confirm the theoretical model, the temperature-dependent variation in the asymmetric coupling was measured in the range 80 K - 320 K. Using liquid nitrogen in a continuous flow cryostat (Janis ST-500) the energy of the exciton can be tuned in the monolayer WSe_2 from 1650 meV - 1700 meV with the consequent changes in linewidth. As the cryostat temperature is increased, cavity-coupled PL extends to farther blue-detuned cavities with respect to the exciton energy (Fig. 4.5a) where the spectra are shifted by the exciton center frequency. In particular, the maximum detuning with visible cavity modes increases with increasing temperature (Fig. 4.5b). The model Hamiltonian parameters extracted from the PL and cavity-coupled PL qualitatively reproduce the spectrum at elevated temperatures (Fig. 4.5c) where the only modified simulation parameter is the measured temperature of the cryostat. Reduced asymmetry in cavity-coupled PL at elevated temperatures is due to the reduced asymmetry of the phonon-mediated exciton-cavity coupling rates with respect to the
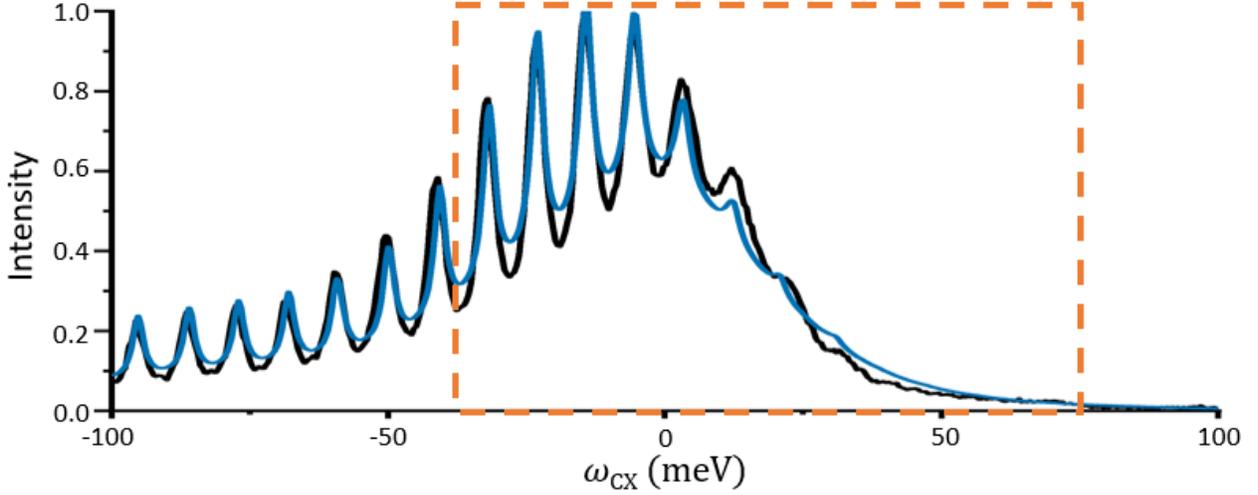
Figure 4.4: **Theoretical fit of a polaron model to cavity-coupled photoluminescence data.** Measured cavity-coupled PL (black) and simulated cavity-coupled PL (blue) at 80 K. Theoretical model fit to the windowed region of data with the Hamiltonian described in the text ($T = 80$ K, $\gamma = 48.4$ meV, $\alpha_p = 0.018$ ps^2, $\omega_b = 6.7$ meV, $\kappa = 2.85$ meV, $g = 4$ meV).

neutral exciton resonance.

4.4.1 Numerical details

The cavity-coupled PL spectrum is found from the Fourier transform of the correlation function

$$S(\omega) = \int_{-\infty}^{\infty} \lim_{t \to \infty} \langle c^\dagger(t + \tau)c(t) \rangle d\tau$$

which is provided as a function in the QuTiP Python library [176]. Although it is tempting to simultaneously include all cavity resonances in the system Hamiltonian, with the cavity bosonic operator truncated at $N = 10$ to ensure convergence a Hilbert space dimension that is classically intractable to simulate quickly overwhelms the computational resources. Instead, each cavity mode of the ring resonator is assumed to be independent because the spatial overlap of different modes is approximately equal to zero. Similarly, only cavity modes which

75
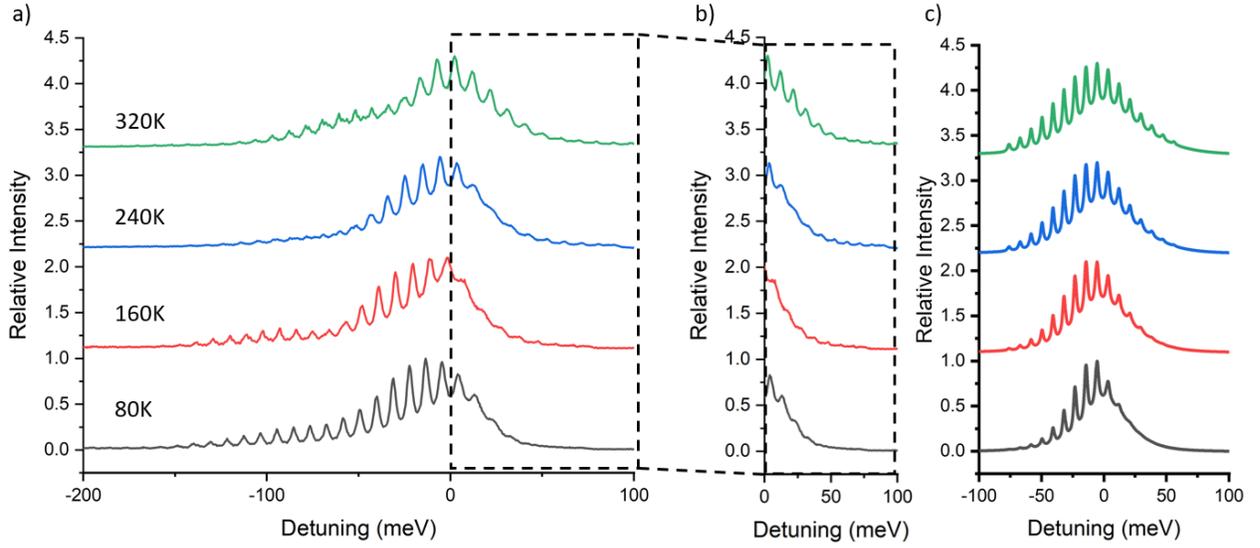
Figure 4.5: **Temperature dependent cavity-coupled photoluminescence data and simulations.** a) Temperature dependence (80 K to 320 K) of the asymmetric cavity-coupled PL. b) Zoomed-in to show the temperature dependence of the asymmetric cavity-coupled PL for cavities blue-detuned with respect to the exciton. c) Simulated temperature dependence of cavity-coupled PL without trion and defect emission. All free parameters are held fixed except the measured cryostat temperature ($T = 80$ K, 160 K, 240 K, 320 K, $\gamma = 48.4$ meV, $\alpha_p = 0.018$ ps^2, $\omega_b = 6.7$ meV, $\kappa = 2.85$ meV, $g = 4$ meV).

have the same spatial wavefunction as the collective excitation of the excitonic resonance [18, 31] are considered. The total spectrum S_{Total} is then a linear superposition of all cavity resonances with different detuning Δ_{CX} coupled to the monolayer PL and background PL

$$S_{Total}(\omega) = f_1 S_{PL}(\omega) + f_2 \sum_{\Delta_{CX}} S_{\Delta_{CX}}(\omega)$$

$$+ f_3 \frac{A_D e^{\frac{-4\ln 2 (\omega - \Delta_D)^2}{\Gamma_D^2}}}{\Gamma_D \sqrt{\frac{\pi}{4\ln 2}}} \sum_{\Delta_{CX}} \frac{2A_{DC}}{\pi} \frac{\Gamma_{DC}}{4(\omega - \Delta_{CX})^2 + \Gamma_{DC}^2}$$

$$+ f_4 \frac{2A_T}{\pi} \frac{\Gamma_T}{4(\omega - \Delta_T)^2 + \Gamma_T^2} \sum_{\Delta_{CX}} \frac{2A_{TC}}{\pi} \frac{\Gamma_{TC}}{4(\omega - \Delta_{CX})^2 + \Gamma_{TC}^2}$$

The free parameters for fitting the model to the cavity-coupled PL data are f_{1-4} as the relative intensity of the background PL, cavity-coupled neutral exciton PL, cavity-coupled defect PL and cavity-coupled trion PL and the exciton-cavity coupling g. The relative intensity in this experiment was found to be $f_1 = 0.53$, $f_2 = 0.44$, $f_3 = 2.18$, and $f_4 = 1.49$. A single cavity parameter for defect and trion emission was chosen to reduce overfitting. For the cavity-coupled defect PL $A_{DC} = 2.24$ and $\Gamma_{DC} = 2.33$ meV. For the cavity-coupled trion PL $A_{TC} = 1.42$ and $\Gamma_{TC} = 2.29$ meV.

4.5 Discussion

The exciton-phonon interactions in cavity-integrated TMDs manifesting as a phenomenological deformation potential has significant value in explaining asymmetric cavity emission [6, 112, 141, 142]. Reflecting on the effective system Hamiltonian (Eq. 4.7), the polaron shift $\hbar \Delta_P = 24$ meV of the exciton energy is comparable to the $\hbar \Delta_P = 29$ meV found via the excitonic Bloch equations [137]. Temperature dependence of the exciton-cavity coupling has been previously observed in strong-coupling experiments with TMD excitons [23, 26, 27], although a rigorous model explaining this behavior was not reported. The modification of the bare value is attributed to the average phonon displacement $g \to \langle B \rangle g$. A consequence of the exciton-cavity incoherent scattering (Eq. 4.20) is an efficient means for exciton population inversion which could potentially explain observations of lasing in cavity-integrated monolayer

materials [5, 6, 36, 141, 147, 177]. In the interest of a low-power optical non-linearity, polaron-polaron scattering in the effective system Hamiltonain ($\Delta_P b^\dagger b^\dagger bb$) provides an interesting opportunity which could lead to non-classical light generation [150]. The calculated polaron shift is two orders of magnitude larger than expected for the exciton-exciton interaction due to a lateral confining potential [20]. The investigation of the exciton-phonon interaction in a quantum optical model for this material system demonstrates the need to fully consider all many-body interactions to assess the potential for future classical and quantum technologies.

Chapter 5

OUTLOOK

The potential advantage of cavity quantum electrodynamics (cQED) [17, 64] with dielectric microresonators for ultra-low power integrated nonlinear optics stems from the wavelength-scale mode volumes ($V_m \sim (\lambda/n)^3$) with moderate quality factors ($Q \sim 1 \times 10^6$) and an inherent scalability using fabrication technologies developed for the microelectronics industry. Compare this to millimeter-scale superconducting cavities with quality factors in excess of $Q \sim 10^{10}$ [17, 178, 179]. The figure of merit Q/V_m for electric field enhancement is orders of magnitude larger for dielectric microresonators. However, due to fabrication imperfections in situ tuning of the quasinormal mode resonant frequency for monolithic dielectric microresonators is necessary, but remains an outstanding problem. Some potential solutions exist such as micro-electro-mechanical displacement of coupled cavities.

Another difficulty of microcavity QED is in choosing an ideal quantum emitter. Color centers, rare-earth ions, quantum dots, and donor qubits all support optical transitions with long-lived internal degrees of freedom, such as electron or nuclear spin sublevels. The stochastic nature of the emitter position precludes a straightforward monolithic fabrication process flow. And, similar to microresonators, due to inhomogeneous broadening the emitter resonant frequency also requires in situ tuning, possibly via the quantum confined Stark effect. The intent of the monolayer transition metal dichalcogenides (TMDs) was for a quantum emitter that can be deterministically integrated into microresonators at the expense of a reduced quantum anharmonicity. This thesis leaves unresolved the possibility for ultra-low power or quantum nonlinear optics in this material system.

5.1 Excitonic optical nonlinearity

5.1.1 Conventional and unconventional photon statisitics

An incontrovertible manifestation of quantum nonlinear optics is a classically forbidden value of the second-order correlation function. The second-order correlation function defined as

$$g^{(2)}(\tau) = \lim_{t\to\infty} \frac{\left\langle \hat{a}^\dagger(t)\left(\hat{a}^\dagger\hat{a}\right)(t+\tau)\hat{a}(t)\right\rangle}{\left[\langle\hat{a}^\dagger\hat{a}\rangle(t)\right]^2} = \frac{\left\langle \hat{a}^\dagger\left(\hat{a}^\dagger\hat{a}\right)(\tau)\hat{a}\right\rangle}{\langle\hat{n}\rangle^2} \tag{5.1}$$

compares the photon arrival times to that of a Poissonian process, such as a laser, where photon arrival times are uncorrelated. Poissonian light sources have $g^{(2)}(\tau) = 1$. Super-Poissonian statistics ($g^{(2)}(\tau) > 1$) exhibits photon bunching and sub-Poissonian statistics ($g^{(2)}(\tau) < 1$) exhibits photon antibunching. Sub-Poissonian statistics cannot be achieved with classical electromagnetic radiation suggesting the measurement of photon statistics as a straightforward test for the quantum nature of a light source.

The general Hamiltonian for polariton blockade in microcavity QED is

$$H = \hbar\Delta_{CL}\hat{a}^\dagger\hat{a} + \hbar\Delta_{XL}\hat{b}^\dagger\hat{b} + \hbar g(\hat{b}^\dagger\hat{a} + \hat{b}\hat{a}^\dagger)$$
$$+ i\hbar\sqrt{\gamma_1}(\alpha\hat{a}^\dagger + \alpha^*\hat{a}) + \frac{U}{2}\hat{b}^\dagger\hat{b}^\dagger\hat{b}\hat{b}. \tag{5.2}$$

The first line is the coupled oscillator Hamiltonian of Eq. (3.29). The second line describes the resonant drive of the photonic mode and a Kerr-type nonlinearity ($\frac{U}{2}$) of the excitonic mode due to exciton-exciton interactions. γ_1 is the input coupling to the cavity and $|\alpha|^2$ is the incident photon flux for a coherent, classical cavity drive. There exist two regimes of non-classical photon statistics for Hamiltonians of this type known as conventional and unconventional, both of which can be described by the mixing of a squeezed and coherent state [180]. Conventional polariton blockade arises when a single photon, resonant to the polariton, excites the material system, but any subsequent photon is detuned from the polariton due to the nonlinearity. Unconventional polariton blockade arises from the destructive interference between two paths to the two-photon excited state [181].

5.1.2 Exciton-exciton interaction

In establishing the exciton-photon interaction and exciton-phonon interaction the excitonic annihilation operator was assumed to satisfy bosonic commutation relations. The exciton Hamiltonian can be extended to include a Kerr-type optical nonlinearity [49]

$$\hat{H}_{\mathrm{x}} = \sum_{\alpha\mathbf{k}} \hbar\omega_{\mathbf{k}} \hat{b}^\dagger_{\alpha\mathbf{k}} \hat{b}_{\alpha\mathbf{k}} + \sum_{\alpha\mathbf{kk'q}} \hbar W_{\mathbf{kk'q}} \hat{b}^\dagger_{\alpha\mathbf{k}+\mathbf{q}} \hat{b}^\dagger_{\alpha\mathbf{k'}-\mathbf{q}} \hat{b}_{\alpha\mathbf{k'}} \hat{b}_{\alpha\mathbf{k}}. \tag{5.3}$$

The first term is the exciton kinetic energy of the bosonic exciton creation operator. The second term is a two body exciton-exciton interaction which is the lowest-order correction to account for the fermionic electron and hole constituents of the composite boson. Within the exciton reaction coordinate the exciton-exciton interaction is

$$\hat{W}_0 = \hbar W'_0 \hat{B}^\dagger_0 \hat{B}^\dagger_0 \hat{B}_0 \hat{B}_0 \tag{5.4}$$

where $W'_0 = \sum_{\alpha\mathbf{kk'q}} W_{\mathbf{kk'q}} U_{0\alpha\mathbf{k}+\mathbf{q}} U_{0\alpha\mathbf{k'}-\mathbf{q}} U^*_{0\alpha\mathbf{k'}} U^*_{0\alpha\mathbf{k}}$ ($U_{0\alpha\mathbf{k}}$ is defined in chapter 3). Note the position space exciton creation operator is $b^\dagger_\alpha(\mathbf{r}) = S^{-1/2} \sum_{\mathbf{k}} e^{-i\mathbf{k}\cdot\mathbf{r}} b^\dagger_{\alpha\mathbf{k}}$. And the position space exciton reaction coordinate creation operator is $B^\dagger_0 = \sum_\alpha \int \mathrm{d}^2\mathbf{r}\, \psi^\alpha_0(\mathbf{r}) b^\dagger_\alpha(\mathbf{r})$. The position space exciton reaction coordinate wave function is

$$\psi^\alpha_0(\mathbf{r}) = -\frac{\tilde{\mathbf{f}}_c(\mathbf{r}, z_0) \cdot \mathbf{p}^\alpha_{\mathrm{cv}}}{\sqrt{\left|\sum_{\alpha'} \int \mathrm{d}^2\mathbf{r}'\, \tilde{\mathbf{f}}_c(\mathbf{r}', z_0) \cdot \mathbf{p}^{\alpha'}_{cv}\right|^2}} \tag{5.5}$$

For dielectric microresonators the quasinormal mode confining length scale is much larger than the exciton Bohr radius. Then $W_{\mathbf{kk'q}} \simeq W_{000}$ is approximately constant over similar momentum variations as $U_{0\alpha\mathbf{k}}$. The exciton-exciton interaction strength can then be written as

$$W'_0 = S W_{000} \sum_\alpha \int \mathrm{d}^2\mathbf{r}\, |\psi^\alpha_0(\mathbf{r})|^4 \tag{5.6}$$

justifying the standard assumption in confined exciton-polariton systems that there exists an excitonic mode commensurate with the cavity mode [18]. The integral in Eq. (5.6) can be written in terms of the QNM field profile as

$$W_0' = SW_{000} \frac{\int \mathrm{d}^2\mathbf{r} \left| \tilde{\mathbf{f}}_C \left(\mathbf{r}, z_0\right) \right|^4}{\left(\int \mathrm{d}^2\mathbf{r} \left| \tilde{\mathbf{f}}_C \left(\mathbf{r}, z_0\right) \right|^2 \right)^2} \tag{5.7}$$

The bare exciton-exciton interaction is of the order $W_{000} \simeq E_b a_B^2 / S$ [182]. For monolayer MoSe$_2$ the exciton binding energy is $E_b = 0.5$ eV and the exciton Bohr radius is $a_B = 2.6$ nm [49]. For the photonic crystal defect resonator in chapter 3 the confinement-enhanced exciton-exciton interaction is $\frac{U}{2} = W_0' \sim 0.1$ μeV ($2\pi \times 25$ GHz).

Assuming optimal experimental parameters for the exciton-resonator system an a priori estimate can be made for the second-order correlation function at zero time delay (Fig. 5.1). The figure of merit for observing polariton blockade is U/γ_X [180]. For $U/\gamma_X = 10^{-4}$ a minimum $g^{(2)}(0) = 0.97$ is similar to that seen in other polariton systems [30, 31] but is difficult to discern from experimental noise. An encouraging prospect is the exciton dressed by phonons, the exciton-polaron, discussed in chapter 4 leads to a larger effective Bohr radius with the polaron-polaron interaction $\hbar\Delta_\rho = \hbar \int_0^\infty d\omega J(\omega)/\omega = \hbar\sqrt{\frac{\pi}{2}} a_p \omega_b^3$. For an order of magnitude improvement with $U/\gamma_X = 10^{-3}$ a minimum $g^{(2)}(0) = 0.73$ is found and with $U/\gamma_X = 10^{-2}$ a minimum $g^{(2)}(0) = 0.05$ is found. Unconventional blockade was explored for this system in Ryou et al. [20] although the model can be improved with our better understanding of the light-matter interaction and confinement effects on the excitonic transition [89].

5.2 Conclusion

In this thesis I established a deterministic and clean method to incorporate micron-scale two-dimensional semiconductors onto integrated photonic devices. I established theoretical and experimental estimates of the light-matter interaction strength for two-dimensional
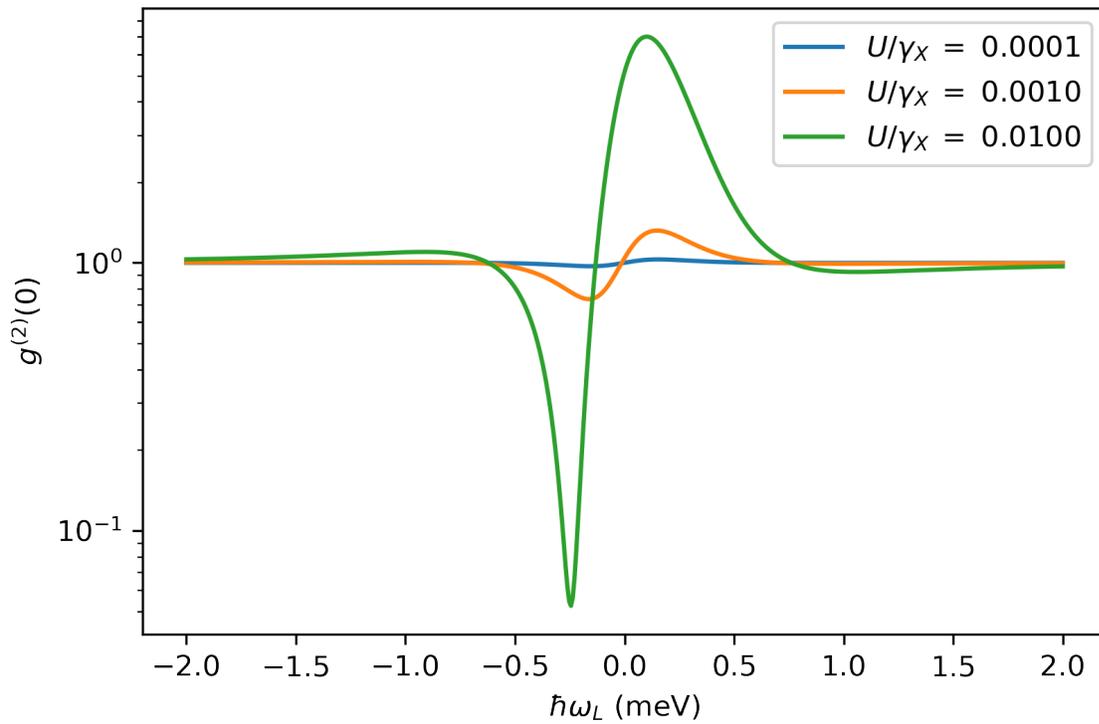
Figure 5.1: **$\mathbf{g^{(2)}(0)}$ versus the driving laser frequency $\omega_{\mathbf{L}}$ relative to the cavity frequency for various $\mathbf{U}/\gamma_{\mathbf{X}}$.** Parameters: $\hbar(\kappa + \gamma) = 0.01$ meV, $\gamma_X = 100(\kappa + \gamma)$, $\hbar g = 5.1$ meV, $\hbar\sqrt{\gamma_1}\alpha = 0.001$ meV.

excitons in monolayer MoSe$_2$ coupled to a nanobeam cavity. And I established limitations of the experimental system due to cavity design and phonon-mediated loss channels.

I also established the confinement-enhanced exciton-exciton interaction and expectations for polariton blockade. The prospects must be re-evaluated for observation with a side-coupled cavity where the input-ouput geometry determines the optimal design [183], such as with a bimodal cavity that allows for multiple driving lasers to engineer the photonic environment [184, 185]. There also exists an anharmonic exciton-photon coupling

$$\hat{W}_{\mathrm{EM}} = \sum_{\alpha \mathbf{k}_1 \mathbf{k}_2 \mathbf{k}_3} \hbar \sigma_{\alpha \mathbf{k}_1 \mathbf{k}_2 \mathbf{k}_3} \left(\hat{b}^\dagger_{\alpha \mathbf{k}_1} \hat{b}_{\alpha \mathbf{k}_2} \hat{b}_{\alpha \mathbf{k}_3} + \text{ H.c. } \right) \left(\hat{a}^\dagger_{\mathrm{c}} + \hat{a}_{\mathrm{c}} \right) \tag{5.8}$$

that leads to saturation of the excitonic oscillator strength [186, 187]. Preliminary results with a far-detuned cavity suggest excitonic optical bistability might be a more straightforward means to observe an optical nonlinearity in this system [188].

The biggest difficulty in observing non-classical photon statistics in this material system is the weak anharmonicity of the excitonic Hamiltonian. Hetero-bilayer structures of two-dimensional materials are a natural next step of my research that hope to avoid this limitation. Hetero-bilayers support interlayer excitons with large out-of-plane dipole moments. Using the methods outlined in chapter 3 it should be possible to ascertain if the light-matter interaction strength is sufficient to form dipolar-polariton modes [189, 190]. The cavities would require a transverse magnetic (TM) mode, instead of the earlier transverse electric (TE) mode, to maximize coupling to the interlayer exciton. The advantage to the hetero-bilayer is the dipolar-dipolar interaction which is ≈ 1 meV [191], four orders of magnitude larger than that of the monolayer. The ancillary benefit is the out-of-plane dipole moment aligns with the out-of-plane electric field used in electrostatic gating of the optical transition to demonstrate the quantum confined Stark effect. This affords a larger tuning effect on the excitonic resonance frequency useful for in situ control of the quantum device.

The material system described in this thesis, a two-dimensional optical transition coupled to a dielectric microresonator, attempts to circumvent the obstacles of zero-dimensional

optical transitions (e.g. color centers, quantum dots, etc.) such as their stochastic position and wavelength. However, two-dimensional excitonic transitions come at the expense of a large linewidth, sensitivity to the atomic smoothness of the dielectric environment, and weak excitonic anharmonicity. Fortunately, all these limitations have straightforward engineering solutions lending to promising prospects for integrated nonlinear optics using dipolar-polaritons in dielectric microresonators.

BIBLIOGRAPHY

[1]Y. Liu, N. O. Weiss, X. Duan, H.-C. Cheng, Y. Huang, and X. Duan, "Van der Waals heterostructures and devices", Nature Reviews Materials **1**, 1–17 (2016).

[2]C.-h. Liu, J. Zheng, Y. Chen, T. Fryett, and A. Majumdar, "Van der Waals materials integrated nanophotonic devices [Invited]", Optical Materials Express **9**, 384–399 (2019).

[3]F. Xia, H. Wang, D. Xiao, M. Dubey, and A. Ramasubramaniam, "Two-dimensional material nanophotonics", Nature Photonics **8**, 899–907 (2014).

[4]T. Fryett, A. Zhan, and A. Majumdar, "Cavity nonlinear optics with layered materials", Nanophotonics **7**, 355–370 (2018).

[5]S. Wu, S. Buckley, J. R. Schaibley, L. Feng, J. Yan, D. G. Mandrus, F. Hatami, W. Yao, J. Vučković, A. Majumdar, and X. Xu, "Monolayer semiconductor nanocavity lasers with ultralow thresholds", Nature **520**, 69–72 (2015).

[6]Y. Ye, Z. J. Wong, X. Lu, X. Ni, H. Zhu, X. Chen, Y. Wang, and X. Zhang, "Monolayer excitonic laser", Nature Photonics **9**, 733–737 (2015).

[7]C. T. Phare, Y.-H. Daniel Lee, J. Cardenas, and M. Lipson, "Graphene electro-optic modulator with 30 GHz bandwidth", Nature Photonics **9**, 511–514 (2015).

[8]N. Youngblood, C. Chen, S. J. Koester, and M. Li, "Waveguide-integrated black phosphorus photodetector with high responsivity and low dark current", Nature Photonics **9**, 247–252 (2015).

[9]D. E. Chang, A. S. Sørensen, E. A. Demler, and M. D. Lukin, "A single-photon transistor using nanoscale surface plasmons", Nature Physics **3**, 807–812 (2007).

[10] D. Englund, A. Majumdar, M. Bajcsy, A. Faraon, P. Petroff, and J. Vučković, "Ultrafast Photon-Photon Interaction in a Strongly Coupled Quantum Dot-Cavity System", Physical Review Letters **108**, 093604 (2012).

[11] D. A. B. Miller, "Attojoule Optoelectronics for Low-Energy Information Processing and Communications", Journal of Lightwave Technology **35**, 346–396 (2017).

[12] S. Sun, H. Kim, Z. Luo, G. S. Solomon, and E. Waks, "A single-photon switch and transistor enabled by a solid-state quantum memory", Science **361**, 57–60 (2018).

[13] P. Kok and B. W. Lovett, *Introduction to Optical Quantum Information Processing* (Cambridge University Press, Cambridge, 2010).

[14] L. Chrostowski and M. Hochberg, *Silicon Photonics Design: From Devices to Systems* (Cambridge University Press, Cambridge, 2015).

[15] R. W. Boyd, *Nonlinear Optics* (Academic Press, Mar. 2020).

[16] G. Agrawal, *Applications of Nonlinear Fiber Optics* (Academic Press, Aug. 2020).

[17] S. Haroche and J.-M. Raimond, *Exploring the Quantum: Atoms, Cavities, and Photons*, Oxford Graduate Texts (Oxford University Press, Oxford, 2006).

[18] A. Verger, C. Ciuti, and I. Carusotto, "Polariton quantum blockade in a photonic dot", Physical Review B **73**, 193306 (2006).

[19] V. Walther, R. Johne, and T. Pohl, "Giant optical nonlinearities from Rydberg excitons in semiconductor microcavities", Nature Communications **9**, 1309 (2018).

[20] A. Ryou, D. Rosser, A. Saxena, T. Fryett, and A. Majumdar, "Strong photon antibunching in weakly nonlinear two-dimensional exciton-polaritons", Physical Review B **97**, 235307 (2018).

[21] X. Liu, T. Galfsky, Z. Sun, F. Xia, E.-c. Lin, Y.-H. Lee, S. Kéna-Cohen, and V. M. Menon, "Strong light–matter coupling in two-dimensional atomic crystals", Nature Photonics **9**, 30–34 (2015).

[22] S. Dufferwiel, S. Schwarz, F. Withers, A. a. P. Trichet, F. Li, M. Sich, O. Del Pozo-Zamudio, C. Clark, A. Nalitov, D. D. Solnyshkov, G. Malpuech, K. S. Novoselov, J. M. Smith, M. S. Skolnick, D. N. Krizhanovskii, and A. I. Tartakovskii, "Exciton–polaritons in van der Waals heterostructures embedded in tunable microcavities", Nature Communications **6**, 8579 (2015).

[23] X. Liu, W. Bao, Q. Li, C. Ropp, Y. Wang, and X. Zhang, "Control of Coherently Coupled Exciton Polaritons in Monolayer Tungsten Disulphide", Physical Review Letters **119**, 027403 (2017).

[24] C. Schneider, M. M. Glazov, T. Korn, S. Höfling, and B. Urbaszek, "Two-dimensional semiconductors in the regime of strong light-matter coupling", Nature Communications **9**, 2695 (2018).

[25] Y. Chen, S. Miao, T. Wang, D. Zhong, A. Saxena, C. Chow, J. Whitehead, D. Gerace, X. Xu, S.-F. Shi, and A. Majumdar, "Metasurface Integrated Monolayer Exciton Polariton", Nano Letters **20**, 5292–5300 (2020).

[26] L. Zhang, R. Gogna, W. Burg, E. Tutuc, and H. Deng, "Photonic-crystal exciton-polaritons in monolayer semiconductors", Nature Communications **9**, 713 (2018).

[27] V. Kravtsov, E. Khestanova, F. A. Benimetskiy, T. Ivanova, A. K. Samusev, I. S. Sinev, D. Pidgayko, A. M. Mozharov, I. S. Mukhin, M. S. Lozhkin, Y. V. Kapitonov, A. S. Brichkin, V. D. Kulakovskii, I. A. Shelykh, A. I. Tartakovskii, P. M. Walker, M. S. Skolnick, D. N. Krizhanovskii, and I. V. Iorsh, "Nonlinear polaritons in a monolayer semiconductor coupled to optical bound states in the continuum", Light: Science & Applications **9**, 56 (2020).

[28] M. Sidler, P. Back, O. Cotlet, A. Srivastava, T. Fink, M. Kroner, E. Demler, and A. Imamoglu, "Fermi polaron-polaritons in charge-tunable atomically thin semiconductors", Nature Physics **13**, 255–261 (2017).

[29]C. Gebhardt, M. Förg, H. Yamaguchi, I. Bilgin, A. D. Mohite, C. Gies, M. Florian, M. Hartmann, T. W. Hänsch, A. Högele, and D. Hunger, "Polariton hyperspectral imaging of two-dimensional semiconductor crystals", Scientific Reports **9**, 13756 (2019).

[30]A. Delteil, T. Fink, A. Schade, S. Höfling, C. Schneider, and A. İmamoğlu, "Towards polariton blockade of confined exciton–polaritons", Nature Materials **18**, 219–222 (2019).

[31]G. Muñoz-Matutano, A. Wood, M. Johnsson, X. Vidal, B. Q. Baragiola, A. Reinhard, A. Lemaître, J. Bloch, A. Amo, G. Nogues, B. Besga, M. Richard, and T. Volz, "Emergence of quantum correlations from interacting fibre-cavity polaritons", Nature Materials **18**, 213–218 (2019).

[32]D. Gerace, F. Laussy, and D. Sanvitto, "Quantum nonlinearities at the single-particle level", Nature Materials **18**, 200–201 (2019).

[33]B. Besga, C. Vaneph, J. Reichel, J. Estève, A. Reinhard, J. Miguel-Sánchez, A. Imamoğlu, and T. Volz, "Polariton Boxes in a Tunable Fiber Cavity", Physical Review Applied **3**, 014008 (2015).

[34]T. K. Fryett, Y. Chen, J. Whitehead, Z. M. Peycke, X. Xu, X. Xu, A. Majumdar, and A. Majumdar, "Encapsulated Silicon Nitride Nanobeam Cavity for Nanophotonics using Layered Materials", in Conference on Lasers and Electro-Optics (2018), paper JW2A.16 (May 2018), JW2A.16.

[35]A. Majumdar, A. Rundquist, M. Bajcsy, V. D. Dasika, S. R. Bank, and J. Vučković, "Design and analysis of photonic crystal coupled cavity arrays for quantum simulation", Physical Review B **86**, 195312 (2012).

[36]Y. Li, J. Zhang, D. Huang, H. Sun, F. Fan, J. Feng, Z. Wang, and C. Z. Ning, "Room-temperature continuous-wave lasing from monolayer molybdenum ditelluride integrated with a silicon nanobeam cavity", Nature Nanotechnology **12**, 987–992 (2017).

[37]C.-H. Liu, G. Clark, T. Fryett, S. Wu, J. Zheng, F. Hatami, X. Xu, and A. Majumdar, "Nanocavity Integrated van der Waals Heterostructure Light-Emitting Tunneling Diode", Nano Letters **17**, 200–205 (2017).

[38]T. K. Fryett, K. L. Seyler, J. Zheng, C.-H. Liu, X. Xu, and A. Majumdar, "Silicon photonic crystal cavity enhanced second-harmonic generation from monolayer WSe 2", 2D Materials **4**, 015031 (2016).

[39]X.-T. Gan, C.-Y. Zhao, S.-Q. Hu, T. Wang, Y. Song, J. Li, Q.-H. Zhao, W.-Q. Jie, and J.-L. Zhao, "Microwatts continuous-wave pumped second harmonic generation in few- and mono-layer GaSe", Light: Science & Applications **7**, 17126–17126 (2018).

[40]P. Rivera, T. K. Fryett, Y. Chen, C.-H. Liu, E. Ray, F. Hatami, J. Yan, D. Mandrus, W. Yao, A. Majumdar, and X. Xu, "Coupling of photonic crystal cavity and interlayer exciton in heterobilayer of transition metal dichalcogenides", 2D Materials **7**, 015027 (2019).

[41]Y. Liu, H. Fang, A. Rasmita, Y. Zhou, J. Li, T. Yu, Q. Xiong, N. Zheludev, J. Liu, and W. Gao, "Room temperature nanocavity laser with interlayer excitons in 2D heterostructures", Science Advances **5**, eaav4506 (2019).

[42]A. Faraon, I. Fushman, D. Englund, N. Stoltz, P. Petroff, and J. Vučković, "Coherent generation of non-classical light on a chip via photon-induced tunnelling and blockade", Nature Physics **4**, 859–863 (2008).

[43]A. Majumdar, M. Bajcsy, and J. Vučković, "Probing the ladder of dressed states and nonclassical light generation in quantum-dot–cavity QED", Physical Review A **85**, 041801 (2012).

[44]A. Reinhard, T. Volz, M. Winger, A. Badolato, K. J. Hennessy, E. L. Hu, and A. Imamoğlu, "Strongly correlated photons on a chip", Nature Photonics **6**, 93–96 (2012).

[45]D. Najer, I. Söllner, P. Sekatski, V. Dolique, M. C. Löbl, D. Riedel, R. Schott, S. Starosielec, S. R. Valentin, A. D. Wieck, N. Sangouard, A. Ludwig, and R. J. Warburton, "A gated quantum dot strongly coupled to an optical microcavity", Nature **575**, 622–627 (2019).

[46]M. Notomi, "Manipulating light with strongly modulated photonic crystals", Reports on Progress in Physics **73**, 096501 (2010).

[47]D. Hunger, T. Steinmetz, Y. Colombe, C. Deutsch, T. W. Hänsch, and J. Reichel, "A fiber Fabry–Perot cavity with high finesse", New Journal of Physics **12**, 065038 (2010).

[48]K. Hennessy, A. Badolato, M. Winger, D. Gerace, M. Atatüre, S. Gulde, S. Fält, E. L. Hu, and A. Imamoğlu, "Quantum nature of a strongly coupled single quantum dot–cavity system", Nature **445**, 896–899 (2007).

[49]E. V. Denning, M. Wubs, N. Stenger, J. Mork, and P. T. Kristensen, "Quantum theory of two-dimensional materials coupled to electromagnetic resonators", arXiv:2103.14488 [cond-mat, physics:quant-ph] (2021).

[50]D. Gerace, H. E. Türeci, A. Imamoglu, V. Giovannetti, and R. Fazio, "The quantum-optical Josephson interferometer", Nature Physics **5**, 281–284 (2009).

[51]T. C. H. Liew and V. Savona, "Single Photons from Coupled Quantum Modes", Physical Review Letters **104**, 183601 (2010).

[52]S. Ferretti and D. Gerace, "Single-photon nonlinear optics with Kerr-type nanostructured materials", Physical Review B **85**, 033303 (2012).

[53]K. Kim, M. Yankowitz, B. Fallahazad, S. Kang, H. C. P. Movva, S. Huang, S. Larentis, C. M. Corbet, T. Taniguchi, K. Watanabe, S. K. Banerjee, B. J. LeRoy, and E. Tutuc, "Van der Waals Heterostructures with High Accuracy Rotational Alignment", Nano Letters **16**, 1989–1995 (2016).

[54]T. Chen, H. Lee, and K. J. Vahala, "Design and characterization of whispering-gallery spiral waveguides", Optics Express **22**, 5196–5208 (2014).

[55]W. Bogaerts, P. De Heyn, T. Van Vaerenbergh, K. De Vos, S. Kumar Selvaraja, T. Claes, P. Dumon, P. Bienstman, D. Van Thourhout, and R. Baets, "Silicon microring resonators", Laser & Photonics Reviews **6**, 47–73 (2012).

[56]P. Lalanne, W. Yan, K. Vynck, C. Sauvan, and J.-P. Hugonin, "Light Interaction with Photonic and Plasmonic Resonances", Laser & Photonics Reviews **12**, 1700113 (2018).

[57]P. T. Kristensen, K. Herrmann, F. Intravaia, K. Busch, and K. Busch, "Modeling electromagnetic resonators using quasinormal modes", Advances in Optics and Photonics **12**, 612–708 (2020).

[58]C. Sauvan, J. P. Hugonin, I. S. Maksymov, and P. Lalanne, "Theory of the Spontaneous Optical Emission of Nanosize Photonic and Plasmon Resonators", Physical Review Letters **110**, 237401 (2013).

[59]P. T. Kristensen and S. Hughes, "Modes and Mode Volumes of Leaky Optical Cavities and Plasmonic Nanoresonators", ACS Photonics **1**, 2–10 (2014).

[60]P. Yao, V. Manga Rao, and S. Hughes, "On-chip single photon sources using planar photonic crystals and single quantum dots", Laser & Photonics Reviews **4**, 499–516 (2010).

[61]P. T. Kristensen, C. V. Vlack, and S. Hughes, "Generalized effective mode volume for leaky optical cavities", Optics Letters **37**, 1649–1651 (2012).

[62]M. Kamandar Dezfouli and S. Hughes, "Regularized quasinormal modes for plasmonic resonators and open cavities", Physical Review B **97**, 115302 (2018).

[63]A. Zangwill, *Modern Electrodynamics* (Cambridge University Press, Cambridge, 2012).

[64]A. V. Kavokin, J. J. Baumberg, G. Malpuech, and F. P. Laussy, *Microcavities*, Second Edition, New to this Edition: Series on Semiconductor Science and Technology (Oxford University Press, Oxford, New York, July 2017).

[65]S. L. Chuang, *Physics of Photonic Devices*, 2nd edition (Wiley, Hoboken, N.J, Jan. 2009).

[66]Q. Quan, P. B. Deotare, and M. Loncar, "Photonic crystal nanobeam cavity strongly coupled to the feeding waveguide", Applied Physics Letters **96**, 203102 (2010).

[67]Q. Quan and M. Loncar, "Deterministic design of wavelength scale, ultra-high Q photonic crystal nanobeam cavities", Optics Express **19**, 18529–18542 (2011).

[68]M. J. Collett and C. W. Gardiner, "Squeezing of intracavity and traveling-wave light fields produced in parametric amplification", Physical Review A **30**, 1386–1391 (1984).

[69]C. W. Gardiner and M. J. Collett, "Input and output in damped quantum systems: Quantum stochastic differential equations and the master equation", Physical Review A **31**, 3761–3774 (1985).

[70]Y. Xu, Y. Li, R. K. Lee, and A. Yariv, "Scattering-theory analysis of waveguide-resonator coupling", Physical Review E **62**, 7389–7404 (2000).

[71]S. Fan, Ş. E. Kocabaş, and J.-T. Shen, "Input-output formalism for few-photon transport in one-dimensional nanophotonic waveguides coupled to a qubit", Physical Review A **82**, 063821 (2010).

[72]E. Rephaeli and S. Fan, "Few-Photon Single-Atom Cavity QED With Input-Output Formalism in Fock Space", IEEE Journal of Selected Topics in Quantum Electronics **18**, 1754–1762 (2012).

[73]K. Srinivasan and O. Painter, "Mode coupling and cavity–quantum-dot interactions in a fiber-coupled microdisk cavity", Physical Review A **75**, 023814 (2007).

[74]M. Combescot and S.-Y. Shiau, *Excitons and Cooper Pairs: Two Composite Bosons in Many-Body Physics*, Oxford Graduate Texts (Oxford University Press, Oxford, 2015).

[75]H. Haug and S. W. Koch, *Quantum Theory of the Optical and Electronic Properties of Semiconductors*, 5th ed. (WORLD SCIENTIFIC, Jan. 2009).

[76]G. Wang, A. Chernikov, M. M. Glazov, T. F. Heinz, X. Marie, T. Amand, and B. Urbaszek, "Colloquium: Excitons in atomically thin transition metal dichalcogenides", Reviews of Modern Physics **90**, 021001 (2018).

[77]A. Chernikov, T. C. Berkelbach, H. M. Hill, A. Rigosi, Y. Li, O. B. Aslan, D. R. Reichman, M. S. Hybertsen, and T. F. Heinz, "Exciton Binding Energy and Nonhydrogenic Rydberg Series in Monolayer ${\mathrm{WS}}_{2}$", Physical Review Letters **113**, 076802 (2014).

[78]T. Olsen, S. Latini, F. Rasmussen, and K. S. Thygesen, "Simple Screened Hydrogen Model of Excitons in Two-Dimensional Materials", Physical Review Letters **116**, 056401 (2016).

[79]D. Van Tuan, M. Yang, and H. Dery, "Coulomb interaction in monolayer transition-metal dichalcogenides", Physical Review B **98**, 125308 (2018).

[80]M. R. Molas, C. Faugeras, A. O. Slobodeniuk, K. Nogajewski, M. Bartos, D. M. Basko, and M. Potemski, "Brightening of dark excitons in monolayers of semiconducting transition metal dichalcogenides", 2D Materials **4**, 021003 (2017).

[81]C. Tan, X. Cao, X.-J. Wu, Q. He, J. Yang, X. Zhang, J. Chen, W. Zhao, S. Han, G.-H. Nam, M. Sindoro, and H. Zhang, "Recent Advances in Ultrathin Two-Dimensional Nanomaterials", Chemical Reviews **117**, 6225–6331 (2017).

[82]Z. Cai, B. Liu, X. Zou, and H.-M. Cheng, "Chemical Vapor Deposition Growth and Applications of Two-Dimensional Materials and Their Heterostructures", Chemical Reviews **118**, 6091–6133 (2018).

[83]L. Wang, I. Meric, P. Y. Huang, Q. Gao, Y. Gao, H. Tran, T. Taniguchi, K. Watanabe, L. M. Campos, D. A. Muller, J. Guo, P. Kim, J. Hone, K. L. Shepard, and C. R. Dean, "One-Dimensional Electrical Contact to a Two-Dimensional Material", Science **342**, 614–617 (2013).

[84]R. A. Hemnani, J. P. Tischler, C. Carfano, R. Maiti, M. H. Tahersima, L. Bartels, R. Agarwal, and V. J. Sorger, "2D material printer: a deterministic cross contamination-free transfer method for atomically layered materials", 2D Materials **6**, 015006 (2018).

[85]H. Lee, T. Chen, J. Li, O. Painter, and K. J. Vahala, "Ultra-low-loss optical delay line on a silicon chip", Nature Communications **3**, 867 (2012).

[86]P. Tonndorf, R. Schmidt, P. Böttger, X. Zhang, J. Börner, A. Liebig, M. Albrecht, C. Kloc, O. Gordan, D. R. T. Zahn, S. M. d. Vasconcellos, and R. Bratschitsch, "Photoluminescence emission and Raman response of monolayer MoS_2, $MoSe_2$, and WSe_2", Optics Express **21**, 4908–4916 (2013).

[87] P. K. Chow, R. B. Jacobs-Gedrim, J. Gao, T.-M. Lu, B. Yu, H. Terrones, and N. Koratkar, "Defect-Induced Photoluminescence in Monolayer Semiconducting Transition Metal Dichalcogenides", ACS Nano **9**, 1520–1527 (2015).

[88] H. Kroemer, "Speculations about future directions", Journal of Crystal Growth, Proceedings of the Twelfth International Conference on Molecular Beam Epitaxy **251**, 17–22 (2003).

[89] G. Wei, D. A. Czaplewski, E. J. Lenferink, T. K. Stanev, I. W. Jung, and N. P. Stern, "Size-tunable Lateral Confinement in Monolayer Semiconductors", Scientific Reports **7**, 3324 (2017).

[90] Y. Shen, N. C. Harris, S. Skirlo, M. Prabhu, T. Baehr-Jones, M. Hochberg, X. Sun, S. Zhao, H. Larochelle, D. Englund, and M. Soljačić, "Deep learning with coherent nanophotonic circuits", Nature Photonics **11**, 441–446 (2017).

[91] T. F. d. Lima, H.-T. Peng, A. N. Tait, M. A. Nahmias, H. B. Miller, B. J. Shastri, and P. R. Prucnal, "Machine Learning With Neuromorphic Photonics", Journal of Lightwave Technology **37**, 1515–1534 (2019).

[92] J.-H. Jiang and S. John, "Photonic Architectures for Equilibrium High-Temperature Bose-Einstein Condensation in Dichalcogenide Monolayers", Scientific Reports **4**, 7432 (2014).

[93] H.-X. Wang, A. Zhan, Y.-D. Xu, H.-Y. Chen, W.-L. You, A. Majumdar, and J.-H. Jiang, "Quantum many-body simulation using monolayer exciton-polaritons in coupled-cavities", Journal of Physics: Condensed Matter **29**, 445703 (2017).

[94] Y. Chen, J. Whitehead, A. Ryou, J. Zheng, P. Xu, T. Fryett, and A. Majumdar, "Large thermal tuning of a polymer-embedded silicon nitride nanobeam cavity", Optics Letters **44**, 3058–3061 (2019).

[95] D. Rosser, T. Fryett, A. Ryou, A. Saxena, and A. Majumdar, "Exciton–phonon interactions in nanocavity-integrated monolayer transition metal dichalcogenides", npj 2D Materials and Applications **4**, 1–6 (2020).

[96] D. Rosser, D. Gerace, L. C. Andreani, and A. Majumdar, "Optimal condition to probe strong coupling of two-dimensional excitons and zero-dimensional cavity modes", arXiv:2107.00078 [cond-mat, physics:physics] (2021).

[97] D. Rosser, D. Gerace, Y. Chen, Y. Liu, J. Whitehead, A. Ryou, L. C. Andreani, and A. Majumdar, "Dispersive coupling between MoSe2 and a zero-dimensional integrated nanocavity", arXiv:2010.05458 [physics, physics:quant-ph] (2020).

[98] H. T. Dung, L. Knöll, and D.-G. Welsch, "Three-dimensional quantization of the electromagnetic field in dispersive and absorbing inhomogeneous dielectrics", Physical Review A **57**, 3931–3942 (1998).

[99] S. Franke, S. Hughes, M. K. Dezfouli, P. T. Kristensen, K. Busch, A. Knorr, and M. Richter, "Quantization of Quasinormal Modes for Open Cavities and Plasmonic Cavity Quantum Electrodynamics", Physical Review Letters **122**, 213901 (2019).

[100] S. Hughes, S. Franke, C. Gustin, M. Kamandar Dezfouli, A. Knorr, and M. Richter, "Theory and Limits of On-Demand Single-Photon Sources Using Plasmonic Resonators: A Quantized Quasinormal Mode Approach", ACS Photonics **6**, 2168–2180 (2019).

[101] S. Franke, M. Richter, J. Ren, A. Knorr, and S. Hughes, "Quantized quasinormal-mode description of nonlinear cavity-QED effects from coupled resonators with a Fano-like resonance", Physical Review Research **2**, 033456 (2020).

[102] S. Shree, M. Semina, C. Robert, B. Han, T. Amand, A. Balocchi, M. Manca, E. Courtade, X. Marie, T. Taniguchi, K. Watanabe, M. M. Glazov, and B. Urbaszek, "Observation of exciton-phonon coupling in ${\mathrm{MoSe}}_{2}$ monolayers", Physical Review B **98**, 035302 (2018).

[103] A. Garg, J. N. Onuchic, and V. Ambegaokar, "Effect of friction on electron transfer in biomolecules", The Journal of Chemical Physics **83**, 4491–4503 (1985).

[104] R. Martinazzo, B. Vacchini, K. H. Hughes, and I. Burghardt, "Communication: Universal Markovian reduction of Brownian particle dynamics", The Journal of Chemical Physics **134**, 011101 (2011).

[105] J. Iles-Smith, N. Lambert, and A. Nazir, "Environmental dynamics, correlations, and the emergence of noncanonical equilibrium states in open quantum systems", Physical Review A **90**, 032114 (2014).

[106] L. C. Andreani, "Exciton-Polaritons in Bulk Semiconductors and in Confined Electron and Photon Systems", in *Strong Light-Matter Coupling* (WORLD SCIENTIFIC, Jan. 2013), pp. 37–82.

[107] N. Lundt, A. Maryński, E. Cherotchenko, A. Pant, X. Fan, S. Tongay, G. Sęk, A. V. Kavokin, S. Höfling, and C. Schneider, "Monolayered MoSe 2 : a candidate for room temperature polaritonics", 2D Materials **4**, 015006 (2016).

[108] Y. V. Morozov and M. Kuno, "Optical constants and dynamic conductivities of single layer MoS2, MoSe2, and WSe2", Applied Physics Letters **107**, 083103 (2015).

[109] B. M. Garraway, "The Dicke model in quantum optics: Dicke model revisited", Philosophical Transactions of the Royal Society A: Mathematical, Physical and Engineering Sciences **369**, 1137–1155 (2011).

[110] L. C. Andreani, G. Panzarini, and J.-M. Gérard, "Strong-coupling regime for quantum boxes in pillar microcavities: Theory", Physical Review B **60**, 13276–13279 (1999).

[111] K. Srinivasan and O. Painter, "Momentum space design of high-Q photonic crystal optical cavities", Optics Express **10**, 670–684 (2002).

[112] D. Rosser, T. Fryett, A. Saxena, A. Ryou, A. Majumdar, and A. Majumdar, "High-precision local transfer of van der Waals materials on nanophotonic structures", Optical Materials Express **10**, 645–652 (2020).

[113] J. J. Olivero and R. L. Longbothum, "Empirical fits to the Voigt line width: A brief review", Journal of Quantitative Spectroscopy and Radiative Transfer **17**, 233–236 (1977).

[114] M. Selig, G. Berghäuser, A. Raja, P. Nagler, C. Schüller, T. F. Heinz, T. Korn, A. Chernikov, E. Malic, and A. Knorr, "Excitonic linewidth and coherence lifetime in monolayer transition metal dichalcogenides", Nature Communications **7**, 13279 (2016).

[115] K. P. O'Donnell and X. Chen, "Temperature dependence of semiconductor band gaps", Applied Physics Letters **58**, 2924–2926 (1991).

[116] S. Tongay, J. Zhou, C. Ataca, K. Lo, T. S. Matthews, J. Li, J. C. Grossman, and J. Wu, "Thermally driven crossover from indirect toward direct bandgap in 2D semiconductors: MoSe2 versus MoS2", Nano Letters **12**, 5576–5580 (2012).

[117] S. Rudin, T. L. Reinecke, and B. Segall, "Temperature-dependent exciton linewidths in semiconductors", Physical Review B **42**, 11218–11231 (1990).

[118] J. Yang, H. Giessen, and P. Lalanne, "Simple Analytical Expression for the Peak-Frequency Shifts of Plasmonic Resonances for Sensing", Nano Letters **15**, 3439–3444 (2015).

[119] K. G. Cognée, W. Yan, F. L. China, D. Balestri, F. Intonti, M. Gurioli, A. F. Koenderink, and P. Lalanne, "Mapping complex mode volumes with cavity perturbation theory", Optica **6**, 269–273 (2019).

[120] A. Majumdar, A. Rundquist, M. Bajcsy, and J. Vučković, "Cavity quantum electrodynamics with a single quantum dot coupled to a photonic molecule", Physical Review B **86**, 045315 (2012).

[121] D. Englund, A. Faraon, I. Fushman, N. Stoltz, P. Petroff, and J. Vučković, "Controlling cavity reflectivity with a single quantum dot", Nature **450**, 857–861 (2007).

[122] F. P. Laussy, E. d. Valle, M. Schrapp, A. Laucht, and J. J. Finley, "Climbing the Jaynes-Cummings ladder by photon counting", Journal of Nanophotonics **6**, 061803 (2012).

[123] D. Englund, A. Majumdar, A. Faraon, M. Toishi, N. Stoltz, P. Petroff, and J. Vučković, "Resonant Excitation of a Quantum Dot Strongly Coupled to a Photonic Crystal Nanocavity", Physical Review Letters **104**, 073904 (2010).

[124] J.-T. Shen and S. Fan, "Theory of single-photon transport in a single-mode waveguide. I. Coupling to a cavity containing a two-level atom", Physical Review A **79**, 023837 (2009).

[125] J.-T. Shen and S. Fan, "Theory of single-photon transport in a single-mode waveguide. II. Coupling to a whispering-gallery resonator containing a two-level atom", Physical Review A **79**, 023838 (2009).

[126] F. O. Afzal, S. I. Halimi, and S. M. Weiss, "Efficient side-coupling to photonic crystal nanobeam cavities via state-space overlap", JOSA B **36**, 585–595 (2019).

[127] E. W. Martin, J. Horng, H. G. Ruth, E. Paik, M.-H. Wentzel, H. Deng, and S. T. Cundiff, "Encapsulation Narrows and Preserves the Excitonic Homogeneous Linewidth of Exfoliated Monolayer ${\mathrm{Mo}\mathrm{Se}}_{2}$", Physical Review Applied **14**, 021002 (2020).

[128] S. Kang, K. Kim, B. H. Kim, J. Kim, K. I. Sim, J.-U. Lee, S. Lee, K. Park, S. Yun, T. Kim, A. Nag, A. Walters, M. Garcia-Fernandez, J. Li, L. Chapon, K.-J. Zhou, Y.-W. Son, J. H. Kim, H. Cheong, and J.-G. Park, "Coherent many-body exciton in van der Waals antiferromagnet NiPS3", Nature **583**, 785–789 (2020).

[129] J. G. Roch, N. Leisgang, G. Froehlicher, P. Makk, K. Watanabe, T. Taniguchi, C. Schönenberger, and R. J. Warburton, "Quantum-Confined Stark Effect in a MoS2 Monolayer van der Waals Heterostructure", Nano Letters **18**, 1070–1074 (2018).

[130] Y. Tang, J. Gu, S. Liu, K. Watanabe, T. Taniguchi, J. Hone, K. F. Mak, and J. Shan, "Tuning layer-hybridized moiré excitons by the quantum-confined Stark effect", Nature Nanotechnology **16**, 52–57 (2021).

[131] J. Chen, X. Zhao, S. J. R. Tan, H. Xu, B. Wu, B. Liu, D. Fu, W. Fu, D. Geng, Y. Liu, W. Liu, W. Tang, L. Li, W. Zhou, T. C. Sum, and K. P. Loh, "Chemical Vapor Deposition of Large-Size Monolayer MoSe2 Crystals on Molten Glass", Journal of the American Chemical Society **139**, 1073–1076 (2017).

[132]F. Liu, W. Wu, Y. Bai, S. H. Chae, Q. Li, J. Wang, J. Hone, and X.-Y. Zhu, "Disassembling 2D van der Waals crystals into macroscopic monolayers and reassembling into artificial lattices", Science **367**, 903–906 (2020).

[133]G. Moody, C. Kavir Dass, K. Hao, C.-H. Chen, L.-J. Li, A. Singh, K. Tran, G. Clark, X. Xu, G. Berghäuser, E. Malic, A. Knorr, and X. Li, "Intrinsic homogeneous linewidth and broadening mechanisms of excitons in monolayer transition metal dichalcogenides", Nature Communications **6**, 8315 (2015).

[134]C. Robert, D. Lagarde, F. Cadiz, G. Wang, B. Lassagne, T. Amand, A. Balocchi, P. Renucci, S. Tongay, B. Urbaszek, and X. Marie, "Exciton radiative lifetime in transition metal dichalcogenide monolayers", Physical Review B **93**, 205423 (2016).

[135]F. Cadiz, E. Courtade, C. Robert, G. Wang, Y. Shen, H. Cai, T. Taniguchi, K. Watanabe, H. Carrere, D. Lagarde, M. Manca, T. Amand, P. Renucci, S. Tongay, X. Marie, and B. Ur-baszek, "Excitonic Linewidth Approaching the Homogeneous Limit in ${\mathrm{MoS}}_{2}$-Based van der Waals Heterostructures", Physical Review X **7**, 021026 (2017).

[136]O. A. Ajayi, J. V. Ardelean, G. D. Shepard, J. Wang, A. Antony, T. Taniguchi, K. Watanabe, T. F. Heinz, S. Strauf, X.-Y. Zhu, and J. C. Hone, "Approaching the intrinsic photoluminescence linewidth in transition metal dichalcogenide monolayers", 2D Materials **4**, 031011 (2017).

[137]D. Christiansen, M. Selig, G. Berghäuser, R. Schmidt, I. Niehues, R. Schneider, A. Arora, S. M. de Vasconcellos, R. Bratschitsch, E. Malic, and A. Knorr, "Phonon Sidebands in Monolayer Transition Metal Dichalcogenides", Physical Review Letters **119**, 187402 (2017).

[138]M. M. Glazov, "Phonon wind and drag of excitons in monolayer semiconductors", Physical Review B **100**, 045426 (2019).

[139]A. Majumdar, E. D. Kim, Y. Gong, M. Bajcsy, and J. Vučković, "Phonon mediated off-resonant quantum dot–cavity coupling under resonant excitation of the quantum dot", Physical Review B **84**, 085309 (2011).

[140]S. Ates, S. M. Ulrich, A. Ulhaq, S. Reitzenstein, A. Löffler, S. Höfling, A. Forchel, and P. Michler, "Non-resonant dot–cavity coupling and its potential for resonant single-quantum-dot spectroscopy", Nature Photonics **3**, 724–728 (2009).

[141]O. Salehzadeh, M. Djavid, N. H. Tran, I. Shih, and Z. Mi, "Optically Pumped Two-Dimensional MoS2 Lasers Operating at Room-Temperature", Nano Letters **15**, 5302–5306 (2015).

[142]C. Javerzac-Galy, A. Kumar, R. D. Schilling, N. Piro, S. Khorasani, M. Barbone, I. Goykhman, J. B. Khurgin, A. C. Ferrari, and T. J. Kippenberg, "Excitonic Emission of Monolayer Semiconductors Near-Field Coupled to High-Q Microresonators", Nano Letters **18**, 3138–3146 (2018).

[143]J. C. L. Carreño and F. P. Laussy, "Excitation with quantum light. I. Exciting a harmonic oscillator", Physical Review A **94**, 063825 (2016).

[144]J. C. L. Carreño, C. Sánchez Muñoz, E. del Valle, and F. P. Laussy, "Excitation with quantum light. II. Exciting a two-level system", Physical Review A **94**, 063826 (2016).

[145]T. Takagahara, "Localization and energy transfer of quasi-two-dimensional excitons in GaAs-AlAs quantum-well heterostructures", Physical Review B **31**, 6552–6573 (1985).

[146]J. Singh, *Excitation Energy Transfer Processes in Condensed Matter: Theory and Applications* (Springer Science & Business Media, Nov. 2013).

[147]S. Hughes and H. J. Carmichael, "Phonon-mediated population inversion in a semiconductor quantum-dot cavity system", New Journal of Physics **15**, 053039 (2013).

[148]A. J. Leggett, S. Chakravarty, A. T. Dorsey, M. P. A. Fisher, A. Garg, and W. Zwerger, "Dynamics of the dissipative two-state system", Reviews of Modern Physics **59**, 1–85 (1987).

[149]I. Wilson-Rae and A. Imamoğlu, "Quantum dot cavity-QED in the presence of strong electron-phonon interactions", Physical Review B **65**, 235311 (2002).

[150]P. Rabl, "Photon Blockade Effect in Optomechanical Systems", Physical Review Letters **107**, 063601 (2011).

[151] R. E. Merrifield, "Theory of the Vibrational Structure of Molecular Exciton States", The Journal of Chemical Physics **40**, 445–450 (1964).

[152] G. D. Mahan, *Many-Particle Physics*, 3rd ed., Physics of Solids and Liquids (Springer US, 2000).

[153] C. Roy and S. Hughes, "Polaron master equation theory of the quantum-dot Mollow triplet in a semiconductor cavity-QED system", Physical Review B **85**, 115309 (2012).

[154] K. Roy-Choudhury and S. Hughes, "Quantum theory of the emission spectrum from quantum dots coupled to structured photonic reservoirs and acoustic phonons", Physical Review B **92**, 205406 (2015).

[155] C. Roy and S. Hughes, "Influence of Electron–Acoustic-Phonon Scattering on Intensity Power Broadening in a Coherently Driven Quantum-Dot–Cavity System", Physical Review X **1**, 021009 (2011).

[156] D. P. S. McCutcheon and A. Nazir, "Quantum dot Rabi rotations beyond the weak exciton–phonon coupling regime", New Journal of Physics **12**, 113042 (2010).

[157] C. Roy and S. Hughes, "Phonon-Dressed Mollow Triplet in the Regime of Cavity Quantum Electrodynamics: Excitation-Induced Dephasing and Nonperturbative Cavity Feeding Effects", Physical Review Letters **106**, 247403 (2011).

[158] R. Manson, K. Roy-Choudhury, and S. Hughes, "Polaron master equation theory of pulse-driven phonon-assisted population inversion and single-photon emission from quantum-dot excitons", Physical Review B **93**, 155423 (2016).

[159] M. Wilkinson, F. Yang, E. J. Austin, and K. P. O'Donnell, "A statistical topographic model for exciton luminescence spectra", Journal of Physics: Condensed Matter **4**, 8863–8878 (1992).

[160] S. Weiler, A. Ulhaq, S. M. Ulrich, D. Richter, M. Jetter, P. Michler, C. Roy, and S. Hughes, "Phonon-assisted incoherent excitation of a quantum dot and its emission properties", Physical Review B **86**, 241304 (2012).

[161]G. S. Agarwal, "Additional vacuum-field Rabi splittings in cavity QED", Physical Review A **43**, 2595–2598 (1991).

[162]H. J. Carmichael, "Classical interpretation of "Additional vacuum-field Rabi splittings in cavity QED"", Physical Review A **44**, 4751–4752 (1991).

[163]Y. Luo, N. Liu, X. Li, J. C. Hone, and S. Strauf, "Single photon emission in WSe 2 up 160\hspace0.167emK by quantum yield control", 2D Materials **6**, 035017 (2019).

[164]K. Greben, S. Arora, M. G. Harats, and K. I. Bolotin, "Intrinsic and Extrinsic Defect-Related Excitons in TMDCs", Nano Letters **20**, 2544–2550 (2020).

[165]G. Plechinger, P. Nagler, A. Arora, R. Schmidt, A. Chernikov, A. G. del Águila, P. C. M. Christianen, R. Bratschitsch, C. Schüller, and T. Korn, "Trion fine structure and coupled spin–valley dynamics in monolayer tungsten disulfide", Nature Communications **7**, 12715 (2016).

[166]T. P. Lyons, S. Dufferwiel, M. Brooks, F. Withers, T. Taniguchi, K. Watanabe, K. S. Novoselov, G. Burkard, and A. I. Tartakovskii, "The valley Zeeman effect in inter- and intra-valley trions in monolayer WSe2", Nature Communications **10**, 2330 (2019).

[167]Z. Li, T. Wang, Z. Lu, C. Jin, Y. Chen, Y. Meng, Z. Lian, T. Taniguchi, K. Watanabe, S. Zhang, D. Smirnov, and S.-F. Shi, "Revealing the biexciton and trion-exciton complexes in BN encapsulated WSe2", Nature Communications **9**, 3719 (2018).

[168]P. Dey, J. Paul, Z. Wang, C. E. Stevens, C. Liu, A. H. Romero, J. Shan, D. J. Hilton, and D. Karaiskaj, "Optical Coherence in Atomic-Monolayer Transition-Metal Dichalcogenides Limited by Electron-Phonon Interactions", Physical Review Letters **116**, 127402 (2016).

[169]T. Calarco, A. Datta, P. Fedichev, E. Pazy, and P. Zoller, "Spin-based all-optical quantum computation with quantum dots: Understanding and suppressing decoherence", Physical Review A **68**, 012310 (2003).

[170]A. Nazir, "Photon statistics from a resonantly driven quantum dot", Physical Review B **78**, 153309 (2008).

[171] J. Xue, K.-D. Zhu, and H. Zheng, "Detuning effect in quantum dynamics of a strongly coupled single quantum dot–cavity system", Journal of Physics: Condensed Matter **20**, 325209 (2008).

[172] R. Schmidt, I. Niehues, R. Schneider, M. Drüppel, T. Deilmann, M. Rohlfing, S. M. d. Vasconcellos, A. Castellanos-Gomez, and R. Bratschitsch, "Reversible uniaxial strain tuning in atomically thin WSe 2", 2D Materials **3**, 021011 (2016).

[173] M. K. Agarwal and P. A. Wani, "Growth conditions and crystal structure parameters of layer compounds in the series Mo1-xWxSe2", Materials Research Bulletin **14**, 825–830 (1979).

[174] Z. Jin, X. Li, J. T. Mullen, and K. W. Kim, "Intrinsic transport properties of electrons and holes in monolayer transition-metal dichalcogenides", Physical Review B **90**, 045422 (2014).

[175] M. D. Luca, X. Cartoixà, J. Martín-Sánchez, M. López-Suárez, R. Trotta, R. Rurali, and I. Zardo, "New insights in the lattice dynamics of monolayers, bilayers, and trilayers of WSe2 and unambiguous determination of few-layer-flakes' thickness", 2D Materials **7**, 025004 (2020).

[176] J. R. Johansson, P. D. Nation, and F. Nori, "QuTiP: An open-source Python framework for the dynamics of open quantum systems", Computer Physics Communications **183**, 1760–1772 (2012).

[177] F. Lohof, A. Steinhoff, M. Florian, M. Lorke, D. Erben, F. Jahnke, and C. Gies, "Prospects and Limitations of Transition Metal Dichalcogenide Laser Gain Materials", Nano Letters **19**, 210–217 (2019).

[178] S. Kuhr, S. Gleyzes, C. Guerlin, J. Bernu, U. B. Hoff, S. Deléglise, S. Osnaghi, M. Brune, J.-M. Raimond, S. Haroche, E. Jacques, P. Bosland, and B. Visentin, "Ultrahigh finesse Fabry-Pérot superconducting resonator", Applied Physics Letters **90**, 164101 (2007).

[179]S. Haroche, "Nobel Lecture: Controlling photons in a box and exploring the quantum to classical boundary", Reviews of Modern Physics **85**, 1083–1102 (2013).

[180]E. Zubizarreta Casalengua, J. C. López Carreño, F. P. Laussy, and E. d. Valle, "Conventional and Unconventional Photon Statistics", Laser & Photonics Reviews **14**, 1900279 (2020).

[181]M. Bamba, A. Imamoğlu, I. Carusotto, and C. Ciuti, "Origin of strong photon antibunching in weakly nonlinear photonic molecules", Physical Review A **83**, 021802 (2011).

[182]V. Shahnazaryan, I. Iorsh, I. A. Shelykh, and O. Kyriienko, "Exciton-exciton interaction in transition-metal dichalcogenide monolayers", Physical Review B **96**, 115409 (2017).

[183]H. Flayac and V. Savona, "Input-output theory of the unconventional photon blockade", Physical Review A **88**, 033836 (2013).

[184]A. Majumdar, M. Bajcsy, A. Rundquist, and J. Vučković, "Loss-Enabled Sub-Poissonian Light Generation in a Bimodal Nanocavity", Physical Review Letters **108**, 183601 (2012).

[185]W. Zhang, Z. Yu, Y. Liu, and Y. Peng, "Optimal photon antibunching in a quantum-dot–bimodal-cavity system", Physical Review A **89**, 043832 (2014).

[186]F. Tassone and Y. Yamamoto, "Exciton-exciton scattering dynamics in a semiconductor microcavity and stimulated scattering into polaritons", Physical Review B **59**, 10830–10842 (1999).

[187]G. Rochat, C. Ciuti, V. Savona, C. Piermarocchi, A. Quattropani, and P. Schwendimann, "Excitonic Bloch equations for a two-dimensional system of interacting excitons", Physical Review B **61**, 13856–13862 (2000).

[188]M. L. Steyn-Ross and C. W. Gardiner, "Quantum theory of excitonic optical bistability", Physical Review A **27**, 310–325 (1983).

[189]E. Togan, H.-T. Lim, S. Faelt, W. Wegscheider, and A. Imamoglu, "Enhanced Interactions between Dipolar Polaritons", Physical Review Letters **121**, 227402 (2018).

[190]I. Rosenberg, D. Liran, Y. Mazuz-Harpaz, K. West, L. Pfeiffer, and R. Rapaport, "Strongly interacting dipolar-polaritons", Science Advances **4**, eaat8880.

[191]W. Li, X. Lu, S. Dubey, L. Devenica, and A. Srivastava, "Dipolar interactions between localized interlayer excitons in van der Waals heterostructures", Nature Materials **19**, 624–629 (2020).